Rheinisch-Westfälische Technische Hochschule Aachen
Fachrichtung Physik

Search for new Physics with high p_T τ-Leptons in Run 2 CMS Data

Masterarbeit
von Marcel Materok

zur Erlangung des zweiten Hochschulgrades

Master of Science (M.Sc.)

vorgelegt der
Fakultät für Mathematik, Informatik und
Naturwissenschaften der RWTH Aachen

erstellt im
September 2017

angefertigt am
III. Physikalischen Institut A

bei
Prof. Dr. Thomas Hebbeker

Zweitgutachter
PD Dr. Oliver Pooth

Abstract

The search for new physics has been performed in data taken with the CMS experiment corresponding to an integrated luminosity of $\mathcal{L}_{\text{int}} = 35.9\,\text{fb}^{-1}$ taken in 2016. This search heavily utilized a tau and E_T^{miss} final state, where the tau decays hadronically. The focus was on a new, heavy gauge boson W', in the context of the Sequential Standard Model (SSM) and non-universal gauge interaction model (NUGIM). While no significant deviation from the Standard Model has been observed, exclusion limits on these models have been set. The mass limits are 4200 GeV for the SSM and 2300 GeV for the NUGIM at $\cot\theta_E$=6.6, at which point the width of the W' equals 50% $M_{W'}$. For the SSM a combination of the leptonic and hadronic decay channels of the tau improved the mass limit to 4300 GeV. In the context of the SSM additionally coupling strength ratios $\frac{g_{W'}}{g_W}$ have been excluded starting at the value 0.2 for low masses increasing to 1.5 for high masses. Additionally a model-independent cross section limit has been derived, which ranges from $174\,\text{fb}^{-1}$ at the lower M_T thresholds $\text{M}_T^{\text{min}} = 300\,\text{GeV}$ to $0.58\,\text{fb}^{-1}$ at $\text{M}_T^{\text{min}} = 2000\,\text{GeV}$.

Kurzdarstellung

Die Suche nach neuer Physik wurde in Daten durchgeführt, die 2016 mit dem CMS Experiment genommen wurden und einer integrierten Luminosität von $\mathcal{L}_{\text{int}} = 35.9\,\text{fb}^{-1}$ entspricht. Diese Suche nutzt verstärkt einen Tauon und E_T^{miss} Endzustand, in dem das Tauon hadronisch zerfällt. Im Fokus standen dabei das Sequentielle Standard Modell (SSM) und das nicht universelle Eichwechselwirkungs Modell (NUGIM). Während keine signifikanten Abweichungen vom Standard Modell beobachtet wurden, wurden Ausschlussgrenzen auf diese Modelle gesetzt. Die Massenausschlussgrenzen betragen 4200 GeV für das SSM und 2300 GeV für das NUGIM bei dem Wert $\cot\theta_E$=6.6, bei dem die Breite des W' 50% $M_{W'}$ gleicht. Die Kombination der leptonischen und hadronischen Zerfallskanäle des Tauons verbessert die Massenausschlussgrenze des SSM auf 4300 GeV. Im Rahmen des SSM konnte zusätzlich das Verhältnis der Kopplungsstärken $\frac{g_{W'}}{g_W}$ ab 0.2 bei niedrigen Massen und ab 1.5 bei hohen Massen ausgeschlossen werden. Zusätzlich wurde eine modellunabhängige Ausschlussgrenze für den Wechselwirkungsquerschnitt gesetzt, die von $174\,\text{fb}^{-1}$ für die unteren M_T Grenzen von $\text{M}_T^{\text{min}} = 300\,\text{GeV}$ bis $0.58\,\text{fb}^{-1}$ bei $\text{M}_T^{\text{min}} = 2000\,\text{GeV}$ reichen.

Table of Contents

Chapter 1

Introduction

Most physicists hope that the whole universe can be described by laws and can be broken down to the most fundamental building blocks everything is made of. Particle physicists have been quite successful at this task developing one of the most precise theories to date: the Standard Model of Particle Physics. That being said, particle physics is still developing. One can see this development in the recent discovery of the Higgs boson. This reveals, however, also the need for further developments, as some of the Higgs' properties still have to be measured. This development can also be seen in the lack of a description for the particle nature of Dark Matter, which has been proposed in astrophysics.

This thesis can be seen as a part of the precise testing and might be part of the development of the Standard Model. An analysis of the tau lepton and missing transverse energy final state is performed. One part of the analysis will be the search for deviations from the Standard Model in the high mass region of the transverse mass variable. This is performed in the context of Beyond the Standard Model physics in the so-called „Sequential Standard Model".

This thesis is sectioned into eight parts. After the introduction, the experimental setup and theoretical framework are explained, the object reconstruction as well as the datasets and analysis framework are introduced. Once the analysis has described, the results are interpreted in terms of exclusion limits. The thesis concludes with a summary and an outlook.

Chapter 2

Experimental Setup

In this chapter the experimental setup will be described. As this thesis is based on data taken with the Compact Muon Solenoid (CMS) detector [1] originating from proton-proton collisions from the Large Hadron Collider (LHC), both CMS and LHC will be explained. Most of the information is taken from the respective papers published in the journal of instrumentation and is referenced in the different sections.

2.1 Large Hadron Collider

The Large Hadron Collider [2] is a collider operated by the Conseil Européen pour la Recherche Nucléaire, or CERN for short. It is also the accelerator in a chain of accelerators at CERN. The chain of accelerators can be seen in Fig. 2.1. It uses a ring geometry with a circumference of approximately 27 km and can be operated with heavy ions or protons. Only the latter will be relevant for this thesis. In order to keep these protons on a circular path, they are constantly bent by superconducting dipole magnets and travel close to the speed of light in two beams with opposite directions. Approximately 1.15×10^{11} protons travel in so-called bunches. At a given time up to 2808 of these bunches traverse the LHC in each beam with a bunch spacing of 25 ns. At four distinct points the two beams are cross each other resulting in proton-proton collisions. Around each of these points a detector is placed recording the collision. The four experiments are divided into two groups, the general purpose detectors ATLAS [3] and CMS, and specialized detectors ALICE [4] and LHCb [5].

Collisions for research purposes were first recorded between 2010 and 2013 with a center of mass energy of $\sqrt{s}$ =7 TeV and $\sqrt{s}$ =8 TeV. In 2015 the second data taking period for research purposes has been started at a center of mass energy of $\sqrt{s}$ =13 TeV. Data from the second research data taking will be used in this thesis with the focus being on data collected in 2016. In both of the data taking periods, commonly referred to as "Runs", there is one characteristic parameter, called luminosity. Where the instantaneous luminosity L is a measure for the collision rate delivered by the collider, the integrated luminosity $\mathcal{L}_{\text{int}}$ enables a possibility to predict the number of events recorded in a given time window for a distinct process. The instantaneous luminosity and the integrated luminosity are connected by the integral over the time, namely $\mathcal{L}_{\text{int}} = \int L \mathrm{d}t$. The instantaneous luminosity can be calculated by [7]

$$L = \frac{N_b f}{4\pi} \frac{N_1 N_2}{\sigma_x \sigma_y}$$

with N_b being the number of bunches, f the revolution frequency, $N_{1/2}$ the number of protons in the first or second beam and $\sigma_{x/y}$ the transversal bunch size. This formula only holds for

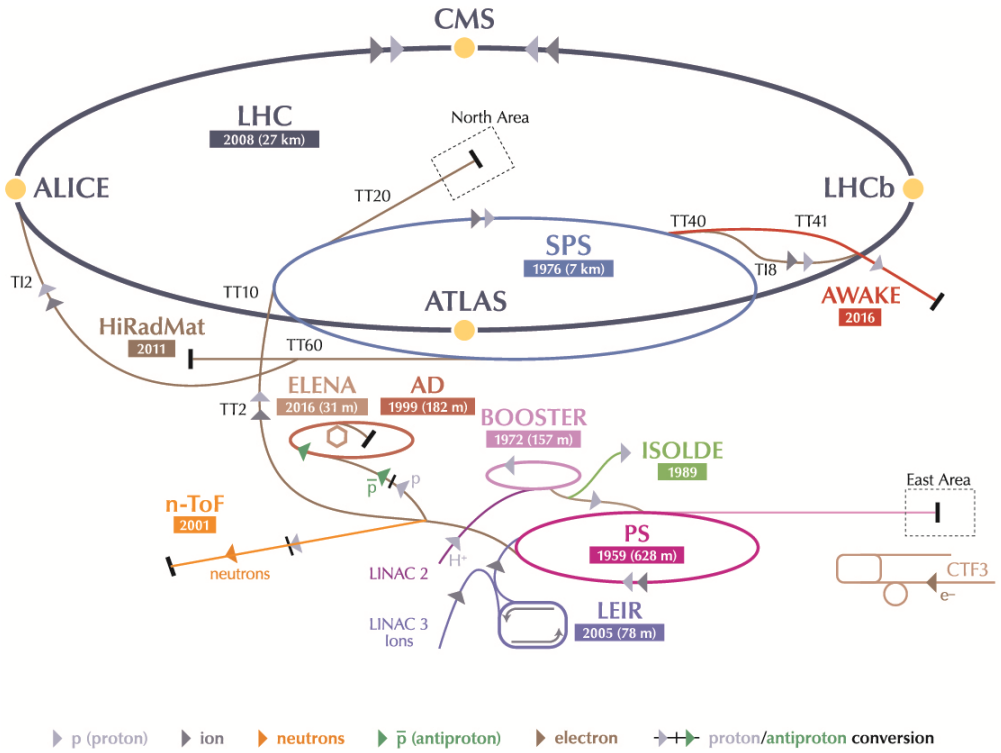

Figure 2.1: The accelerator chain starting with the LINAC and ending with the LHC is shown. The picture is taken from [6].

Gaussian-shaped, equal beams in a head-on collision. If the bunches of each beam do not have the same size or the beams collide at a given angle, this formula has to be corrected. In the 2016 data taking the design value for the integrated luminosity of $10^{34}\text{cm}^{-2}\text{s}^{-}1$ was exceeded and values of up to $1.5{\cdot}10^{34}\text{cm}^{-2}\text{s}^{-}1$ were achieved [8].

2.2 Compact Muon Solenoid Detector

The Compact Muon Solenoid is a multi-purpose detector in a cavern approximately 100m underneath the French city Cessy. It is built cylindrically around an interaction point of the two beams, called IP 5. With a length of 28.7m and a diameter of 15m it is impressively compact compared to ATLAS which is almost twice as big. The compact design allows most of the active material to be located within the solenoid. CMS consists of several concentric detector layers, the magnet and the muon system going inside out. In CMS all subdetectors are divided in a barrel and two endcap regions. The structure of CMS can be seen in Fig. 2.2, with the tracking system being located innermost, next being the calorimeters and beyond the solenoid magnet the muon system can be found.

To describe positions and directions in CMS a suitable coordinate system is used. It is derived from a right handed Cartesian system where the origin is in the center of CMS. The x-axis points to the center of the LHC, the y-axis points upwards and the z-axis points west, parallel to the beam pipe. The set of variables comprising the commonly used coordinate system in CMS features the azimuthal angle ϕ in the $x-y$ plane and the pseudorapidity η. The latter is defined by

$$\eta = -\ln\tan\left(\frac{\theta}{2}\right)$$

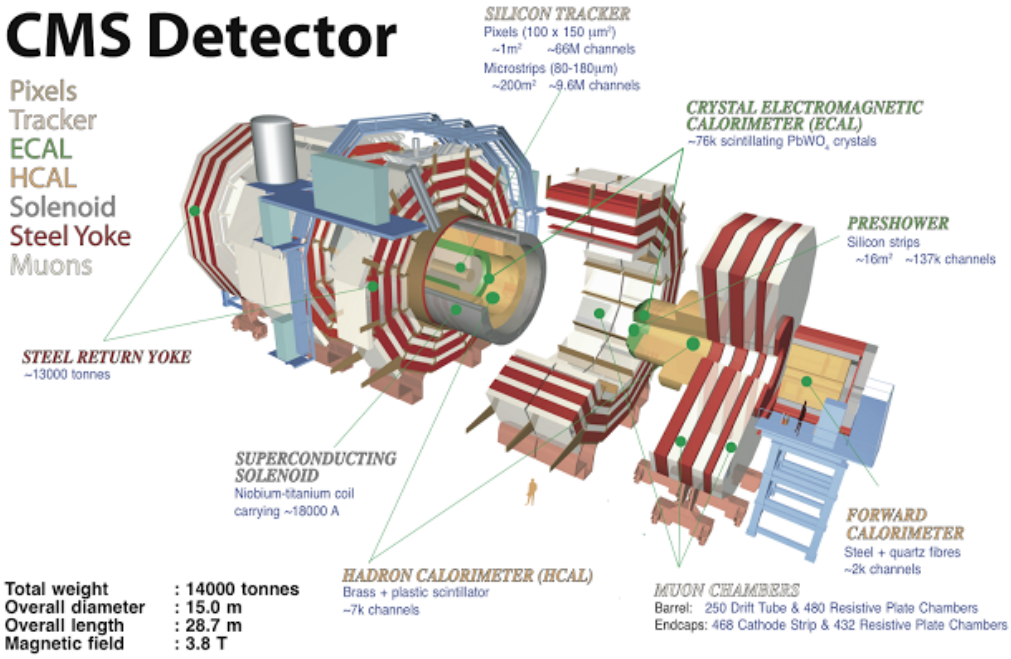

Figure 2.2: The picture taken from [?] shows the CMS detector with its different layers. From the outside to the inside the muon system, the solenoid magnet, calorimeters and the tracking system are located.

where θ is the polar angle. Following the invariance under Lorentz transformations, the pseudorapidity allows for a boost independent description of the angular distance $\Delta\eta$. Due to the unknown boosts in the rest frame of parton-parton collision, this choice is especially advantageous when working with a hadron collider such as the LHC. The spatial distance of two objects, or more generally points, in the system can be evaluated using the variable ΔR which can be defined as

$$\Delta R = \sqrt{\Delta\phi^2 + \Delta\eta^2}$$

where $\Delta\phi$ and $\Delta\eta$ are the respective differences in the azimuthal angle ϕ and η of the two objects or points. In order to describe a specific interaction further, transverse quantities such as E_T or p_T are used. In parton-parton collisions the transverse component of the momentum is conserved and should be equal to 0 GeV. While the longitudinal component of the momentum in a given interaction is also conserved, it is not necessarily known. As the transverse component of the momentum is conserved and its vectorial sum should be 0 GeV, the transverse mass is used as the discriminating variable. The transverse mass is defined as $M_T = \sqrt{2p_\mathrm{T}E_\mathrm{T}^\mathrm{miss}(1-\cos\Delta\phi)}$.

2.2.1 Tracker

The innermost component of CMS is the tracking system [9–11] which comprises pixel and strip detectors. Their task is to detect charged particles with a high spatial resolution. This resolution allows for the reconstruction of the trajectory of the particles and thus for a precise measurement of the curvature. The curvature is used to determine the momentum of a given particle. Using the information of different tracks, vertices can be reconstructed. In order to

achieve this, the tracking system needs to be as close as possible to the interaction point. The minimal distance of the pixel detectors to the beam spot is 4.4 cm. As a consequence of the small distance to the beam spot, the detectors have to endure high radiation levels. To limit the radiation levels only the region up to $|\eta| < 2.5$ is covered. A need for a fast response arises following the 25 n sec bunch spacing and the correspondingly high instantaneous luminosities provided by the LHC. Due to these reasons detectors on silicon basis are chosen.

With the a radial distance ranging from 4.4 cm to 10.2 cm the pixel detectors cover an area of 1 m^2. Each of the roughly 66 million pixel cells is sized either 25 µm × 100 µm or 50 µm × 50 µm and has a spatial resolution of 15 µm. Around 9.3 million strip detectors extend the range of the tracking system up to 1.2 m and cover a region of 198 m^2. Depending on where the strip is located, the dimensions of the strips are either 10 cm × 10 cm or 5 cm × 10 cm and resolutions between 23 and 53 µm can be achieved. These precise measurements can be utilized to reconstruct transverse momenta. The precision of this measurement depends on its magnitude. For example at 1 TeV in transverse momentum the resolution is at the 5% level, while for low momenta around 1 GeV the resolution is around 0.7%.

2.2.2 Calorimeters

The energies of most particles is measured inside the solenoid in one of the two calorimeters. If the particle is a charged hadron, most of the energy is typically deposited in the hadronic calorimeter (HCAL) whereas charged leptons - in case of taus, only leptonically decaying ones - deposit most of their energy in the electromagnetic calorimeters (ECAL). The arrangement inside CMS can be seen in Fig. 2.3.

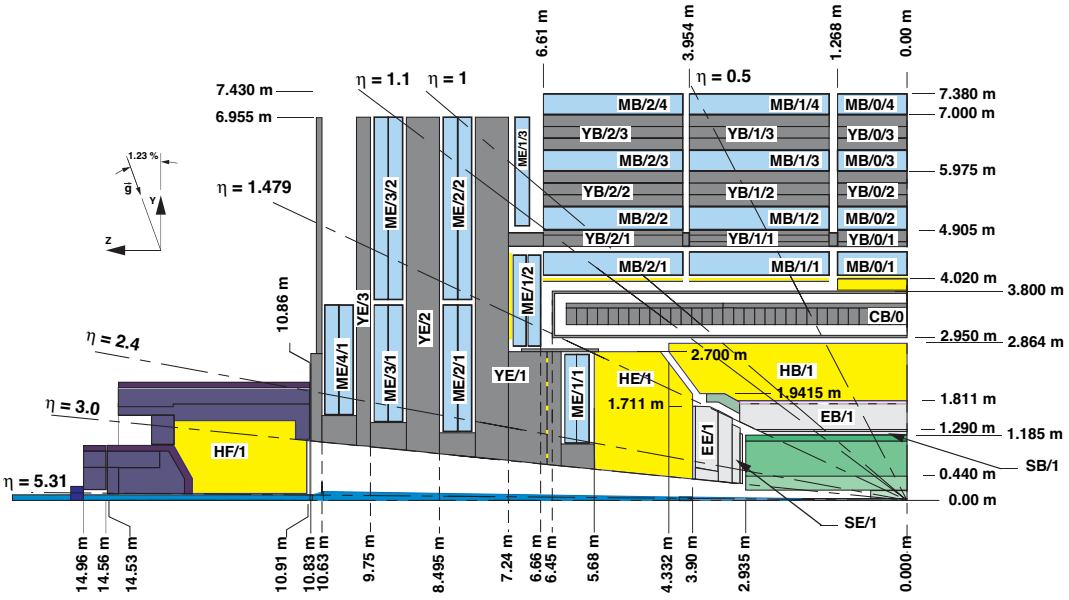

Figure 2.3: Cross-section through one quarter of the CMS detector in the $y - z$ plane, showing the different subdetectors and their ranges in pseudorapidity η. The picture is taken from [12].

Electromagnetic Calorimeter

Roughly 68000 lead tungstate ($PbWO_4$) crystals make up the ECAL [13]. While roughly 61000 of these crystals are located in the barrel, around 7000 crystals are located in the

endcaps. Since there are two regions, there has to be a transition region. This region is within $1.4442 < |\eta| < 1.566$ and is often neglected in searches relying on the ECAL resolution. The overall ECAL has a volume of more than $11\,\mathrm{m}^3$ and weighs more than 80 tons. Using all these crystals to measure the energy the resolution has been determined to be

$$\left(\frac{\sigma}{E}\right)^2 = \left(\frac{2.8\%}{\sqrt{E/GeV}}\right)^2 + \left(\frac{12\%}{E/GeV}\right)^2 + (0.3\%)^2$$

The term including the $\sqrt{E}^{-1}$ arises from stochastic effects from the electromagnetic shower, the expression including E^{-1} originates from the readout noise and the 0.3% term is due to a systematic uncertainty arising from the calibration. For sufficiently high energies the ECAL resolution is dominated by the systematic uncertainty, while for low energy the stochastic and noise effects are dominant.

Hadronic Calorimeter

Having stopped and measured most of the electrons and photons in the ECAL, the HCAL [14] is designed to measure the energy of hadrons. Most hadrons deposit energy but are not stopped in the ECAL since the nuclear interaction length is much greater at a given density than the electromagnetic one. To measure the energy of hadrons, four different subsystems have been built: the so-called hadron barrel (HB), endcap (HE), outer (HO) and forward (HF) calorimeters. The HCAL is designed as a sampling calorimeter. In the barrel and endcap regions, the calorimeter is built from brass and plastic scintillators, respectively, while the magnet acts as an absorber for the HO and uses two layers of scintillators in the first wheel, the so-called wheel 0, and one layer in the other wheels. The HF is in the harshest environment and measures the energy using Cherenkov radiation of the particles with quartz fibers embedded into a steel absorber. The HCAL overall covers a region of $|\eta| < 5$, where the barrel and endcap regions cover the region up to $|\eta| < 3$.

The stand alone energy resolution of the HCAL for $\pi^{\pm}$ is worse than the ECAL [1]

$$\left(\frac{\sigma}{E}\right)^2 = \left(\frac{138\%}{\sqrt{E/GeV}}\right)^2 + (13\%)^2\,.$$

When combining information from both calorimeters, the resolution improves to

$$\left(\frac{\sigma}{E}\right)^2 = \left(\frac{80\%}{\sqrt{E/GeV}}\right)^2 + (8\%)^2\,.$$

2.2.3 Magnet

The solenoid magnet is the core component of the detector and was one of the first parts to be decided on in the CMS collaboration [15]. The other systems are determined as a consequence of the choice of the magnet. The magnet is used to bend the trajectory of charged particles inside the detector. One can measure the radius and deduce the momentum for a given magnetic field strength using the formula

$$p[GeV] = 0.3 \cdot B[T] \cdot R[m] \sin\delta$$

where p is the momentum, B the magnetic field strength, R is the bending radius and δ is the angle between the momentum and the magnetic field. To measure high momenta, a

large magnetic field has to be produced. For this reason a superconducting magnet has been built that can produce a magnetic field strength of up to 4 T, but to maximize longevity is operated at 3.8 T. Since the magnet is a solenoid, the magnetic field is parallel to the beam axis and the trajectories are bent perpendicular to this axis. Following this, not the total momentum but the transversal component is measured. In order to close the magnetic field lines, an iron return yoke is installed in between the muon chambers.

2.2.4 Muon System

The outermost detector of CMS is the muon system [16], which is embedded in the return yoke. Like the other parts, the muon system is also divided into a barrel and endcap regions. The barrel region covers $|\eta| < 1.2$ with drift tubes (DT), and the cathode strip chambers (CSC) are used in the endcap region to cover the region of $0.9 < |\eta| < 2.4$. Both, the DT and CSC systems are composed of four layers, or so-called stations, see Fig. 2.3. Depending on the number of hits, both systems provide a comparable spatial resolution, which is better than 100 µm. The relative residual width of q/p_T of a muon in the muon system is significantly below 10% at the TeV-scale and even lower than 1% for very low p_T muons, as seen in Fig. 2.4.

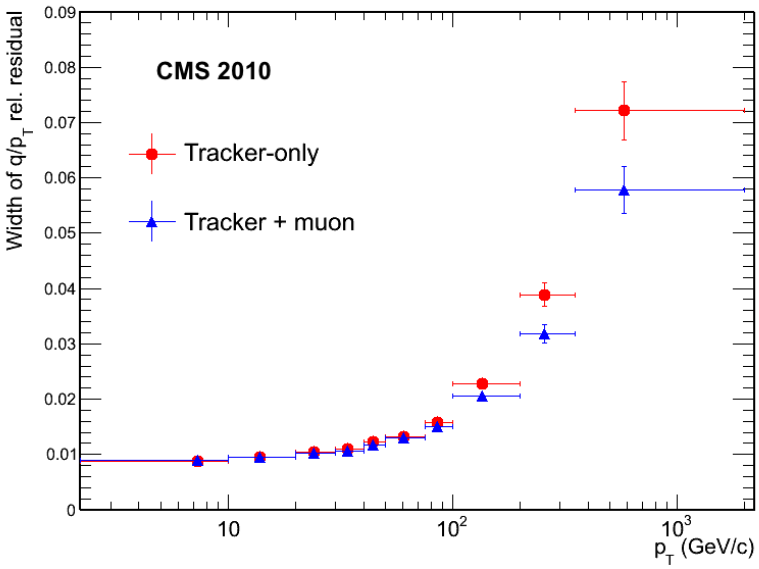

Figure 2.4: The muon resolution with both the tracker and muon system from cosmic muons is displayed. The plot is taken from [17].

2.2.5 Trigger

In the 2016 data taking a bunch spacing of 25 ns has been deployed, resulting in an event rate of 40 MHz. If every proton-proton collision event was reconstructed with this event rate, the amount of data needed to be written would be too large. Therefore one has to reduce the event rate that is kept. This is done with the trigger system in two steps. The so-called Level 1 (L1) [18] and High-Level (HLT) [19] triggers. The L1 system is implemented directly in the hardware and filters for detector responses, as shown in Fig. 2.5, while the HLT is software driven and reconstructs the event partially. The rate is reduced to approximately

100 kHz by the L1 and to roughly 1 kHz by the HLT. This two level trigger system enables the collaboration to implement new triggers without the need to change neither hardware nor the firmware for said hardware. Following the nearly complete reconstruction of the event in the HLT, triggers may consider more than one object in the final state.

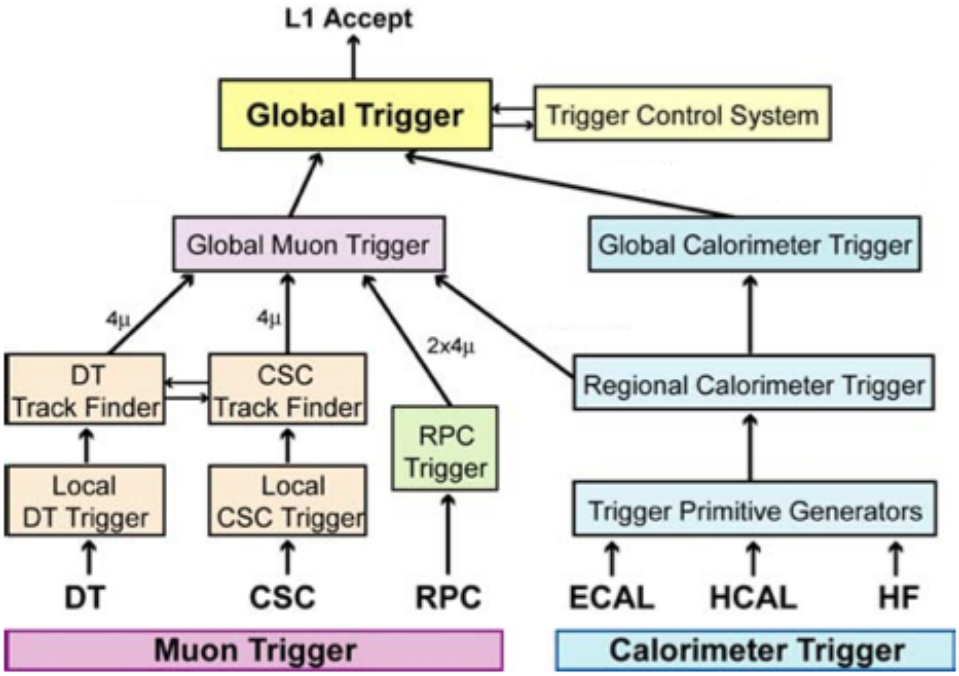

Figure 2.5: The different inputs for the Level 1 trigger are shown. The picture is taken from [1]. Most relevant for this analysis are the calorimeter triggers.

Chapter 3

Theoretical Framework

In this thesis new physics is search for using high-p_T tau leptons. To understand new physics an overview of the Standard Model of Particle Physics and the physics Beyond the Standard Model is given in this chapter. This analysis heavily focuses on the hadronic decay of the tau lepton, but the leptonic decay will be investigated as well. Therefore, the properties of the tau lepton will be discussed in this chapter in more detail.

The analysis for the leptonic decay is performed by the authors of Ref. [20], the analysis for the hadronic decay and the statistical interpretation is done by the author of this thesis.

3.1 Standard Model of Particle Physics

If not indicated otherwise, this section is based on [21] and [22]. This section is meant to be a short overview of the theory used and is, however, not meant to explain every detail of it and requires prior knowledge to be understood properly.

3.1.1 Gauge Theories

In physics there are two approaches to utilize gauge fields. One can derive these fields from physics equations, obtained from empirical measurements, and extract further knowledge about the inherent symmetries. One can also impose symmetries, inherent to the investigated problem, and derive both the gauge fields and the physics governing these fields. If the latter is chosen, these theories often are called gauge theories. This approach was used to obtain the Standard Model of Particle Physics (SM). The SM is a locally invariant gauge theory that uses a formalism analogous to the Lagrange formalism of classical mechanics. Where the motion of a particle is described by the Lagrange function in mechanics, in particle physics the relativistic, spin-dependent and quantized solutions to the Lagrange density, in the following called Lagrangian, describe gauge fields. To obtain the equation of motion for a given particle the Euler-Lagrange equation

$$\partial_\mu \left(\frac{\partial \mathcal{L}}{\partial(\partial_\mu \Psi)} \right) = \frac{\partial \mathcal{L}}{\partial \Psi}$$

has to be solved for a given field Ψ. If one imposes a given symmetry, the Lagrangian has to be invariant under the associated gauge transformation. Considering a shift in spacetime should not change the physics of a system, If one therefore substitutes

$$\psi \rightarrow e^{i\theta(x)}\psi,$$

the resulting Lagrangian has to remain in the same form. In order to have an invariant Lagrangian the term arising from a derivation of $\theta(x)$ has to be absorbed into the Lagrangian and can be identified as the gauge bosons which are responsible for the interactions.

3.1.2 Quantum Electrodynamics

After Dirac developed the first quantum theory describing the quantization of an electromagnetic ensemble of harmonic oscillators, the combined work of Tomonaga, Schwinger, Dyson and Feynman [23] allowed for the first fully covariant formulation of Quantum Electrodynamics that was finite in any order of perturbation theory. This theory, often abbreviated QED, describes photons as an excitation of a vector field by a U(1) group and their interactions with a spin-$\frac{1}{2}$ field. The physics governing this vector field is given by the Lagrangian

$$\mathcal{L}_{\text{QED}} = \sum_n \bar{\psi}_n(i\gamma^\mu\partial_\mu - m_n)\psi_n - \sum_n qA^\mu\bar{\psi}_n\gamma^\mu\psi_n - \frac{1}{4}F_{\mu\nu}F^{\mu\nu}$$

with ψ being the bispinor field of a spin-$\frac{1}{2}$ particle, γ^μ the Dirac matrices, m the mass of the particle, A^μ the covariant four-potential of the electromagnetic field and $F_{\mu\nu}$ the electric field tensor. The terms including A^μ, but not any derivative of A^μ, have to be added to the Lagrangian in order to guarantee invariance under a unitary transformation of ψ, e.g.

$$\psi \to U\psi, \quad \text{with} \quad U^\dagger U = 1.$$

The second term of the QED Lagrangian describes the interaction between the photon and the spin-$\frac{1}{2}$ particles. Using the Euler-Lagrange equation, the equations of motion for the fields A^μ and ψ can be derived to be

$$\Box A^\mu = e\bar{\psi}\gamma^\mu\psi(i\gamma^\mu\partial_\mu - m)\psi = e\gamma_\mu A^\mu\psi$$

This equation can be identified as the classical Maxwell equations in the Lorentz gauge and the Dirac equation including the interaction with the electromagnetic field.

3.1.3 Quantum Flavordynamics

While the U(1) symmetry group describes QED, a SU(2) describes Quantum Flavordynamics, or QFD for short. QFD is commonly referred to as the weak interaction. Requiring the SU(2) to be invariant under a local gauge symmetry, one finds in principle four gauge bosons, as opposed to the one boson of QED. Two of these four bosons are electrically charged (W^1_μ,W^2_μ) while the other two are electrically neutral (W^3_μ,B_μ). These four bosons lead to the so-called charged and neutral currents, depending on which of the type of bosons is exchanged.

The charged current has two distinct characteristics: It changes the so-called "flavor" of the interacting particles and it violates the parity maximally by only coupling to left-handed particles. Following this fact the underlying symmetry is often written as $\text{SU}(2)_L$, where the L indicates the left-handed nature of the coupling. The charge corresponding to the coupling is the so-called *weak isospin* I.

Opposed to the charged current, the neutral current also couples to right-handed particles and the charge of this coupling is called *weak hyperchage* Y. However, this second neutral current cannot be distinguished from the neutral current in QED. As a consequence the

electro-magnetic current has to be included and the electro-magnetic charge Q can be written as

$$Q = I_3 + \frac{1}{2}Y$$

where I_3 is the third component of the weak isospin.

Electro-Weak Interaction

This approach results in a unified electro-weak interaction and leads to a unification of the symmetry groups, thus a $\mathrm{SU}(2)_L \times \mathrm{U}(1)_Y$ is formed. Following the electro-weak symmetry breaking introduced by the Higgs mechanism, described in Section 3.1.5, the four bosons form mass eigenstates that are observed in nature. These are namely the bosons $W^{\pm}$, Z^0 and the photon γ which is massless. These bosons arise from the corresponding fields $W_\mu^{\pm}$, Z_μ and A_μ and are given by

$$\begin{aligned} W_\mu^{\pm} &= \sqrt{\frac{1}{2}}(W_\mu^1 \mp W_\mu^2) \\ Z_\mu &= -B_\mu \sin\theta_W + W_\mu \cos\theta_W \\ A_\mu &= B_\mu \cos\theta_W + W_\mu \sin\theta_W \end{aligned}$$

where θ_W is the mixing angle or Weinberg angle. This angle cannot be calculated but can be measured by the fraction of the masses of the physical W and Z bosons, $\frac{M_W}{M_Z} = \cos\theta_W$.

3.1.4 Quantum Chromodynamics

Beside a U(1) or a SU(2), one also could use a SU(3) group as basis for a quantum field theory. If this is done, the result is Quantum Chromodynamics, often abbreviated QCD. The underlying symmetry group introduces eight new gauge fields each resulting in an excitation called gluon with a unique combination of color charges. Furthermore, in QCD the Dirac spinor is a vector with three components, one corresponding to each of the three different color charges. Each of the three components of the vector is a bispinor field as discussed in QED. The new Dirac spinor Ψ can thus be written as

$$\Psi = \begin{pmatrix} \psi_r \\ \psi_b \\ \psi_g \end{pmatrix}$$

where the indices r, b and g indicate the color charges, commonly called red, blue and green.

In QCD only particles and states without color charge have been observed so far. For elementary particles this often requires bound states to be formed. This is in contrast to QED where all particles have been observed to be free in nature. Additionally, the bosons of QCD are able to couple to themselves, unlike their counterparts in QFD.

3.1.5 Higgs Mechanism

The observation of massive gauge bosons, namely $W^{\pm}$ and Z^0, cannot be described exclusively by a $\mathrm{SU}(2)_L \times \mathrm{U}(1)_Y$ symmetry group. A theoretical explanation was offered by three different groups independently in 1964 [24–26], with Peter Higgs and François Englert being

awarded the Nobel prize for their work in 2013. These groups explain that adding the Lagrangian of a scalar particle can explain the origin of the masses of particles that couple to the scalar particle. The Lagrangian of the scalar particle can be written as

$$\mathcal{L}_{\text{scalar}} = \frac{1}{2}(\partial_m u\Phi)^*(\partial^m u\Phi) + \frac{1}{2}\mu^2(\Phi^*\Phi) - \frac{1}{4}\lambda(\Phi^*\Phi)^2$$

where Φ is a new complex field and can be written in the form $\Phi = \Phi_1 + i\Phi_2$. From this Lagrangian one can read off the around 0 symmetrical potential $\mathcal{V} = -\frac{1}{2}\mu^2(\Phi^*\Phi) + \frac{1}{4}\lambda(\Phi^*\Phi)^2$. Assuming $\mu^2 > 0$, this potential is not in its ground state at $\Phi = 0$, resulting in a symmetric equation of motion but an asymmetric ground state. This leads to the often called spontaneous symmetry breaking. Sometimes this is called the electro-weak symmetry breaking. The additional Lagrangian can therefore explain the mass of the $W^{\pm}$ and Z^0 bosons and the fermions due to their coupling to the scalar particle. Another effect of this Lagrangian is the prediction of a new scalar particle, the so-called Higgs boson. In 2012 a new heavy boson was discovered and is assumed to be the Higgs boson [27–29].

3.1.6 Particles of the Standard Model

There are three fundamental interactions, the electro-magnetic, the weak and the strong interaction describd in the SM. They are mediated by the photon, the $W^{\pm}$ and Z^0 bosons and the gluons, and have been derived by their respective symmetry groups.

However, aside from these bosons, the SM contains fermions, which can be further grouped into leptons and quarks. Both quarks and leptons are sorted in three so-called „generations“ or „ families“. While each generation of the quarks consists of two differently charged elementary particles, the leptons consist of a charged and an uncharged elementary particle. Each lepton family has an associated quantum number which is conserved. While leptons have no color charge, quarks can have one of the three different color charges and thus can only be observed in bound states with no „effective“ color charge.

All of these particles can be found in Fig. 3.1.

Due to the focus on the tau lepton in this thesis, the most important properties will be introduced in the next part of this section.

Properties of the Tau Lepton

In contrast to the electron, which cannot decay due its small mass, and the muon, which can only decay into electrons, the tau lepton can also decay, both, leptonically and hadronically. This is a direct consequence of the large mass of the tau lepton of 1776 MeV, which is larger than most of the light quark mesons. The hadronic tau decay [31] – often shortened to hadronic tau – accounts for roughly 65% of the branching fraction, while only roughly 35% of the branching fraction is taken by the leptonic tau decays. The focus in this analysis is on the hadronic tau decays, however the leptonic tau decays will also be investigated. The most important decays of the tau lepton are listed in Tab. 3.2.

The multitude of decay channels available to the tau results in a significantly reduced lifetime compared to the light leptons. While the muons regularly reach the muon station and the electrons reach the electromagnetic calorimeter before losing their energy, the taus regularly decay before even reaching the innermost pixel layer. This can be estimated using a tau lepton with a transverse momentum of 900 GeV. Using the mean life time of $c\tau_{\text{tau}} = 87.03\,\mu\text{m}$, the contracted length $l_{\text{lab}} = \frac{l_0}{\gamma}$ can be calculated to be approximately 4.4 cm which is the average distance of the pixel detector in CMS to the expected interaction point.

Table 3.1: Particle content of the Standard Model of Particle Physics, values taken from [30].

Name	Mass [eV]	Charge [e]
Quarks		
Up	2.3 M	$\frac{2}{3}$
Down	4.8 M	$-\frac{1}{3}$
Charm	1.275 G	$\frac{2}{3}$
Strange	95 M	$-\frac{1}{3}$
Top	173.21 G	$\frac{2}{3}$
Bottom	4.38 G	$-\frac{1}{3}$
Leptons		
Electron	511 k	-1
Electron neutrino	<2	0
Muon	105.66 M	-1
Muon neutrino	<18.2 M	0
Tau	1.776 G	-1
Tau neutrino	<0.19 M	0
Bosons		
Photon	$< 10^{-18}$	0
Gluon	0	0
W	80.385 G	± 1
Z	91.187 G	0
Higgs	125.7 G	0

Table 3.2: The branching fractions of the decays of the tau leptons are presented [30]. In order to keep universality the combination of particle and antiparticle, as well as the charge from the hadron is expected to be inferred from the reader.

Final state	Branching fraction	Resonance	Mass of resonance [MeV]
$e\nu_e\nu_\tau$	17.83 ± 0.04	–	–
$\mu\nu_\mu\nu_\tau$	17.41 ± 0.04	–	–
$\pi\nu_\tau$	10.83 ± 0.06	–	–
$\pi\pi^0\nu_\tau$	25.52 ± 0.09	ρ	770
$\pi 2\pi^0\nu_\tau$	9.80 ± 0.011	a_1	1220
$\pi 3\pi^0\nu_\tau$	1.05 ± 0.07	–	–
$3\pi\nu_\tau$	8.99 ± 0.06	a_1	1220
$3\pi\pi^0\nu_\tau$	2.70 ± 0.08	a_1	1220
$h\omega\nu_\tau$	2.0 ± 0.08	–	–
other decays < 1%	4.36 ± 0.01	–	–

3.2 Parton Distribution Functions

In contrast to the Large Electron-Positron Collider [32], in which electrons and positrons collide, protons collide at the LHC. Due to the fact, that the proton is a bound state of two up quarks and one down quark as valence quarks, the momentum of any quark is not known precisely. The energy of a given parton, which can be either a quark or a gluon, can be statistically described by the so-called parton distribution function (PDF). The fraction of the proton momentum x carried by the parton depends on the energy transfer $\mathcal{Q}^2$ of the interaction. The probability for a given pair of x and $\mathcal{Q}$ is given by a function $f(x, \mathcal{Q})^2$. The PDF has to be taken into account in order to calculate the cross section of any interaction P in the following form:

$$\sigma(pp \to X_P) \propto \sum_i \sum_j C_{ij}^P(x_1, x_2, \alpha_S(\mathcal{Q}^2)) \otimes f(x_i, \mathcal{Q}^2) \otimes f(x_j, \mathcal{Q}^2),$$

where $C_{ij}^P(x_1, x_2, \alpha_S(\mathcal{Q}^2))$ describes the hard process for the parton types i and j at an energy $\mathcal{Q}$ with the couping constant $\alpha_S(\mathcal{Q}^2)$. The $\mathcal{Q}^2$ dependence of the PDF can be calculated using the DGLAP equations [33–35] and has been measured mostly in electron proton colliders such as HERA [36, 37]. Theory describes the PDFs up to next-to-next-to leading-order (NNLO) in QCD with the photon contributions being taken into account. There are multiple descriptions for the PDF where the differences between the various PDF sets are larger than the uncertainties on the individual PDF sets. This will be used to determine the systematic uncertainty on the PDF at a later stage in the analysis. In Fig. 3.1 an examplary PDF is shown at NNLO and in Fig. 3.2 the differences between various PDF sets are shown for the up and down quarks respectively at $\mathcal{Q}^2$=$10^4\,\mathrm{GeV}^2$.

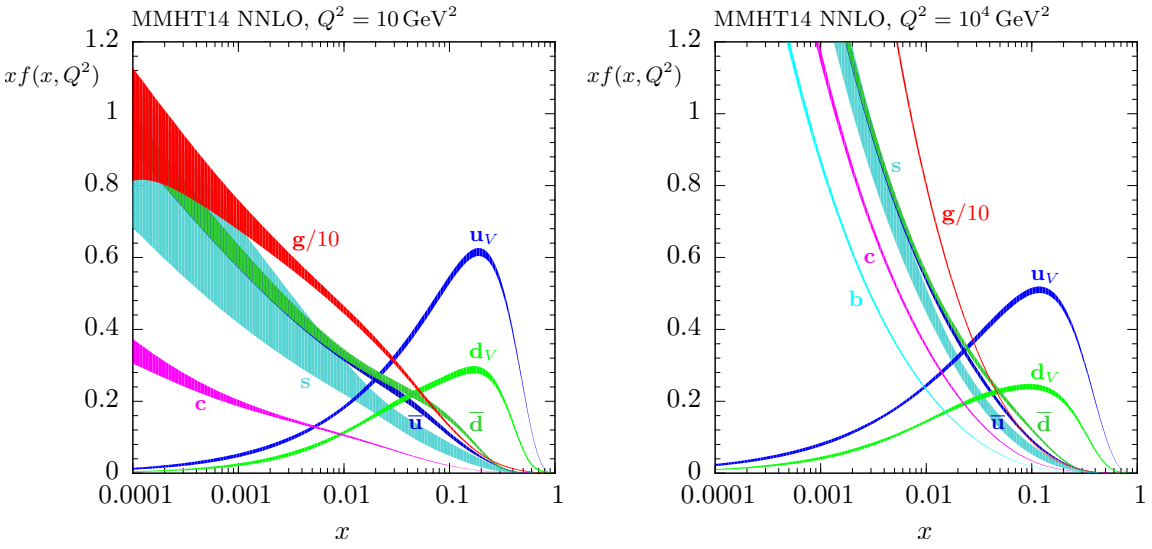

Figure 3.1: The MMHT2014 PDF set is shown as an example on the left for $\mathcal{Q}^2$=$10\,\mathrm{GeV}^2$ and on the right for $\mathcal{Q}^2$=$10^4\,\mathrm{GeV}^2$ with the associated 68% confidence-level uncertainty bands. These diagrams are taken from [38].

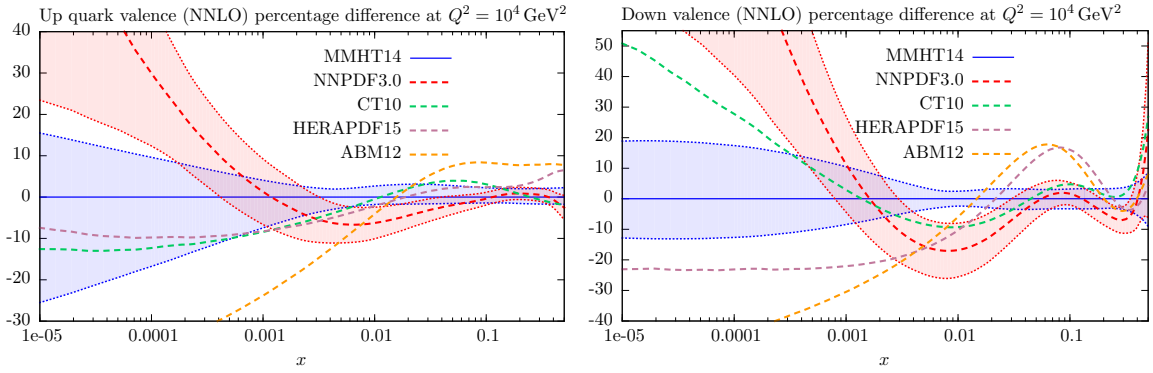

Figure 3.2: The differences of various PDF sets at NNLO for $\mathcal{Q}^2$=$10^4\,\mathrm{GeV}^2$ are shown for valence up quarks on the left and on the right for valence down quarks. These diagrams are taken from [38].

3.3 Physics Beyond the Standard Model

While the SM is one of the best tested and most precise theories in all of physics, it still has massive shortcomings. It describes only three out of the four fundamental forces, omitting gravity, and describes only visible matter which constitutes roughly 5% of the universe [39, 40]. Neither dark matter nor dark energy are explained within the SM. These facts clearly point out the need for physics beyond the SM (BSM). There are many different models predicting new physics, often with heavy charged particles. Assuming a short decay chain, the products are usually seen best in final states with leptons. If one is also interested in a model with coupling to mass or an enhanced coupling to the third generation, tau leptons are a good probe for BSM physics. This thesis thus will focus on a signature oriented search in the tau lepton and missing transverse energy channel. The discussed BSM theories will, however, not be able to yield a direct answer to dark matter nor dark energy.

3.3.1 Heavy, Charged Gauge Boson W'

One common feature of BSM models is the prediction of new heavy particles. These can either be electrically charged or neutral. In many of these models the charged particles can be vector bosons and are called W'. Assuming the shortest possible decay chain of the W' there are two distinct possibilities: the decay into quarks or leptons. Since the decay into leptons is generally a cleaner final state and the tau lepton is assumed to be a good probe for BSM physics, this final state is going to be discussed in the following.

Sequential Standard Model

In a number of different models a new heavy charged gauge boson W' is predicted and is a carbon copy of the SM W. The Feynman diagram of the production of a tau lepton and tau neutrino pair via the W' boson is shown in Fig. 3.3. In this thesis the Sequential Standard Model (SSM) [41] is going to be discussed. While there might be no strong physical motivation from any measurement for the SSM, this type of model is relatively easy to implement and analyze. This results in a long history in high energy physics analyses [42–47] and has made this model a reference model.

In principle, the W' boson can couple to a charged lepton and a neutrino, or to two quarks, or to a SM W and a SM Z boson. In a model where the mass of the W' is larger than 250 GeV the decay into a W and a Z boson is often dominant. However, one can also

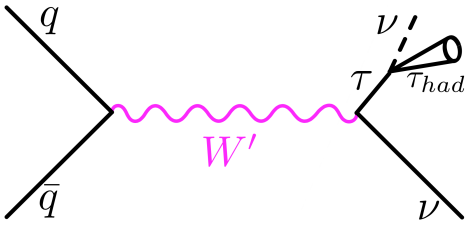

Figure 3.3: Leading order Feynman diagram of the W' production and decay. [20]

think of a suppression of the bosonic decay and, depending on the model, have the tri-vector coupling vanish completely.

The latter type of model is investigated in this thesis. The W' is assumed to couple with the same strength as the W boson to the fermions, thus $g_{W'} = g_W$. In contrast to the W boson, the W' is also allowed to decay into a top and bottom quark pair, if the mass of the new boson is larger than the one of the quark pair. This leads to a branching fraction to each leptonic channel of approximately 8%.

If the mass of the new vector boson is roughly a third of the center of mass energy $\sqrt{s}$ of a proton-proton collider, the parton-parton center of mass energy $\sqrt{\hat{s}}$ is often smaller than the bosons mass. This results in the W' being produced predominantly off-shell. This can be seen in Fig. 3.4 by the sizable contribution at transverse masses lower than their mass and by the non-peaked nature of the signal. In turn this means that the cross section of this particle cannot be approximated with the so-called narrow width approximation [48].

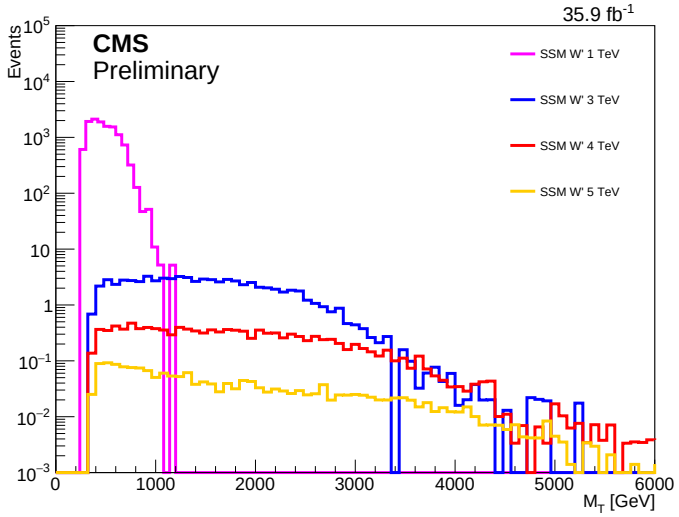

Figure 3.4: Examples for a W' signal for the masses $M_{W'}$=1, 3, 4 and 5 TeV.

Aside from the increase in off-shell contribution, the signal also gets broader with increasing W' mass, or in absolute terms $\frac{\Gamma}{m_{W'}}$=const. This can also be seen when summing all partial widths of the decay channels. The partial width of each decay channel is given by [48, 49]

$$\Gamma_{W' \to \bar{f} f'} = m_{W'} \frac{g_{W'} C_{\bar{f} f'}}{2 \cdot 48\pi} F\left(\frac{m_{\bar{f}}}{m_{W'}}, \frac{m_{f'}}{m_{W'}}\right)$$

where $m_{W'}$ is the mass of the W', $g_{W'}$ is the coupling strength of the W', $C_{\bar{f} f'}$ is the color

factor for the fermions (1 for leptons and 3 for quarks) and $F(x_1, x_2)$ is given by [48, 49]

$$F(x_1, x_2) = (2 - x_1^2 - x_2^2 - (x_1^2 - x_2)^2)\sqrt{(1 - (x_1 + x_2)^2)(1 - (x_1 - x_2)^2)}.$$

The coupling strength of the W' is assumed to be equal to the coupling strength of the W boson, thus

$$g_{W'} = g_W(\mathcal{Q}^2 = M_Z) = \sqrt{\frac{4\pi\alpha_{em}(\mathcal{Q}^2 = M_Z)}{\sin^2\theta_W}} \approx 0.66$$

with α_{em} being the fine-structure constant at $(\mathcal{Q}^2 = M_Z)$. For sufficiently high masses of the W' boson, all ratios of the fermion mass to the W' mass can be assumed to be close to 0. Due to F(0,0)=2, the total width of the W' is given by [48]

$$\Gamma_{W'} = m_{W'}\frac{g_{W'}}{4 \cdot \pi}$$

and for $g_{W'} = g_W$

$$\Gamma_{W'} = \frac{4}{3}\frac{m_{W'}}{m_W}\Gamma_W.$$

In Tab. 3.3 the widths for the signals from Fig. 3.4 are listed.

Table 3.3: Width for exemplary signals are given.

Mass $m_{W'}$	Width $\Gamma_{W'}$
1 TeV	35 GeV
3 TeV	104 GeV
4 TeV	139 GeV
5 TeV	173 GeV

Following the dependence of the width on the coupling strength, the signal shape will vary for different values of the coupling strength. Values smaller than g_W will result in the distribution being narrow, while larger values will broaden the distribution. This can be seen in Fig. 3.5.

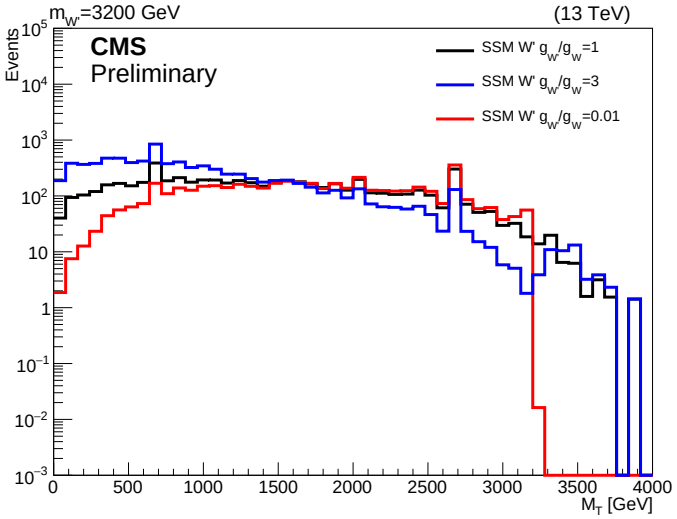

Figure 3.5: Examples for a W' signal for the mass $M_{W'}$=3.2 TeV and the ratios $\frac{g_{W'}}{g_W}$=3,1,0.1.

In case of the W and the W' bosons having the same coupling structure, there will be interference between the bosons [50, 51]. Neglecting the decay width, the differential cross section can be written as

$$\frac{\mathrm{d}\sigma}{\mathrm{d}\Omega} \cdot s \propto \left(\frac{g_{SM}^2}{s - M_W^2}\right)^2 + \left(\frac{g_{W'}^2}{s - M_{W'}^2}\right)^2 \pm \left(\frac{g_{SM}^2}{s - M_W^2} \cdot \frac{g_{W'}^2}{s - M_{W'}^2}\right)^2 .$$

The interference is given by the third term. If the couplings to the quarks and leptons in the initial and final state are the same, the positive sign needs to be applied. However, if the coupling is opposite, the sign is negative. This effect has been studied in earlier analyses and is less than 10% [44, 48]. In a $\tau + E_T^{\mathrm{miss}}$ final state this effect cannot be resolved as the interference is only noticeable in the Breit-Wigner peak, which is not visible for hadronically decaying taus, as can be seen in Fig. 3.4. The interference effect is thus negligible [52] and will be ignored in the following.

Non-universal gauge interaction model

A model predicting a W' boson is the non-universal gauge interaction model, abbreviated NUGIM. In this model the weak interaction is not described by one SU(2) gauge group but by two. One of the SU(2) couples to the light fermions that is the fermions in the first and second generation, and the other SU(2) couples to the heavy fermions, thus the fermions in the third generation. This division of the SU(2) introduces a new Higgs doublet forming, together with the SM Higgs doublet, a so-called 2 Higgs Doublet Model (2HDM). These doublets give rise to the mass of the first, second and third generation respectively, instead of generating the mass of the up-type quarks and neutrinos as done in many 2HDM. The resulting coupling structure is $\mathrm{SU}(2)_l \times \mathrm{SU}(2)_h \times \mathrm{U}(1)_Y$ and is referred to as "non-universal", G(221) or topflavor model. This model is described in detail in [53] and the W' phenomenology is explained in [54].

Analogous to the electro-weak interaction in the SM, in the new coupling structure the observable bosons can be described by mixing angles of the gauge bosons. This mixing is due to the symmetry being broken at a distinct energy scale u. This mixture is described by the mixing angle θ_E of the extended gauge group. The couplings are defined by $g_l = \frac{g}{\cos\theta_E}$ and $g_h = \frac{g}{\sin\theta_E}$. Following the symmetry breaking, the Higgs sector is comprised of two scalar particles in the 2HDM. These bosons, commonly referred to as ϕ_l and ϕ_h, have two different vacuum expectation values v_l and v_h. If the ratio of these vacuum expectation values, defined as $\tan\beta = \frac{v_h}{v_l}$, is large, the large masses of the third generation can be explained. In this case the heavy Higgs will not be the lightest observable boson of this model. Since the Higgs sector generally has little consequences on the phenomenology of the W', in this thesis the Higgs sector will be ignored and a large $\tan\beta$ is assumed. In this scenario the total width of the W' is given by [54]

$$\Gamma_{W'} = \Gamma_{Z'} = \Gamma_{W'}^{SSM} \times \frac{4 + \frac{1}{4}\cot^2\theta_E + 8\tan^2\theta_E}{12 + \frac{1}{4}}$$

where the $\tan^2\theta_E$ term originates from the light fermions and the $\cot^2\theta_E$ term originates from the heavy fermions. From this formula one finds the total cross section at the LHC, $\sigma \times B$, being proportional to $B_{SSM} \cdot \frac{\Gamma_{W'}^{SSM}}{\Gamma_{W'}}$, where B_{SSM} is the branching ratio of the SSM to the leptons. This behavior is depicted in Fig. 3.6. One can see that the branching fraction for the $\tau + \nu$ decay is larger than the branching to the light leptons for values of $\cot\theta_E > 1$, and the branching fraction of the decay becomes flat for $\cot\theta_E \approx 2$ $\tau + \nu$. Following this,

values of $\cot\theta_E > 1$ are interesting for this analysis. One also finds the total width becoming larger than 50% of the W' mass around $\cot\theta_E \approx 5$. The search will focus on the region $1 < \cot\theta_E < 5$.

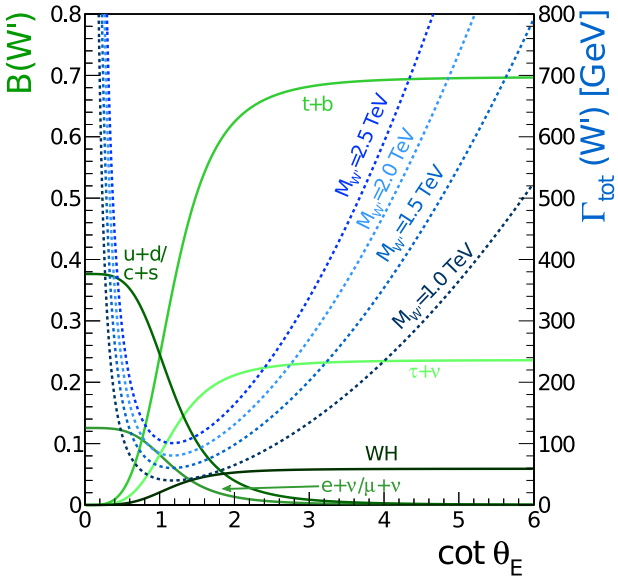

Figure 3.6: Branching fractions (left-hand scale and solid lines) and total width (right-hand scale and dotted lines) for W' decays in the NUGIM. For $\cot\theta_E$=1 the values are the same as those in the SSM, rescaled to accommodate the WH decay channel. For values of $\cot\theta_E > 5$ the total width of the W' becomes larger than 50%. This graphic is taken from [52]

.

Chapter 4

Object Reconstruction

CMS reconstructs tau leptons making use of information of the tau's decay products. This follows from the decay modes of the tau lepton, as described in Section 3.1.6, having distinctly different signatures compared to jets from quarks and gluons. The decay modes can be used to combine information from all subcomponents of the detector. This combination and the particle reconstruction is done within the Particle Flow (PF) algorithm [55–57]. After an introduction to the PF algorithm, the particle reconstruction will be discussed.

4.1 Particle Flow Algorithm

Compared to other particle reconstruction algorithms of the time, the PF algorithm utilizes a novel, almost revolutionary, approach of reconstructing physics objects. When the PF algorithm was developed, state-of-the-art algorithms reconstructed one specific object with information only from parts of the detector designed for this exact object. The PF algorithm deviated from this approach by including all available information for any object. This approach ensures that any input object, for example any calorimeter cluster, is used at most once in a given event, avoiding previously possible ambiguities. The algorithm is not only able to search for objects like an electron or photon, but is also able to resolve charged and neutral hadrons. Using the PF algorithm, one obtains a nearly complete list of particles, bar neutrinos, which can only be inferred from missing transverse energy, for one event with just one reconstruction algorithm. The information for the resulting physics objects, especially jets, is also much more detailed. These jets are obtained by clustering aforementioned hadrons, opposed to summing up information from calorimeter clusters and tracks, fulfilling jet requirements such as having a certain distance relative to an object already included in the jet-candidate. By clustering hadrons the composition of a jet and its evolution inside the detector can be resolved. This allows for robust conclusions about the origin of the jet.

To achieve this, the PF algorithm uses so-called pfCandidates which are sorted into seven types ordered by their appearance in the algorithm:

- μ: pfMuons build from tracks in the tracker and/or the muon system with no ECAL cluster
- e: pfElectrons build from „Gaussian-Sum Filter“-tracks [58], innertracker tracks and ECAL clusters
- $h^{\pm}$: pfChargedHadrons build from tracks linked with calorimeter entries

- γ: pfGammas build from ECAL clusters that are not linked to tracks
- h^0: pfNeutralHadrons build from clusters in the HCAL
- $e^{\mathrm{HF}}/\gamma^{\mathrm{HF}}$: electromagnetic particles in the hadron forward calorimeter
- h^{HF}: hadronic particles in the hadron forward calorimeter

These candidates are created in three steps. First, all hits in the subdetectors are combined separately into so-called pfElements. This is done by clustering calorimeter entries and fitting tracks from both the tracker and the muon system. In the next step, these pfElements from different detector components are linked into pfBlocks. If muons, electrons and photons can be reconstructed with their dedicated algorithms, the used information of the detector is removed from the pfBlocks and the particles are used directly as pfCandidates. The linking procedure ensures the compatibility of the energy for a given candidate but largely relies on geometrical information. The PF algorithm concludes by sorting the pfBlocks in the order of the list given above into pfCandidates. While this categorization does not yield a perfect particle identification, amongst other things, it allows for partially removing pileup in the event by ignoring all particles which have a certain distance in z from the primary vertex.

Using the approach deployed in the PF algorithm results in an improved detector resolution when compared to more traditional approaches. This can be seen best in missing transverse energy. Fig. 4.1 shows the E_T^{miss} resolution for three differently reconstructed E_T^{miss}, namely calorimeter based (type2 caloE_T^{miss}), track corrected (tcE_T^{miss}) and pfE_T^{miss}. While the shown comparison was done in 2011, it is still valid. It can be seen that the calorimeter only based E_T^{miss} has the worst resolution which is, depending on the exact value, roughly a factor 2 worse than pfE_T^{miss}which performs best.

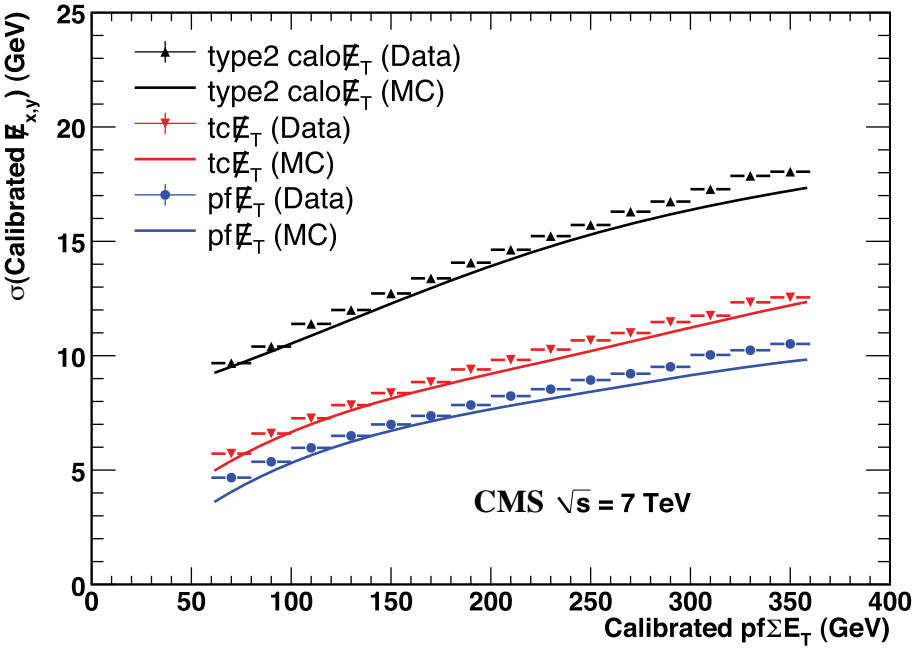

Figure 4.1: Width of the missing transverse energy resolution as a function of the $\sum E_{\mathrm{T}}$ of the particle flow reconstruction. The plot is taken from [59].

4.2 Tau Reconstruction

There are two distinct possibilities for the tau lepton decay, leptonic or hadronic. While the hadronic decays can be reconstructed and identified as a tau, it is virtually impossible for the leptonic decays to be distinguished from electrons or muons originating from the primary interaction. This is a direct consequence of the mean tau decay time being approximately 290 fs and the tau lepton therefore often not decaying before reaching the CMS detector. For the leptonic decays the electrons and muons are reconstructed using their normal reconstruction algorithms. In contrast, the hadronic decays utilize a dedicated algorithm, called hadron plus strips (HPS) [60] which builds on top of the PF algorithm. This algorithm was developed as a highly efficient tau identification at transverse momenta ranging from 20 to 100 GeV.

4.2.1 Hadron Plus Strips Algorithm

The HPS uses a pfJet as the initial seed which is split into charged hadrons ($h^{\pm}$) and neutral contributions from pions (π^0). The π^0 contributions are determined in an area corresponding to 0.05×0.2 in the $\eta \times \phi$ plane in Run I, which is referred to as strip. In Run II the area for the strip has been relaxed depending on the p_T of the γ or converted e from the π^0 decay to $\Delta\eta(p_{\mathrm{T}}) = 0.20 \cdot \left(\frac{p}{GeV}\right)_{\mathrm{T}}^{-0.66}$ and $\Delta\phi(p_{\mathrm{T}}) = 0.35 \cdot \left(\frac{p}{GeV}\right)_{\mathrm{T}}^{-0.71}$ [61]. For a pfGamma to be used in a strip, its energy has to be greater than 0.5 GeV and for a strip to be considered, it has to have a total energy greater than 2.5 GeV. The threshold for the charged hadrons is 0.5 GeV in p_T. It should be noted that the HPS neglects all contributions from pfNeutralHadrons, as these are built from clusters in the HCAL but the π^0 almost exclusively decays into a pair of photons which are detected in the ECAL.

The charged hadrons and strips are combined into decay modes. The combined mass of these decay modes has to be in a decay mode dependent mass window. These mass windows correspond to possible intermediate resonances and are listed in Tab. 4.1 If there is more than one combination possible, the highest energetic combination is chosen as the hadronic tau.

Table 4.1: The decay modes and their corresponding mass windows in the reconstruction are shown.

Decay mode	Mass window
$1h\ 0\pi^0$	$M_{\pi^{\pm}}$
$1h\ 1\pi^0$	0.3 MeV-1.3 MeV
$1h\ 2\pi^0$	0.4 MeV-1.2 MeV
$3h\ 0\pi^0$	0.8 MeV-1.5 MeV

This step is technically part of the particle identification for the tau, but since it is so commonly used, it is essentially part of the criteria for the HPS algorithm. This is one half of the so-called „DecayModeFinding“ discriminator. The other half of this discriminator requires the hadron and strips to be in a cone with a size of $\Delta R < 3\,\mathrm{GeV}/p_T$. This definition is truncated at ΔR=0.1 for low p_T taus and at ΔR=0.05 for high p_T taus to accommodate for the detector resolution. Based on the results of a CMS internal Analysis Note [62], the use of this discriminator is strongly suggested.

4.2.2 Tau Identification

Once a tau candidate is reconstructed, it also has to be identified as a tau. For this, so-called discriminators are used which are provided by the HPS algorithm. Any of these discriminators imposes a unique set of requirements and has a specific reconstruction efficiency. The discriminators can be grouped into three different types. The first type is the already mentioned „DecayModeFinding“ discriminator. The other two types are the isolation-based and the anti-light-lepton discriminators. In Tab. 4.2 a list of the discriminators with their selection criteria is given.

Table 4.2: A list of the most important discriminators for the identification of a HPS tau and their selection criteria are given [63].

Name	Selection
ByLooseElectronRejection	MVA selection based on electron and pion
ByMediumElectronRejection	MVA selection based on electron and pion
ByTightElectronRejection	MVA selection based on electron and pion
ByLooseMuonRejection	Tau Lead Track not matched to chamber hits
ByMediumMuonRejection	Tau Lead Track not matched to global/tracker muon
ByTightMuonRejection	Tau Lead Track not matched to global/tracker muon and large enough energy deposit in ECAL + HCAL
ByDecayModeFinding	Narrowness and jet mass requirement
ByLooseIsolationMVA	BDT based selection using isolation in rings around tau direction and shower shape variables
ByMediumIsolationMVA	BDT based selection using isolation in rings around tau direction and shower shape variables
ByTightIsolationMVA	BDT based selection using isolation in rings around tau direction and shower shape variables

The discriminators „ByDecayModeFinding“, „ByMediumIsolationMVA“, „ByMediumElectronRejection“ and „ByMediumMuonRejection“ are required to be fulfilled for a tau to be identified as such in this analysis.

Isolation Discriminators

The „DecayModeFinding“ discriminator has been optimized for high efficiency, resulting in the fake probability for QCD jets still being very high and needing to be suppressed. Following the different composition of a jet originating from QCD or from a tau decay, the isolation differs quite significantly. While a jet from a tau decay is largely contained in a cone of $\Delta R < 0.3$, a QCD-jet commonly is accompanied by many other particles. This can be used either in a cut-based approach or in a multivariate approach (MVA). The MVA uses a boosted decision tree (BDT) on multiple jet properties such as shower shape variables to discriminate against QCD jets. In contrast, the cut-based „CombinedIsolationDBSumPtCorr“ discriminators use properties of the jet and information on pileup for the discrimination. The isolation of the tau is evaluated using a cone of size $\Delta R < 0.3$ in which the p_T of all charged PF objects and photons ($p_T^{\gamma} > 0.5\,\mathrm{GeV}$) is summed up. Pileup then is corrected for, by using the $\Delta\beta$ corrections. For this correction it is assumed that the neutral parts of the jet account for roughly 50% of the charged part. These neutral parts are subtracted from the isolation cone.

For the majority of this analysis the medium isolation working point of the MVA (ByMediumIsolationMVA) has been chosen.

Anti-Electron and Anti-Muon Discriminators

Another source of misidentified hadronic taus are the light leptons, both of which can be discriminated. For muons, this can be achieved by checking the leading track within the tau candidate. If this track can be matched to a muon candidate reconstructed within the muon system, the tau candidate will be rejected. For electrons, the situation is a bit more complicated. The electron can be misidentified as a tau if the track is taken as the dominant track and photons produced by Bremsstrahlung are identified as one or more π^0. A BDT has been trained on properties of the shower shape and the fraction of energy deposited in the ECAL and the HCAL to distinguish between electrons and taus. This BDT is used in this analysis.

4.2.3 Modificaations of the Identification Method for High-p_T Taus

As the HPS was originally designed for energies smaller than 100 GeV, there was no guarantee that it is highly efficient and yields the correct prediction for the transverse momentum for high p_T taus. In fact it has been shown that the transverse momentum is underestimated by roughly 30% at 1 TeV. This has been investigated in [52]. It has been found that the underestimation can largely be explained by three different effects:

- Track merging
- Track momentum underestimation
- Mass window

Each of the effects can be counteracted. For highly energetic taus the tracks of the 3 prong decay can merge due to the boost of the tau and finite resolution of the pixel detector. If this happens, the efficiency can be regained by either allowing for the unphysical two prong decay or by counting the prongs based on a combination of tracks and charged hadrons where potential double-counting is taken care of. Due to different dependencies of the resolution on the energy, the general assumption of the PF algorithm that the tracker has the best energy resolution can be wrong. This is typically the case for energies greater than 400 GeV. Adding the previously ignored h^0 candidates with p_T>50 GeV to the tau candidate can further raise the efficiency. Lastly, it has been shown that the mass windows of the HPS as listed in 4.1 are too narrow for high p_T taus. This issue can be resolved by introducing a p_T dependent correction shown in Tab. 4.3. These changes to the „DecayModeFinding“ discriminator resulted in a change in the naming scheme, calling this version the „new“ while the previous version is labeled as „old“.

The full description of the performance of the tau reconstruction in Run II can be found in [61].

Table 4.3: The decay modes and their corresponding mass windows in the reconstruction are shown.

Decay mode	Mass window
$1h\ 0\pi^0$	$M_{\pi^\pm}$
$1h\ 1\pi^0$	$0.3\,\text{MeV}\text{-max}(1.3,\text{min}(1.3\cdot\sqrt{\frac{p_T}{100\,\text{GeV}}},4.2))\text{MeV}$
$1h\ 2\pi^0$	$0.4\,\text{MeV}\text{-max}(1.2,\text{min}(1.2\cdot\sqrt{\frac{p_T}{100\,\text{GeV}}},4.0))\text{MeV}$
$2h\ 0\pi^0$	$0\,\text{MeV}\text{-}1.2\,\text{MeV}$
$2h\ 1\pi^0$	$0\,\text{MeV}\text{-max}(1.2,\text{min}(1.2\cdot\sqrt{\frac{p_T}{100\,\text{GeV}}},4.0))\text{MeV}$
$3h\ 0\pi^0$	$0.8\,\text{MeV}\text{-}1.5\,\text{MeV}$

4.3 Reconstruction of other Objects

As the electrons and muons are also used in this analysis the reconstruction of these particles is discussed briefly in the following. This section will then be concluded by introducing the reconstruction of missing transverse energy.

4.3.1 Electron Reconstruction

The reconstruction of the electrons [64] relies on the tracker and the ECAL and utilizes their excellent resolution. The algorithm starts by reconstructing the tracks with either the Kalman Filter [65] or the Gaussian Sum Filter (GSF) [58] method. The latter is a modification of the Kalman filter taking the radiation of Bremsstrahlung into account. The tracks then are used to obtain information of the clusters of deposited energy in the ECAL likely originating from the electron candidate. Without the magnetic field about 97% of the electro-magnetic shower is contained in a 5×5 crystal array in the ECAL. With the magnetic field, however, a spread in ϕ direction is anticipated due the bending of the electron and the resulting continuous photon radiation. The deposited energy is combined in so called superclusters. This combination differs slightly in barrel and endcap due to differences in the ECAL shape.

The performance of the electron reconstruction can be found in [66, 67]

4.3.2 Muon Reconstruction

For the muon reconstruction there are three widely used „types“ of muons, the so-called standalone, global and tracker muons. For all three types the Kalman Filter technique is used to build the tracks iteratively. Usually these tracks are seeded in the muon system which is heavily taken advantage of since the muon is the only charged particle regularly reaching this part of the detector. If just the muon system is used to identify a muon, this muon is called standalone. Extending the muon system track of the muon candidates and accounting for interaction with the active material, such as multiple scattering, often a match to a track in the pixel detector can be found. In this case the muon is called a global muon. If the reconstruction starts in the tracker and the hits in the muon can be matched, the muon is called a tracker muon.

The performance of the muon reconstruction can be found in [68, 69]

4.3.3 Missing Transverse Energy Reconstruction

Following the conservation of the transverse momentum in an idealized head-on proton-proton collision, the transverse energy in an event is expected to be zero. If in a given event particles are either not reconstructed or not detected, as often is the case for neutrinos, the measured transverse energy will differ from zero. This results in the quantity commonly referred to as missing transverse energy, or E_T^{miss} for short. Following the presented argument, missing transverse energy is defined as

$$E_T^{\text{miss}} = \left| -\sum \vec{p}_T \right|$$

where $\vec{p}_T$ are the vectorial transverse momenta of all pfCandidates. The direction of E_T^{miss} in the azimuthal plane (θ or η) is per definition not relevant. The polar direction, however, can be important in analyses. For this purpose a vectorial transverse momentum can be defined as $\vec{p}_T^{\,\text{miss}} = -\sum \vec{p}_T$. As the only particles in the SM that are expected not to be detected in CMS are neutrinos, the transverse momentum and transverse energy are essentially equal, $\vec{p}_T^{\,\text{miss}} \approx \vec{E}_T^{\,\text{miss}}$. In a final state with only a single charged lepton the E_T^{miss} is determined by the p_T of the lepton.

Chapter 5

Datasets and Analysis Framework

5.1 Analysis Framework

The analysis of the largest dataset taken with CMS ever at a center-of-mass energy of 13 GeV requires suitable software to handle the amount of data. This is done in two parts: one originating from the CMS collaboration and is called the CMS software, or CMSSW [70] for short, and the other originated in the Aachen workgroup and is called „Three A Physics Analysis Software“or TAPAS [71] for short. Using CMSSW the CMS collaboration provides the data in different formats with „MiniAOD“, where AOD is short for „Analysis Object Data“, being the one used the most. For a given analysis the amount of information not used for this particular analysis saved in these MiniAOD's is typically quite large. In order to reduce the size of the files stored in the Aachen Tier 2 server, the MiniAOD files have to be skimmed. The skimming step is done in the TAPAS framework. The output is generated with the help of the PXL library [72] and is saved in the format „pxlio“, which provides the possibility to store data of the recorded particles.

5.2 Used Datasets

This analysis has been performed using data taken with a center-of-mass energy of 13 TeV collected with the CMS detector. The data has been certified by the Physcis Data and Monte Carlo Validation group and the JSON file [1], in which only certified events are listed, has been used. The dataset had be to reconstructed twice. The second reconstruction mainly addressed two issues that arose after the first reconstruction:

- The so-called „ECAL gain switch“ issue which is related to the underestimation of reconstructed hits in the tracker at very high p_T. This affects the whole Run 2 dataset in the barrel region but not the Monte Carlo (MC) prediction.
- The so-called „Bad PF muon“ or „spurious muon“ issue. This has been discovered in the E_T^{miss} tails, which is spoiled by bad quality PF muons. These bad quality PF muons are often duplicates of good muons. The rate of these bad muons is much higher for first part of the 2016 data-taking. This part of the data-taking was affected by a strip dynamic inefficiency, following the „Heavy Ionizing Particle“ (HIP) effect.

The datasets used for the tau channel are listed in Tab. 5.1 and correspond to an integrated luminosity of 35.9 fb^{-1} with an uncertainty of 2.5% as measured in [73]. These

[1] $Cert\_271036-284044\_13TeV\_23Sep2016ReReco\_Collisions16\_JSON.txt$

datasets are identical to the ones used in [74]. Requiring only tau identification criteria and the tau and E_T^{miss} cross trigger described in Section 6.1, 4×10^3 events have been taken in this dataset.

Table 5.1: The datasets used in this analysis are listed.

Dataset	Run-Range	Integrated Luminosity
/Tau/Run2016B-03Feb2017 ver2-v2/MINIAOD	273158 - 275376	$5.79\,\text{fb}^{-1}$
/Tau/Run2016C-03Feb2017-v1/MINIAOD	275657 - 276283	$2.57\,\text{fb}^{-1}$
/Tau/Run2016D-03Feb2017-v1/MINIAOD	276315 - 276811	$4.25\,\text{fb}^{-1}$
/Tau/Run2016E-03Feb2017-v1/MINIAOD	276831 - 277420	$4.01\,\text{fb}^{-1}$
/Tau/Run2016F-03Feb2017-v1/MINIAOD	277981 - 278808	$3.10\,\text{fb}^{-1}$
/Tau/Run2016G-03Feb2017-v1/MINIAOD	278820 - 280385	$7.54\,\text{fb}^{-1}$
/Tau/Run2016H-03Feb2017 ver2-v1/MINIAOD	281613 - 283685	$8.39\,\text{fb}^{-1}$
/Tau/Run2016H-03Feb2017 ver3-v1/MINIAOD	284036 - 284044	$0.22\,\text{fb}^{-1}$
Total	27158 - 284044	$35.87\,\text{fb}^{-1}$

5.3 Background Processes

There are a few processes in the SM yielding the final state of the type „lepton + missing transverse energy“. This type of final state can also be obtained by misreconstruction or particles being out of acceptance of the detector. The knowledge and modeling of these SM processes is therefore important for the search for a BSM signal. Thus, the simulation and relevant backgrounds will be described in this section.

5.3.1 Process Simulation

In order to determine the number of expected background events in this analysis, as well as the expected shape of a W' signal in the CMS detector, the relevant processes are generated using simulation. For this purpose MC generators are used. When producing the samples used to predict the number of events, usually one cannot know beforehand the integrated luminosity. For this reason and due to reduced statistical uncertainties, the focus is on producing as many events for a given process as reasonably possible and weighting the produced events by the factor

$$w = \frac{\sigma \cdot \mathcal{L}}{\text{N}_{\text{MC}}}$$

where σ is the cross section of the given process, $\mathcal{L}$ is the integrated luminosity of the used collision data and N_{MC} is the number of generated events.

Depending on the process, the events are generated at leading (LO) or next-to-leading order (NLO), and if known, a flat k-factor is applied to account for the inclusive NLO or next-to-next-to leading order (NNLO) cross sections. One should note that a NLO or NNLO k-factor requires a lot of theoretical work and the achieved order highly depends on the available computing ressources. For the most important background, originating from the decay of a W boson, a k-factor depending on the boson's mass has been evaluated. This has been described in detail in [75] and will be summarized in 5.4.1.

It is crucial to describe the decay of the tau lepton in the W background well. For this decay there are three components that need to be modeled as accurately as possible. These

components are the detector response, as done by GEANT4 [76–78], the hadronization, as done by PYTHIA [79, 80], and the decay of the tau lepton, as done by the dedicated library TAUOLA [81]. While the first two are commonly used even for processes not involving taus, the latter one is specific for taus. The interplay between the three parts ensures the best available prediction of the tau leptons in the CMS detector.

5.4 SM Background Prediction

Not only the W' decay has the desired tau and MET final state, but several other SM processes can result in this final state. While having only one lepton and MET as a signal has advantages when reconstructing this type of events, the disadvantage is the very limited number of selections available to reject background processes. This is of little consequence for the main source of background, namely the production and subsequent decay of off-shell SM W bosons. This is due to the W' boson being by construction a heavy copy of the W boson and thus experimentally not distinguishable from a SM W boson. Only the number of events in a given mass region, the signal region to be exact, can give conclusions to the existence of the SSM boson. However, there are more processes that have to be taken into account. These processes are the QCD multijet, $t\bar{t}$, single top, diboson and Drell-Yan processes, which can lead to the same signature in the detector. While the QCD multijet process has an extremely large cross section, the selection on the expected kinematic properties of the signal can reduce this background significantly.

The following sources of backgrounds are included in this analysis. If not stated otherwise, k-factors have been taken from [82]:

- W$\rightarrow \ell\nu$ ($\ell = e, \mu, \tau$): In order to to achieve the best possible description, this process is split into three regions: the so-called bulk with W masses below 100 GeV and hadronic jet activities (H_T) less than 100 GeV, a region with m_W <100 GeV and H_T >100 GeV, and the off-shell production with m_W >100 GeV. This is illustrated in Fig. 5.1. The bulk region is produced with aMC@NLO [83] at NLO and a m_W dependent k-factor is applied. The samples with H_T >100 GeV are produced with Madgraph 5 version 1.5.11 [84] at LO, but a flat k-factor is applied to scale the cross section to NLO. This set of samples has the following bins in H_T/GeV: 100-200, 200-400, 400-600, 600-800, 800-1200, 1200-2500 . The off-shell production is produced at LO with Pythia 8 and the m_W dependent k-factor [75] is applied. This region is also binned, this time in the W mass. The bins are as follows in m_W/GeV: 100-200, 200-500, 500-1000, 1000-2000, 2000-3000, 3000-4000, 4000-5000, 5000-6000, 6000-∞.

- Drell-Yan process with taus in the final state: This type of process becomes relevant if one of the two taus is not identified or reconstructed as a tau. Madgraph 5 version 1.5.11 has been used to produce these samples at LO which are binned in the boson mass in the bins 10-50 GeV and 50 GeV to ∞. A flat k-factor has been applied to reach a NNLO precision in the cross section.

- Single-top and top-antitop production: The decay of either the (anti-)top or the subsequent decay of the bottom quark can result in a high p_T lepton and MET. These samples have been produced with POWHEG in NLO [85–89]. When available, NNLO k-factors are applied.

- Diboson production: The WW,WZ and ZZ processes are produced in Pythia 8 at LO with NLO k-factors being applied if available. The W and Z bosons can decay include not only the decay to tau leptons but also to other possible particles.

- QCD multijet: The QCD jet can be misidentified as a tau particle and enter the analysis this way. The E_T^{miss} of these events is typically low. This process is generated at LO and binned in H_T/GeV with the following bins: 100-200, 200-300, 300-500, 500-700, 700-1000, 1000-1500, 1500-2000, 2000-∞

- Z+jets to $\nu\nu$: The Z+jets process can enter the analysis if a jet is misidentified as a tau particle and has sufficient E_T^{miss} due to the pair of neutrinos. This process is generated at LO with a flat NLO k-factor applied. This process also is binned in H_T/GeV with the following bins: 100-200, 200-400, 400-600, 600-800, 800-1200, 1200-2500, 2500-∞

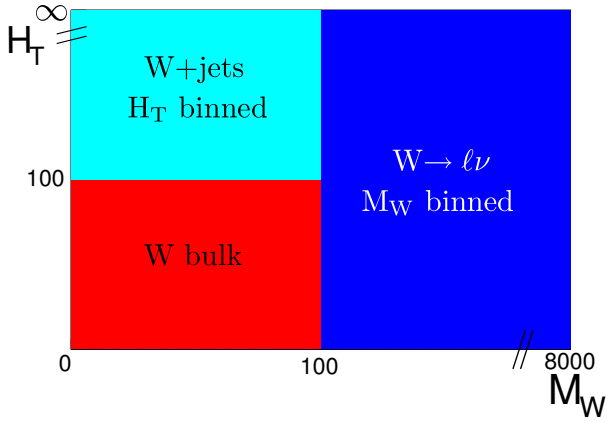

Figure 5.1: The regions for the SM W background are illustrated. There are three regions, two of which correspond to the bulk samples with $M_{W'}$<100 GeV and differ in the hadronic jet activity in the event, and the third corresponding to the off-shell production. Each region is subdivided by different samples.

5.4.1 Higher Order Corrections for the W Boson

Based on [48, 52, 75], the higher order corrections for the W boson will be summarized.

In principle there are two sources of corrections, the QCD and the electro-weak ones. Until now there is no tool to combine a matrix level combination of these corrections. As a direct consequence the corrections are determined independently and combined afterwards. There are two possibilities to do this, in an additive ($\left[\frac{\mathrm{d}\sigma}{\mathrm{d}M}\right]_{\text{QCD}\oplus\text{EW}}$) or in a multiplicative approach ($\left[\frac{\mathrm{d}\sigma}{\mathrm{d}M}\right]_{\text{QCD}\otimes\text{EW}}$) [90, 91]. The additive approach has been recommended by [91] and the multiplicative approach is used as a measure for the systematic uncertainty. The two approaches can be formulated as

$$\left[\frac{\mathrm{d}\sigma}{\mathrm{d}M}\right]_{\text{QCD}\oplus\text{EW}} = \left[\frac{\mathrm{d}\sigma}{\mathrm{d}M}\right]_{\text{QCD}} + \left[\frac{\mathrm{d}\sigma}{\mathrm{d}M}\right]_{\text{EW}} - \left[\frac{\mathrm{d}\sigma}{\mathrm{d}M}\right]_{\text{LO}}$$

$$\left[\frac{\mathrm{d}\sigma}{\mathrm{d}M}\right]_{\text{QCD}\otimes\text{EW}} = \left(\frac{\left[\frac{\mathrm{d}\sigma}{\mathrm{d}M}\right]_{\text{QCD}}}{\left[\frac{\mathrm{d}\sigma}{\mathrm{d}M}\right]_{\text{LO}}}\right) \times \left[\frac{\mathrm{d}\sigma}{\mathrm{d}M}\right]_{\text{EW}}$$

where $\left[\frac{d\sigma}{dM}\right]_{QCD}$ and $\left[\frac{d\sigma}{dM}\right]_{EW}$ are the differential cross sections with corrections for NNLO QCD and NLO electroweak processes in which the LO cross section is included.

The W' mass dependence has been chosen, as this variable is well defined for several different generators. To derive the NNLO QCD correction, FEWZ [92], and for the NLO electro-weak correction MCSANC [93] has been used. The resulting k-factor is shown in Fig. 5.2 and ranges from 0.55 to 1.15.

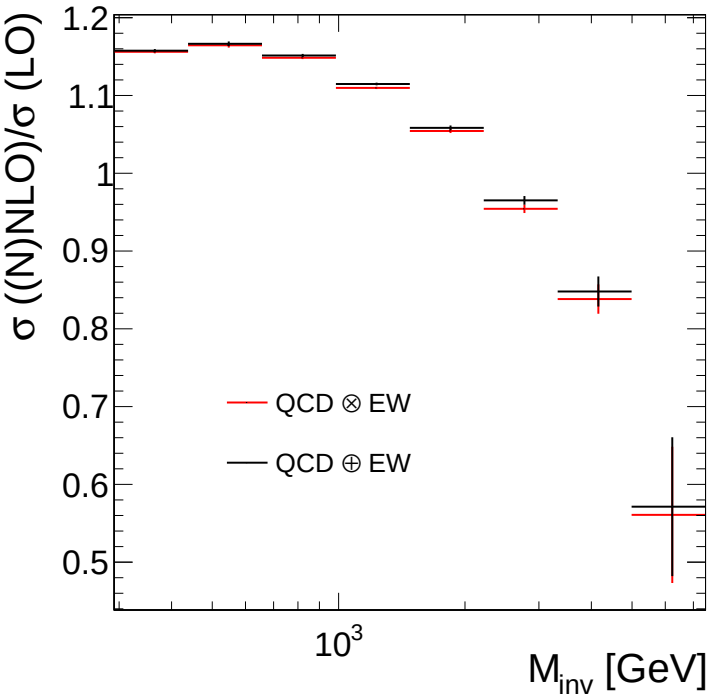

Figure 5.2: The additive and multiplicative k-factors are produced with FEWZ and MCSANC and depend on the W' mass. The additive approach is given in black, while the multiplicative approach is given in red. This plot is taken from [75]

5.5 Signal Samples

The SSM samples are, just like the SM W samples, produced with Pythia 8 in LO for masses in the range of 400 to 5800 GeV. For the SSM model also a NNLO k-factor has been derived [94]. Analogous to the SM case, the SSM k-factor is dependent on the W' bosons mass. For each mass the signal efficiency can be determined using the produced samples. To derive limits on the coupling strength, Madgraph has been used with a W' implementation [95]. For the fraction of couplings 10^{-4},10^{-3},10^{-2},10^{-1},1,2,3 and 5, samples have been produced by the author to reweight the officially produced SSM W' samples.

Chapter 6

Analysis

6.1 Trigger Selection

In this analysis three different combinations of triggers are used. Two of these combinations, namely the electron and muon triggers, are used for a data-driven estimate of background processes and the last type is used to select events with exactly one tau, using a tau and MET cross trigger. The used datasets and trigger tresholds are listed in Tab. 6.1 and their names are given Tab. 6.2. Events triggered by a tau lepton are corrected for trigger turn-on effects by selecting for events with the tau p_T>80 GeV and E_T^{miss}>120 GeV. A scale factor has been derived in [96] and applied in this analysis to account for possible mismodeling of the trigger in MC and is found to be 0.9. This is shown in Fig. 6.1.

Table 6.1: The on- and offline trigger thresholds are listed as well as the datasets in which the triggers are used.

Primary Dataset	p_T/GeV threshold		E_T^{miss}/GeV threshold	
	online	offline	online	offline
Single Electron	27	35	0	0
	45	55	0	0
	115	130	0	0
Single Muon	50	55	0	0
Tau	50	80	90	200

Table 6.2: The trigger names are listed as well as the datasets in which the triggers are used.

Primary Dataset	Name
Single Electron	HLT_Ele27_WPTight_Gsf
	HLT_Ele45_WPLoose_Gsf
	HLT_Ele115_CaloIdVT_GsfTrkIdT
Single Muon	HLT_Mu50
	HLT_TkMu50
Tau	HLT_LooseIsoPFTau50_Trk30_eta2p1_MET120

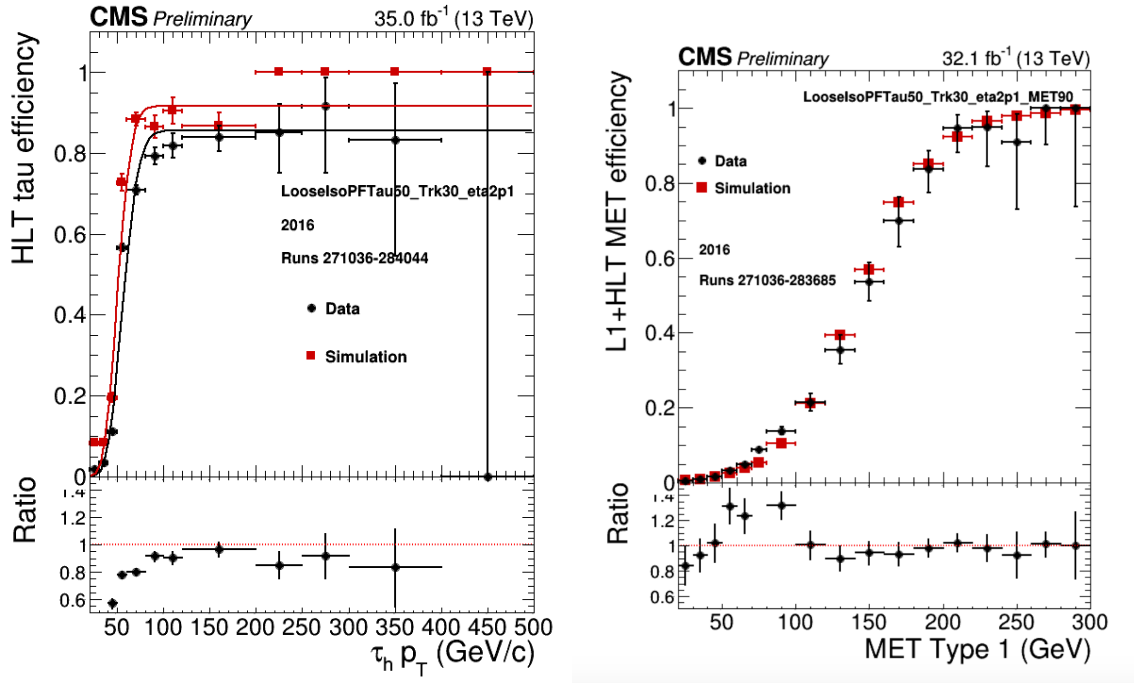

Figure 6.1: On left and right the trigger effiencies are studied in dependence of the tau p_T and E_T^{miss}, respectively. For tau p_T a scale factor of 0.9 has been found. These plots have been produced by Sami Lehti for [74].

6.2 Kinematic Selection

When searching for a signal, the separation between signal and background processes should be as large as possible. To ensure this, the kinematic selection for the tau and E_T^{miss} channel has been optimized in [52, 97]. While heavily correlated with the discriminating variable M_T, defined as $\sqrt{2p_T E_T^{\text{miss}}(1-\cos\Delta\phi)}$, the variables used for the kinematic selection are $\Delta\Phi(\tau, E_T^{\text{miss}})$ and p_T/E_T^{miss}. These variables are used to exploit the back-to-back kinematics of the decay of the W' boson decaying into a tau lepton and a neutrino. Since the W' is heavy enough to have little momentum, the two body decay products will have equal momenta. When the tau decays further, the E_T^{miss} is also expected to be back-to-back to the visible part of the tau, however smaller than the „original“ E_T^{miss} due to additional neutrino(s) in the final state. This follows from the strong boost of the tau lepton which results in boosted decay products. This is illustrated in Fig. 6.2.

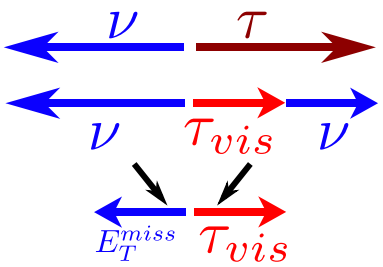

Figure 6.2: The back-to-back kinematics of the W' to tau decay is illustrated. The measured E_T^{miss} is reduced with respect to the E_T^{miss} assuming the tau does not decay.

The values obtained by the optimization [52,97] are $\Delta\Phi(\tau, E_T^{\text{miss}}) > 2.5$ and $0.7 < p_T/E_T^{\text{miss}} < 1.3$.

6.3 Determination of the Multijet Backgrounds from Data

6.3.1 Method

The multijet backgrounds originating from Z+jets, with the Z decaying to a pair of neutrinos, or from QCD events, are important backgrounds in this analysis. As no higher order corrections are available for this background and the statistics have been found to be insufficient in the past, this background has traditionally been derived from data. This lack of statistics is especially apparent in the p_T and E_T^{miss} variables in the later defined signal region. These distributions will be shown later. Subsequently large values of p_T/E_T^{miss} suffer from the lack of statistics as well. This region is expected to be dominated by the multijet backgrounds.

The method used is the ABCD method which is illustrated in Fig. 6.3 and has already been used in [20] and in [46] in a slightly different variation. A similar method has also been used in [44] with $\sqrt{s}$=8 TeV CMS data.

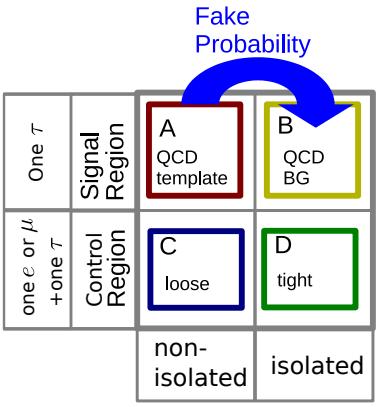

Figure 6.3: The ABCD method used to determine the multijet background is illustrated. There are two regions defined, a signal and a control region. Both regions require exactly one tau, but the control region additionally requires either one electron or one muon. To differentiate between a template for the shape and the background in the signal region, the isolation is introduced as a second discriminant.

The basic approach can be described as follows: First, a signal and a control region are defined. The control regions are derived from the „Single Electron“ and „Single Muon“ datasets, while the signal region is taken from the „Tau“ dataset. These regions are further subdivided and the four subcategories are defined. The ratios of the control regions ($\frac{D}{C}$) and signal regions ($\frac{B}{A}$) are expected to be equal. One can see that there are two variables (in a general sense) required to perform this type of approach. In this analysis the signal region is defined as having exactly one tau and the control region additionally requires an electron or muon to be in the event. While the signal region requires events to be triggered by the tau leptons, in the control region the electron or muon has to trigger the event. The triggers used for this purpose have been described in 6.1 and their online and offline thresholds in p_T and E_T^{miss} are given in Tab. 6.1. The subdivision is performed using the isolation of the tau. If the isolation is fulfilled, the event is treated as a signal event originating from a multijet process. However, if the isolation fails, the multijet template for the shape can be retrieved. In the control region the corresponding subregions are called „tight“ and „loose“

if the isolation is fulfilled or fails. The p_T dependent distributions in these subregions are shown in Fig. 6.4. Furthermore, the expected number of „true“ taus are subtracted. A true tau is defined as a tau in a simulated sample which can be matched to a generated tau. A p_T dependent true-tau subtracted „tight-to-loose“ ratio, or R_{tl} for short, is computed. This ratio is shown in Fig. 6.5 and varies from less than 1% at low p_T to 0.1% at high p_T. In the last step this ratio of the tight and loose categories in the control region can be applied to the template to access the background yield in the signal region.

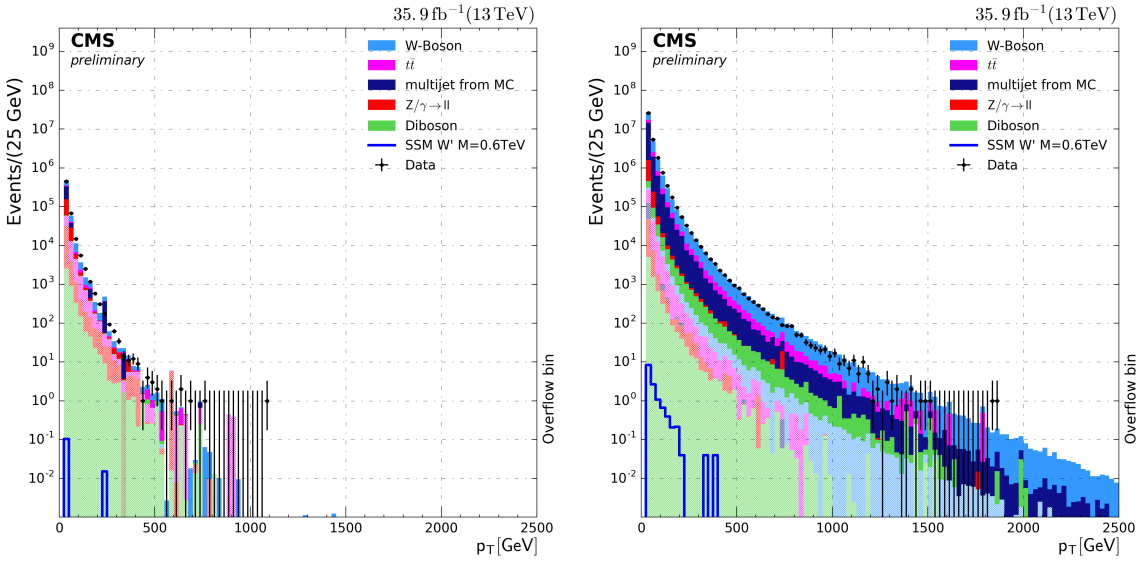

Figure 6.4: The p_T distributions for isolated and non-isolated events are shown on the left and right, respectively. The true tau contribution is shown as the brighter, hatched area. The data is shown as black dots.

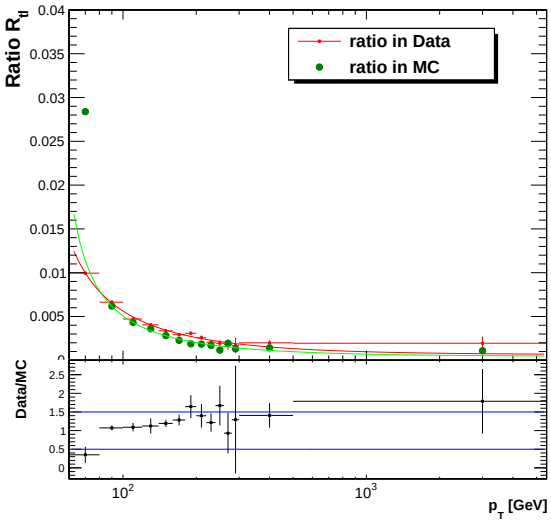

Figure 6.5: The tight-to-loose ratio is shown for simulation and data in red and green respectively. On the bottom the ratio of R_{tl} from Data and simulation is shown. They are largely contained within the blue lines indicating the derived 50% systematic uncertainty.

6.3.2 Derivation of the Systematic Uncertainty

The differences in the tight-to-loose ratio R_{tl} in Data and simulation are assumed to originate from a suboptimal description of the events. In order to account for this, a systematic uncertainty has been derived. This uses the fraction of R_{tl} in Data and simulation, as illustrated in Fig. 6.5, as an input. As the fraction of R_{tl} is largely contained within 50%, this value has been deduced as the systematic uncertainty originating from modeling of the multijet background.

6.3.3 Monte Carlo Based Closure Test

While the method aims to estimate the multijet background from data, the validity of the procedure itself has to be verified. This is done with a simulation based closure test. The test is preformed by applying R_{tl} to simulated multijet events in region A and comparing the event yields in region B. A comparison between simulation and the output of the ABCD method is shown in Fig. 6.6 for the variables E_T^{miss}, p_T and M_T. Aside from spikes in the simulation based distribution, overall good agreement can be found with the results from the ABCD method.

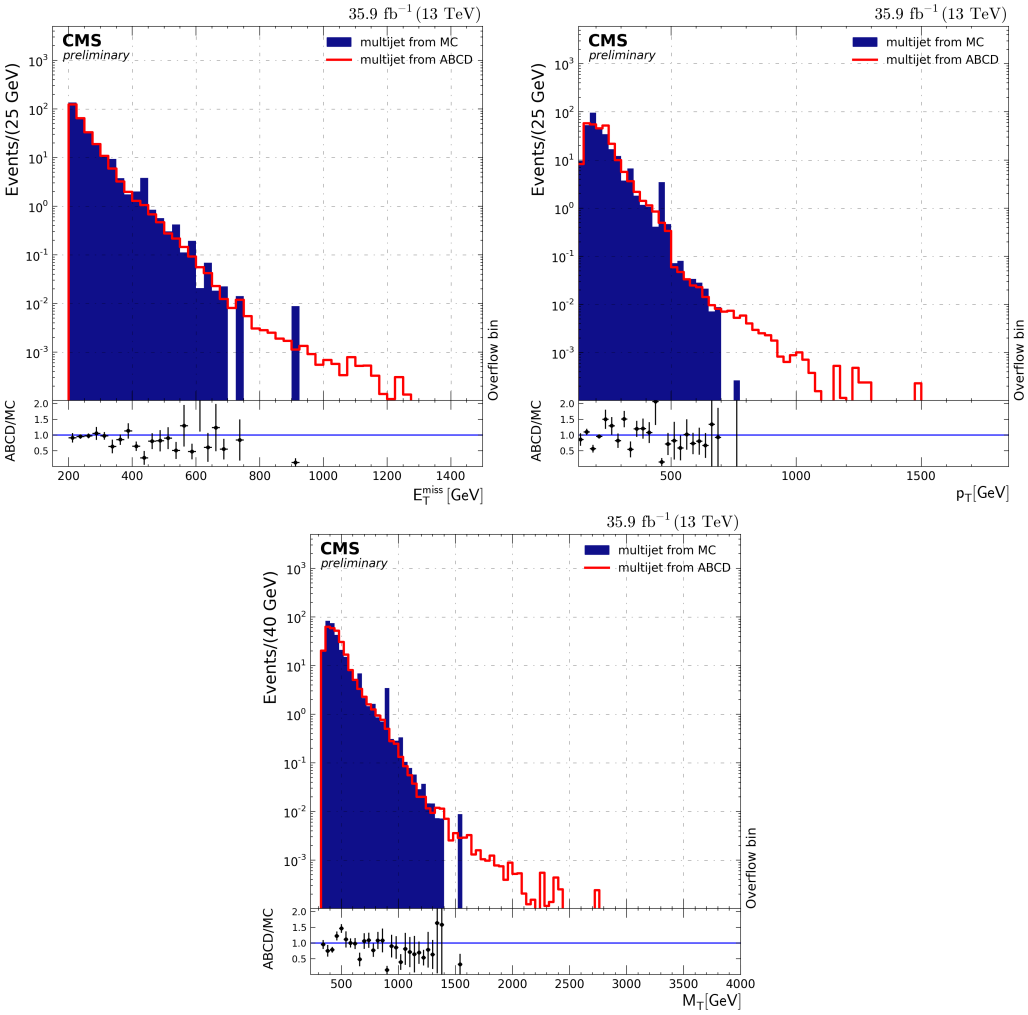

Figure 6.6: The distributions for the mulitjet processes from simulated samples and estimated from the simulation based ABCD method are compared for the variables E_T^{miss}, p_T and M_T. While there are minor differences, overall a good agreement can be found.

6.3.4 Background Estimate from Data

As the method has been found to close on MC and the systematic uncertainties are derived, the multijet contributions can be derived from data. This is based on the R_{tl} as seen in Fig. 6.5. The resulting distributions with their systematic uncertainties are shown in Fig. 6.7 as a function of E_T^{miss},p_T and M_T.

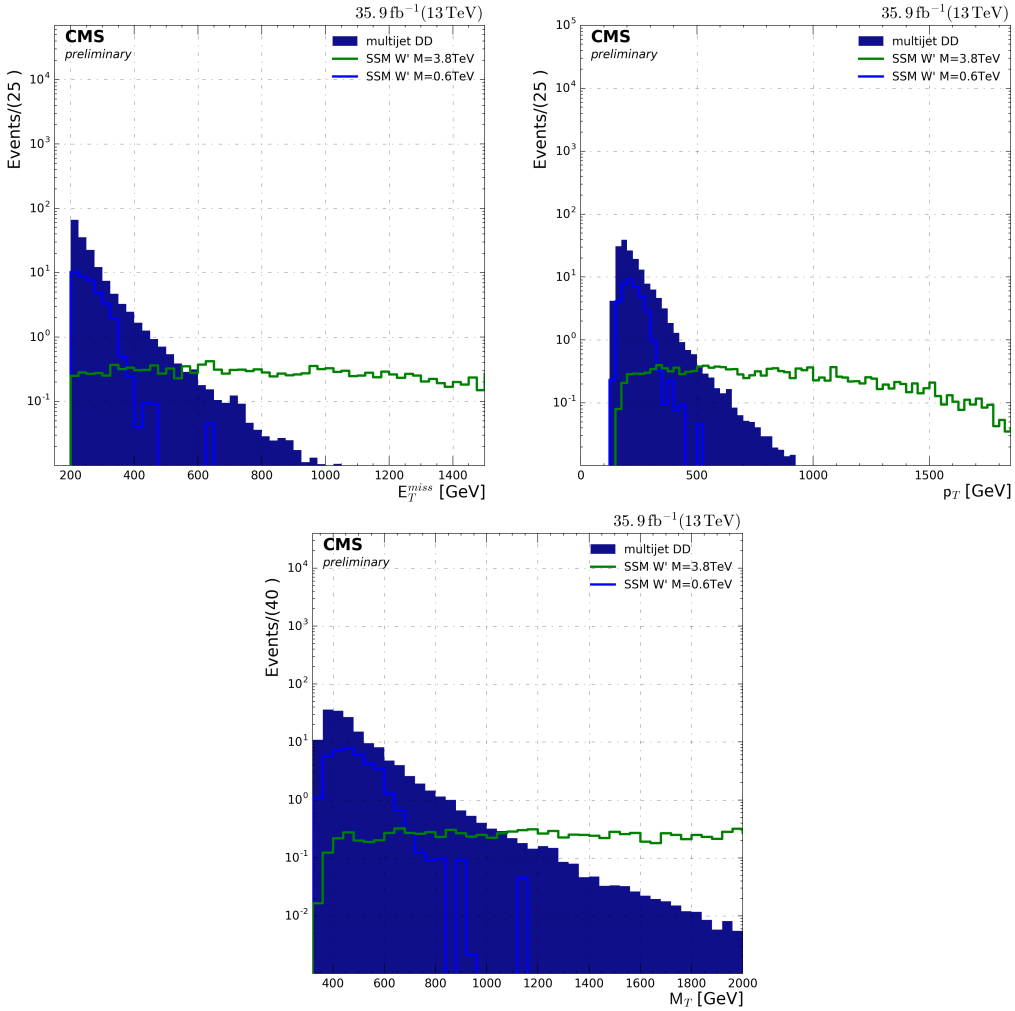

Figure 6.7: The multijet distributions derived from data can be seen from left to right as a function of the variables E_T^{miss},p_T and M_T after all selections being applied.

6.4 Pileup reweighting

Due to the high instantaneous luminosity at the interaction point of CMS, often more than one proton-proton interaction takes place at each bunch crossing. This leads to multiple interactions in any event, each giving rise to additional vertices. These additional interactions are part of what is called pileup. Also the underlying event has to be taken into account which originates from the proton. While strongly dependent on the beam conditions and thus run dependent, the average number of vertices in all of 2016 is ≈ 25.

Pileup conditions have to be considered in simulation due to effects on properties of the objects. The effects relevant for this analysis include possible differences in tau isolation

and missing transverse energy reconstruction. As a theoretical description of pileup events is very difficult, pileup is simulated using so-called minimum bias events. Minimum bias events are events that are not triggered by any specific condition but an expected bunch crossing. This means that all SM processes are taken into consideration at the same time and are dominated by QCD processes due to their large cross sections. While the beam conditions and thus the average number of pileup events change during data taking, simulation has to be continually adapted either by producing more events or by reweighting existing samples. The latter option is chosen and the MC based number of vertex distribution is continually adapted to the distribution found in data. For this, weights are derived on a bin-by-bin basis for all processes at the same time. The minimum bias cross section used for this procedure is 69.2 mb. However, the number of pileup events in data cannot be measured directly due to differences originating form misidentification. Instead it is calculated, using the instantaneous luminosity and the total inelastic proton-proton cross section, both of which can be measured directly. In Fig. 6.8 the distribution of the number of vertices is shown.

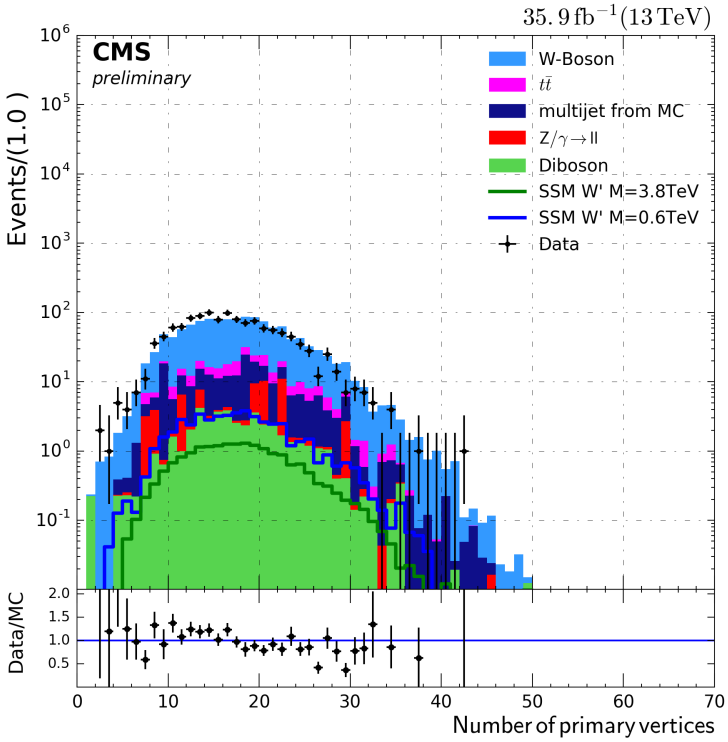

Figure 6.8: The distribution of the number of vertices.

6.5 Evaluation of Systematic Uncertainties

Virtually every measurement has some uncertainty accompanying it. In CMS there are two kinds of systematic uncertainties. One kind has an impact on a bin-by-bin basis with varying strength and thus might change the shape of any distribution. In contrast, the impact of the second kind of uncertainties has a constant value and only affects normalization. The second kind thus does not alter the shape of the distribution of events in a given variable. Examples for the second type of uncertainty are uncertainties on scale factors and the uncertainty on the luminosity. Examples for the first kind of uncertainty include the energy scale. To

evaluate this type of systematic uncertainty, the analysis is repeated with the investigated energy scale being varied to the minimally and maximally allowed values. The difference to the original distribution is then taken as the uncertainty. These uncertainties enter the figures as a gray band in which the uncertainties are added in quadrature. Considered in this analysis are:

- Luminosity uncertainty: Based on Ref. [73], an uncertainty of 2.5% is assumed for the background processes, changing the total number of events, independent of the bin. The signal efficiency is not affected by this uncertainty.

- Pileup reweighting uncertainty: Based on the recommendation by the Lumi Physics Object Group [98] a 4.6% uncertainty on the minimum bias cross section is assumed. Within these bounds the minimally and maximally allowed cross sections are chosen and the differences to the nominal minimum bias cross section are taken as uncertainty.

- PDF uncertainty: Following the recommendation of the PDF4LHC working group [99] the differences of PDF sets are used to evaluate the differences to the original distribution on a bin-by-bin basis for any given variable. These differences are used to determine an envelope of the individual uncertainties and this envelope is taken as the systematic uncertainty.

- Tau ID Scale Factor uncertainty: A dedicated study has found the tau ID scale factor to have a relative uncertainty of 5% plus 20% per TeV in tau-p_T by the tau POG [100].

- Tau trigger uncertainty: In Ref. [96] an uncertainty on the tau trigger scale factor of 10% has been determined. As this does not change with the tau p_T, this uncertainty scales the overall number of events.

- Tau Electron Fake uncertainty: Based on [100] an uncertainty on the electron faking a hadronically decaying tau smaller than 3% for both, barrel and endcap, has been applied.

- Tau Energy Scale uncertainty: The uncertainty on the energy scale was evaluated in [100] by comparing differences in data and simulation using jet and tau reconstruction algorithms. The uncertainty on the energy scale is estimated to be 1.2%.

- Jet Energy Scale uncertainty: The uncertainty on the jet energy scale has been found to vary depending on p_T and η. Exact values can be found in [101]. The energy of the jets, which are not identified as a tau, are shifted accordingly.

- Jet Energy Resolution uncertainty: The jet energy resolution depends on p_T and η [102] . The energy smearing is performed for each of the three momentum vector components individually. The smearing is randomly generated using the true value of the energy as the mean value of a Gaussian distribution.

- MET Energy Scale uncertainty: As the E_T^{miss} is reconstructed by many different objects, each object is shifted individually and the overall resulting difference is taken as the uncertainty. For the tau object, the tau POG recommends an uncertainty of 3% on the MET energy scale [100].

- k-Factor uncertainty: Based on [75] the maximum difference of the additive and multiplicative approaches, which is around 5%, is taken as the uncertainty on a bin-by-bin basis.

- multijet method uncertainty: Based on the study in 6.3.2 an uncertainty of 50% is assigned to the background yield estimated with the multi-jet ABCD method.

The relative uncertainties for all background processes are shown as a function of M_T in Fig. 6.9.

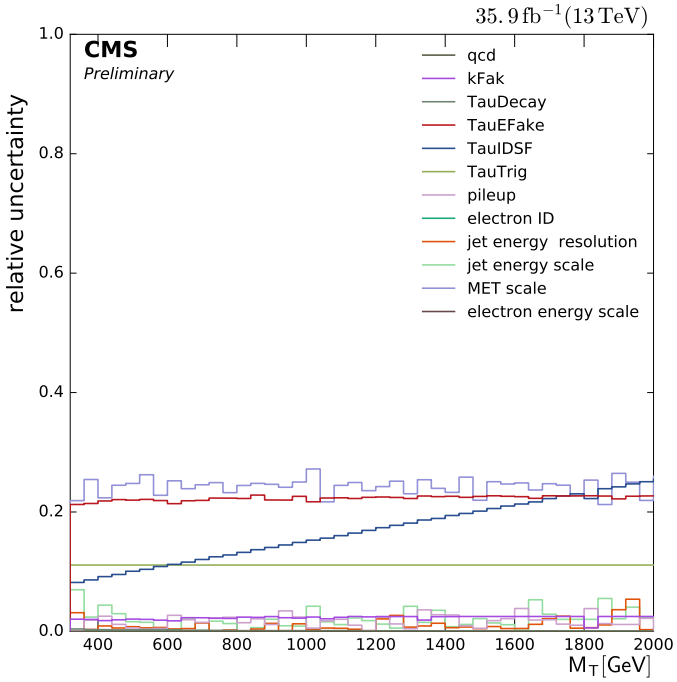

Figure 6.9: Relative uncertainties for all background processes are shown as a function of M_T.

In order to minimize the effects of bin-to-bin fluctuation originating from insufficient statistics of the background prediction in the final M_T distribution, the systematic uncertainties are fitted with a function of the form

$$\exp(a + bx + cx^2) \cdot x^d$$

where x is M_T/GeV and a,b,c and d are constants without any units.

6.6 Full Background Prediction and Final Distribution

With all parts of the analysis being explained, the full background prediction and CMS data alongside signal candidates will be shown. Most of the backgrounds are taken from simulation. As there are two possibilities to estimate the multijet background, Figs. 6.10, 6.11 and 6.12 will have both methods in top and bottom, respectively. The top row always features the multijet background derived from data and in the bottom row this background is taken from simulation.

In Fig. 6.10 the kinematic variables p_T/E_T^{miss} and $\Delta\Phi(\tau, E_T^{\text{miss}})$ are shown on the left and right, respectively. The trigger selection and tau identification are applied for both variables and the selection for $\Delta\Phi(\tau, E_T^{\text{miss}})$ is applied on the left, while the selection for p_T/E_T^{miss} is applied on the right For the $\Delta\Phi(\tau, E_T^{\text{miss}})$ distributions both methods to determine the multijet background yield good descriptions of the data over the complete range. In contrast,

for the p_T/E_T^{miss} distribution, the simulation based approach describes low values of p_T/E_T^{miss} well, while not describing the data at high values. For the data-driven approach the opposite is correct.

For the simulation based approach the bad description of high values of p_T/E_T^{miss} is expected due to lack of statistics in the samples used in the signal region. For the data-driven approach the statistics in the „loose“ signal region is much better and the description in the region of high values for p_T/E_T^{miss} is expected and found.

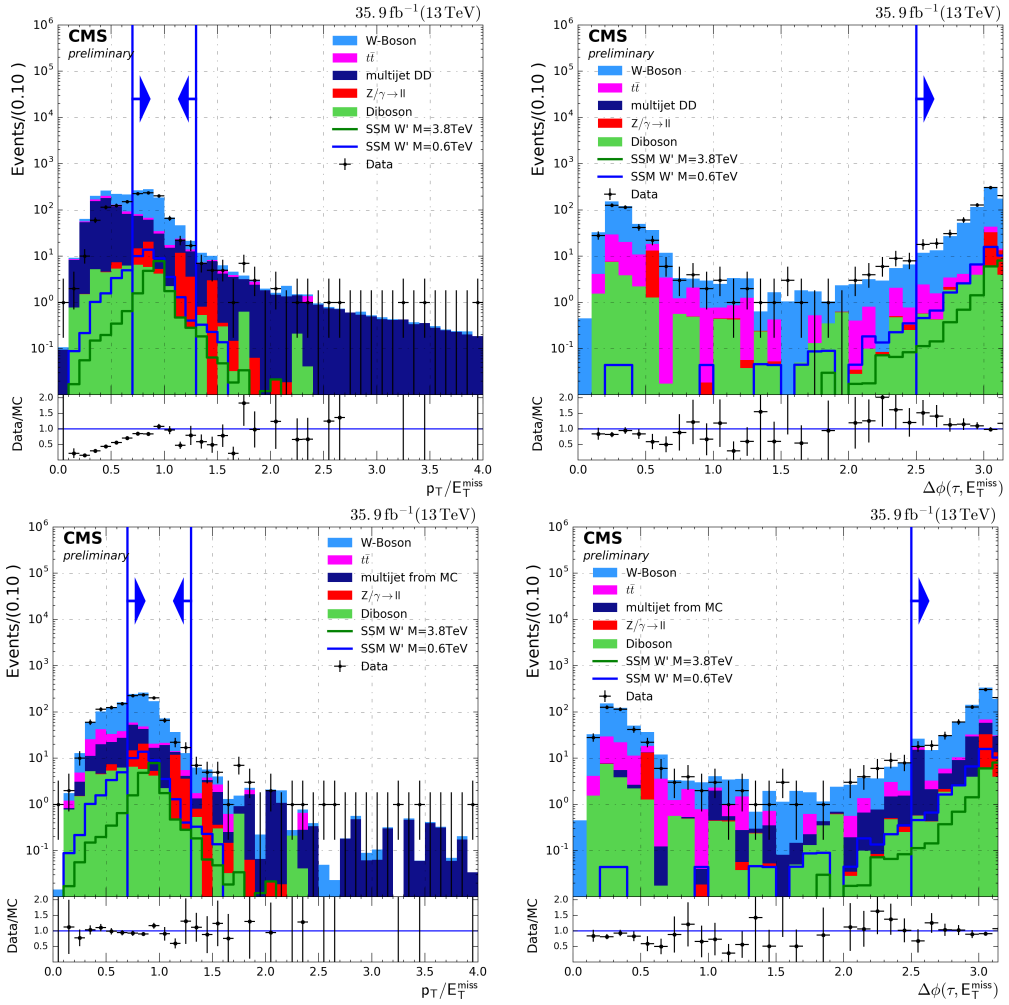

Figure 6.10: The distributions for the kinematic variables p_T/E_T^{miss} and $\Delta\Phi(\tau, E_T^{\text{miss}})$ are shown with all selections but the one on the variable itself. On the top row, the data-driven estimate of the multijet backgrounds is shown, while on the bottom row the simulation based backgrounds are shown. For the signal region indicated by the blue arrows, there are only minor differences.

In Fig. 6.11 the p_T and E_T^{miss} variables are shown individually on the left and right respectively. In this figure all selections are required and a good agreement between data and background prediction can be found for both approaches on top and bottom, respectively.

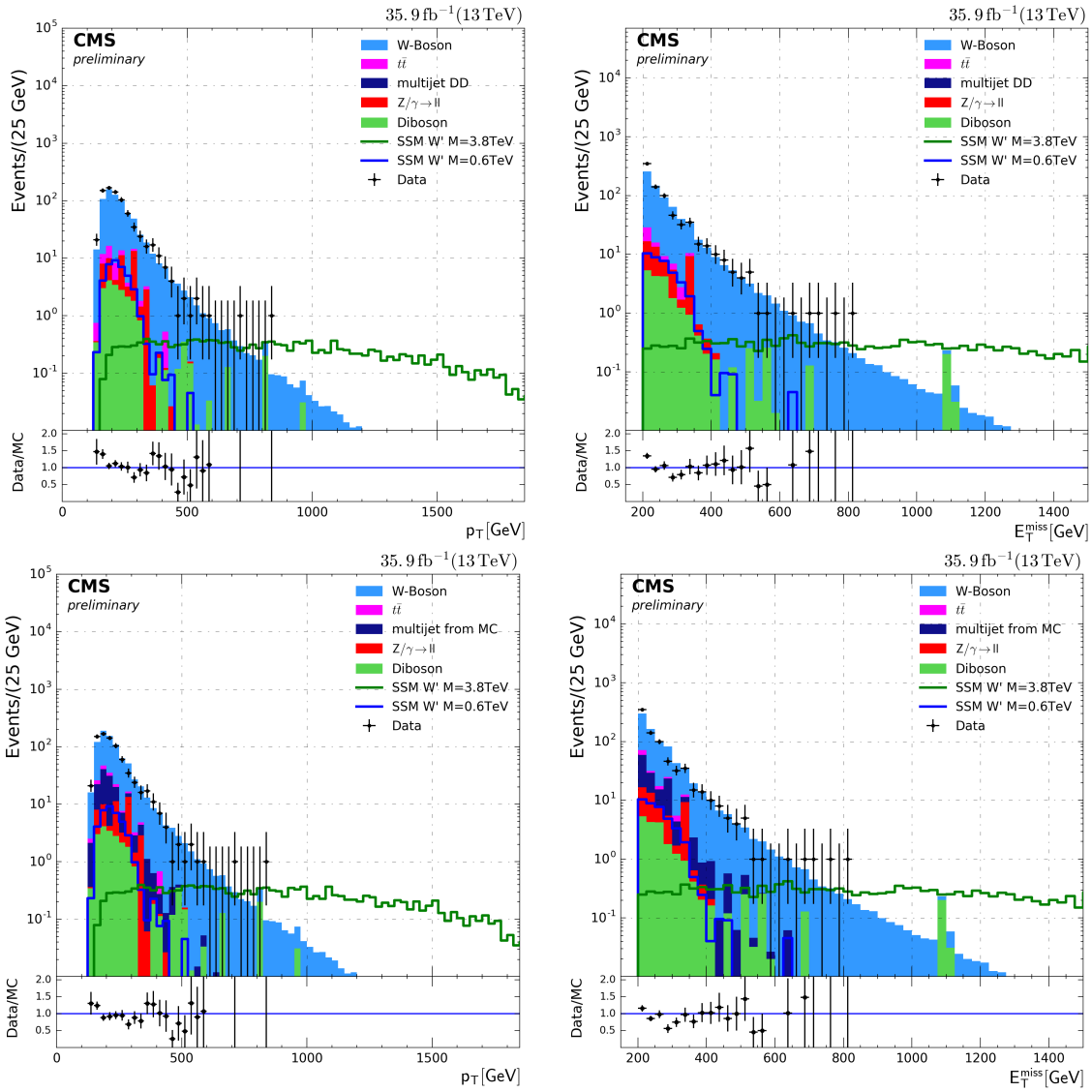

Figure 6.11: The distributions for the variables p_T and E_T^{miss} are shown.

The final distribution in Fig. 6.12 shows the number of events as a function of the transverse mass. On left and right the non-cumulative and cumulative distributions are given. On top and bottom, again, the data-driven and simulation based approaches are shown, respectively. These serve as an input for the limit setting procedure. The data is found to be described well within the systematic uncertainties.

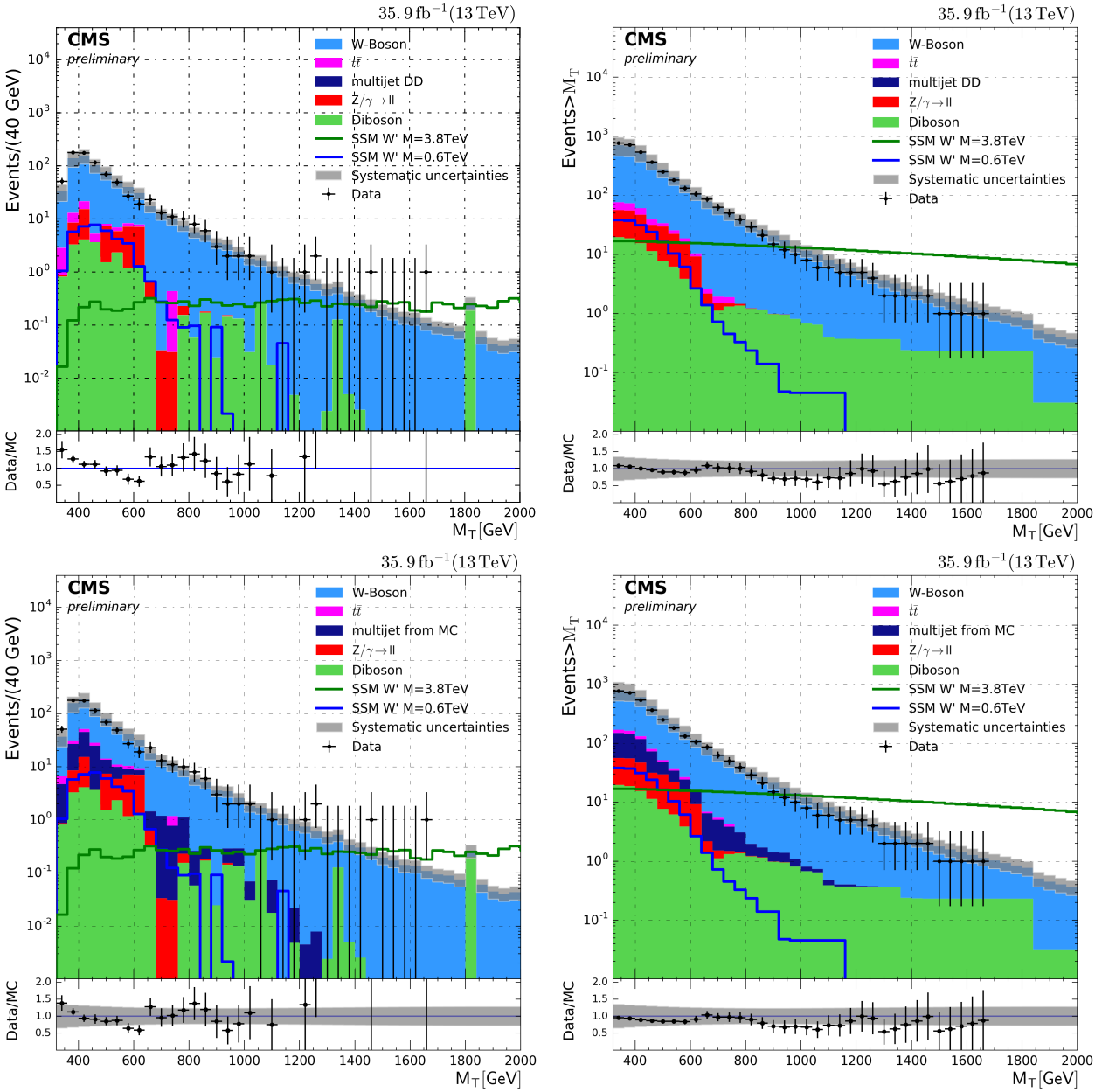

Figure 6.12: The distribution for the discriminating variable, M_T, is shown on the left in a non-cumulative and on the right in a cumulative way. The data is described well by the Monte Carlo and multijet estimate derived from data.

6.6.1 Final Distributions for Electron and Muon

In order to get a complete picture for the tau lepton, in this thesis not only the hadronically decaying taus but also the leptonically decaying taus are considered. A leptonically decaying tau is virtually not distinguishable from an electron or a muon originating directly from a W' – or any other particle for that matter. As a direct consequence, the electron or muon has to identified. In CMS this is done in a dedicated search for a W' decaying into an electron or muon and the corresponding neutrino. The analysts have agreed to provide the final distribution with the signal expectation of the $W' \to \tau\nu_\tau$ where the tau lepton further decays to an electron or muon. The details of the analysis are documented in [103, 104].

In Fig. 6.13 the final distributions for the electron or muon and missing transverse energy channel are shown on left and right, respectively. The final distribution agrees within the assigned systematic uncertainties.

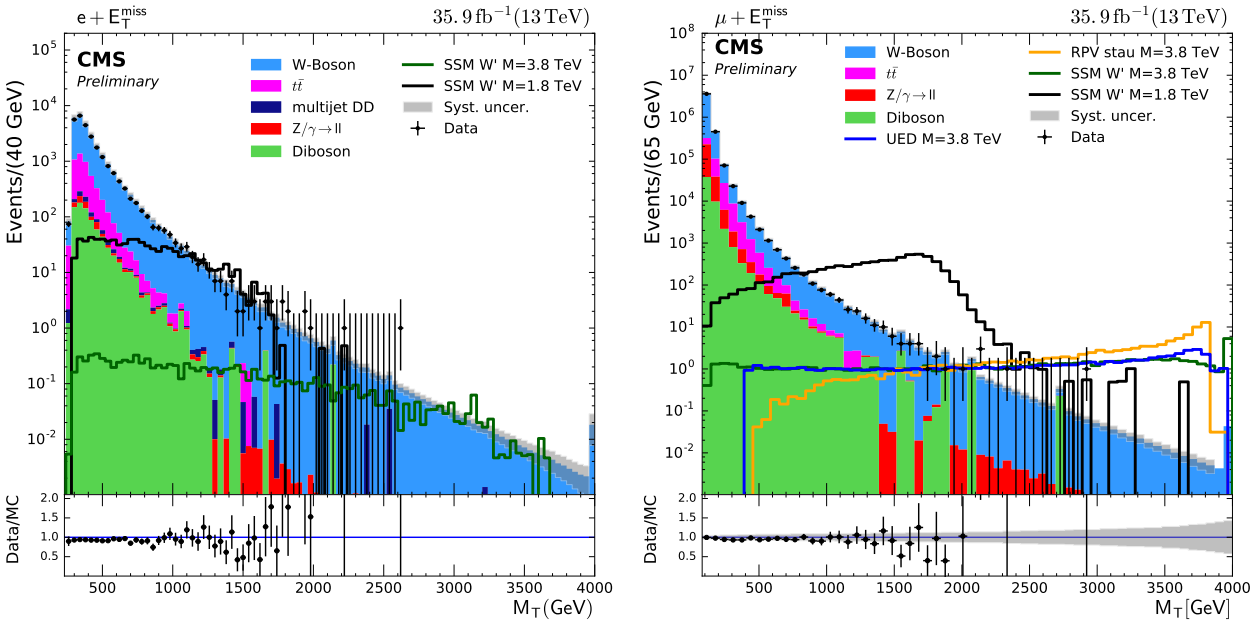

Figure 6.13: The final distribution for the electron or muon and missing transverse energy channels are shown on the left and right, respectively. These distributions have been produced by the authors of Ref. [104]. In the distribution for the electron and E_T^{miss} final state, the displayed signal displays a W' decaying to a tau which further decays to an electron, ignoring the neutrinos. In contrast, in the distribution of the muon and E_T^{miss} final state, the displayed W' directly decays into muons. In the statistical analysis the W' will first decay into a tau and then into a muon.

Chapter 7

Interpretation

In Sec. 6.6 no significant deviation from the SM expectation has been observed. In the following exclusion limits are determined on the model predictions. These exclusion limits are a measure for the compatibility of a given signal model with the data taken. First, the method to determine the exclusion will be introduced, then the different model interpretations are discussed.
Unless stated otherwise, the multijet background is determined with the data-driven approach.

7.1 Computation of Limits

For the W' specific models a multi-bin approach is used in order to derive an exclusion limit from the M_T distribution, as shown in Fig. 6.12 for the hadronic decays and Fig. 6.13 for the leptonic decays. The kinematic selections on $\Delta\Phi(\tau, \mathrm{E_T^{miss}})$ and $\mathrm{p}_T/E_T^{\mathrm{miss}}$are already applied to the M_T distribution. The M_T distribution is divided into multiple bins, for each of which a likelihood function is separately evaluated. The multi-bin approach takes the information of the shape of the signal into account and is often more sensitive to a given signal or at least as sensitive as a single-bin approach. Additionally, the multi-bin approach is typically more stable than the single-bin approach as it uses more information. The likelihood function can be modeled in two ways, using the so called frequentist or Bayesian approach. In the past the W' groups of the CMS and ATLAS experiments have agreed upon using the Bayesian approach, which is reviewed in detail in [30], for the derivation of exclusion limits. As the name suggests, Bayes' theorem is used. In Bayes' theorem two subsets A and B of the set S are connected to each other. Bayes' theorem states that the probability of B being true assuming A is true can be connected to the probability of A being true assuming B is true by the formula:

$$P(A|B) = \frac{P(B|A)P(A)}{P(B)}$$

where A is a hypothesis and B the set of data. One can thus connect the probability of a hypothesis H being true for a given set of data ($P(H|\text{data})$) to the probability of the data occurring assuming the hypothesis to be true (($P(\text{data}|H)$)). According to Bayes' theorem the probability to observe a given set of data and the prior believe in the hypothesis $\pi(H)$ also have to be taken into account. Due to the denial of any knowledge about the parameter of interest, the prior is assumed to be flat for positive values of the parameter of interest. This choice is based on Laplace's rule [105] The prior believe in the hypothesis can be influenced by the systematic uncertainties. These systematic uncertainties are assumed

to follow the log-normal distribution. The probability to observe a given set of data can be calculated by $P(B) = \sum_i P(B|A_i)P(A_i)$ which translates to the probability of all possible hypotheses ($P(\text{data}|H_i)$) times the probability of the particular hypothesis $\pi(H_i)$ as A_i is a given hypothesis and B is the set of data.

If the model hypothesis depends on a set of parameters θ, it is common practice in BSM physics to provide a limit for these model parameters. For the SSM W' the most prominent model parameter is the mass of the W'. Furthermore, in particle physics it has been agreed upon excluding the parameter with a 95% probability. This is also known as the 95% confidence level (C.L.), even though this terminology is originally used by the frequentist interpretation. The 95% C.L. is calculated using the following formulae:

$$0.95 = \frac{\int_0^{\theta_{0.95}} \mathrm{d}\theta\ \pi(\theta) \cdot \mathrm{L}'(\text{data}|\theta)}{\int \mathrm{d}\theta'\ \pi(\theta') \cdot \mathrm{L}'(\text{data}|\theta')}$$

with

$$\mathrm{L}'(\text{data}|\theta) = \int \mathrm{d}\vec{\nu}\ \mathrm{L}_{\text{Poisson}}(\text{data}|\theta, \vec{\nu})$$

and

$$\mathrm{L}_{\text{Poisson}}(\text{data}|\theta, \vec{\nu}) = \prod_{i \in \text{bins} \otimes \text{channels}} \frac{\epsilon_i(\theta, \vec{\nu})^{n_i}}{n_i!} e^{-\epsilon_i(\theta, \vec{\nu})} \times \pi(\vec{\nu}),$$

where $\theta_{0.95}$ is the limit on the model parameter, θ the parameter of interest, $\vec{\nu}$ are the nuisance parameters – these are the parameters modeling the uncertainties –, n_i is the number of events in a given bin i and $\epsilon_i(\theta, \nu)$ is the expectation value of the number of events. These numbers of events can be translated into the cross section for a give integrated luminosity.

The described procedure is implemented in the „Higgs combine tool“ [106, 107] which builds upon the RooStats package [108]. A detailed description of the statistical analysis can be found in [48]. In the context of this thesis a model-independent single-bin limit is derived. In this approach one single bin is formed, starting at a given $\mathrm{M}_T^{\text{min}}$ threshold up to infinity and the excluded cross section is calculated. The advantage of this approach is the usability for a reinterpretation in the context of theories with comparable kinematics as applied in this thesis.

7.2 Parameters of Interest

In this thesis almost all exclusion limits are calculated on the cross section σ times the branching ratio B of the process. To directly derive the limits on the cross section, the Higgs combine tool needs the integrated luminosity times the signal acceptance times efficiency, $\mathcal{L} \times A$, as an input for a given point of the parameter of interest phase space. The signal efficiency for the hadronically decaying taus is shown in Fig. 7.1. It peaks around $M_{W'} \approx 3000\,\text{GeV}$ with a value of 32% and features the W'-typical „banana“ shape. This shape can be explained by two effects. The first effect affects the low masses of the W' where the tau lepton often does not fulfill the trigger requirements, resulting in low values for the acceptance times efficiency. For medium masses of the W' the efficiency increases until roughly 2500 GeV at which it plateaus. For masses above approximately 4000 GeV the values for the acceptance times efficiency start to decrease again as a consequence of the second effect. This is caused by the contribution of the low W' mass off-shell production increasing with the mass of the W' and the first effect reducing the over all acceptance times efficiency.

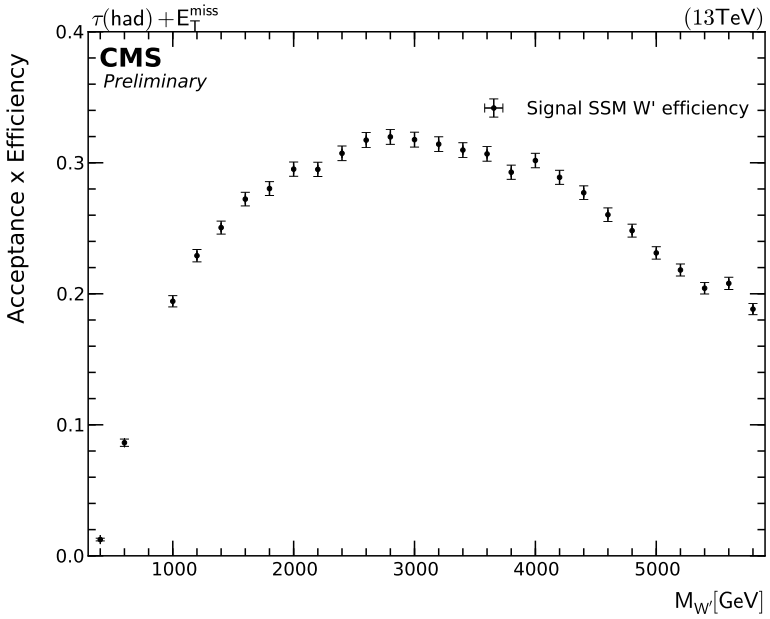

Figure 7.1: The signal acceptance times efficiency for the hadronic tau decays of the SSM W'.

For the W' specific models, the parameters of interest are the mass $M_{W'}$ or the coupling parameter $\frac{g_{W'}}{g_W}$ for the SSM and the mixing angle $\cot\theta_E$ for the NUGIM. For the model-independent approach the cross section is evaluated as a function of $\mathrm{M}_T^{\mathrm{min}}$. The signal efficiency is fixed to the signal efficiency of the mass point $M_{W'}$=3.0 TeV at $A \times \epsilon \approx 0.32$.

7.3 Exclusion Limits on the Sequential Standard Model

Upper limits on the cross section times branching ratio of the W' to $\tau\nu$ are evaluated for the SSM as a function of M_T. This is shown for the hadronically decaying taus in Fig. 7.2. The observed limit is depicted as the black solid line, while the black dotted line is the expected limit. The 1 and 2 σ standard deviations on the expected limits are displayed as the green and yellow bands respectively. The thin dashed line with the grey band corresponds to the theoretical cross section times branching ratio of the SSM W' at NNLO and the uncertainty due to its PDF. The intersection of the observed limit and the theoretical cross section mark the highest possible exclusion limit on the mass. For the hadronically decaying taus this is $M_{W'}$=4.2 TeV. The observed limit follows the expected limit closely until roughly 3 TeV in W'. After that point the slight deficit in data results in better observed exclusion limits than expected. In Fig. 7.3 limits for the leptonically decaying taus are shown. The exclusion limits have been determined to be $M_{W'}$=3.2 TeV and $M_{W'}$=2.1 TeV for the decay to electron and muon respectively. For both cases the observed limit is largely contained within the 1 standard deviation band. In Fig. 7.4 the combination of all tau decays are shown. The combination of all three channels is dominated by the hadronically decaying taus following the much better exclusion limit. The exclusion limit is found to be $M_{W'}$=4.3 TeV which is an improvement of 0.1 TeV.

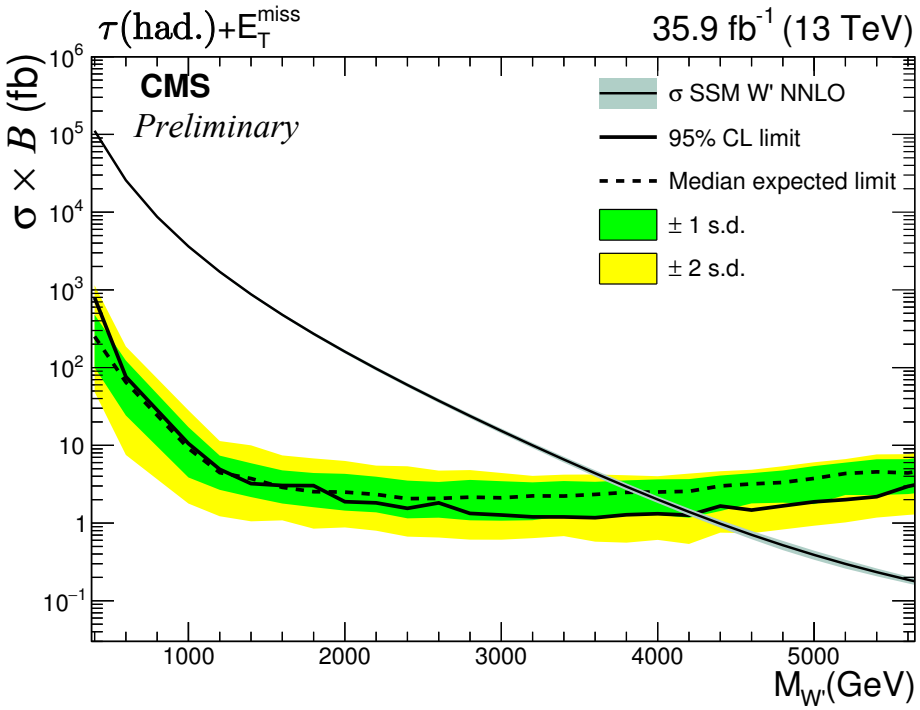

Figure 7.2: The exclusion limit on the cross section times branching ratio is shown as a function of the mass of the W' for the hadronic decay channel. The black solid line is the observed limit in Run II. The green and yellow areas around the short-dashed black line are the 1 and 2 standard deviation bands around the expected limit.

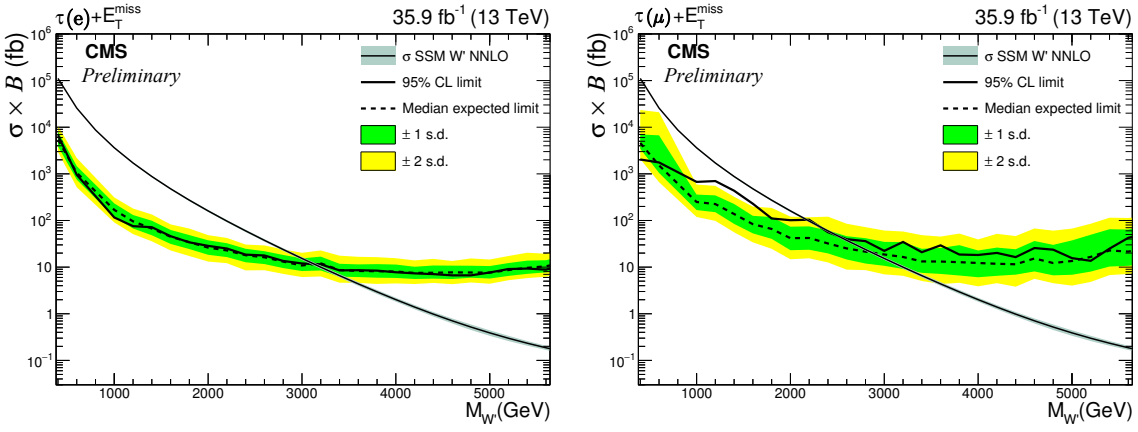

Figure 7.3: The exclusion limits on the cross section times branching ratio are shown as a function of the mass of the W' for the electron (left) and muon (right) decay channels. The black solid line is the observed limit in Run II. The green and yellow areas around the short-dashed black line are the 1 and 2 standard deviation bands around the expected limit.

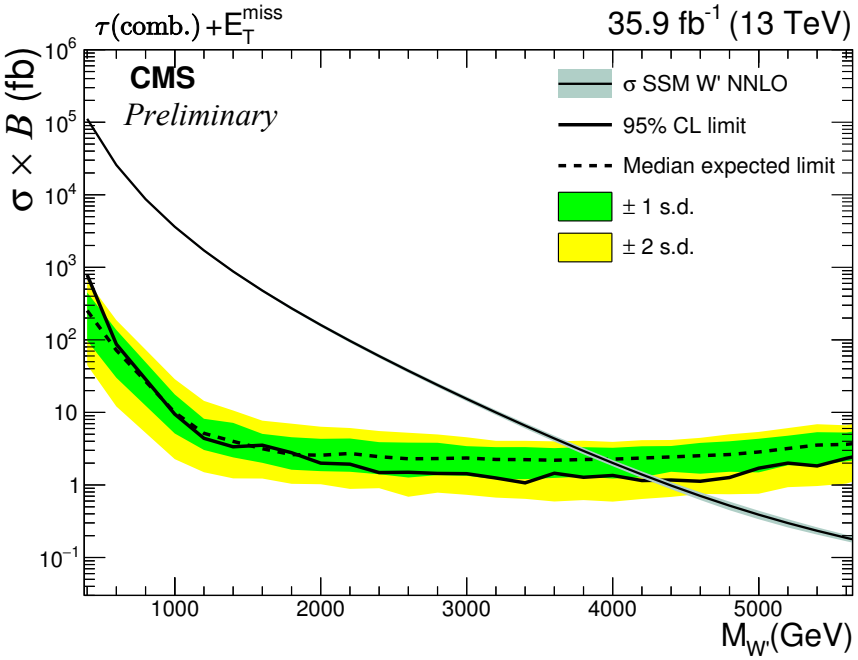

Figure 7.4: The exclusion limit on the cross section times branching ratio is shown as a function of the mass of the W' for combination of all decay channels. The black solid line is the observed limit in Run II. The green and yellow areas around the short-dashed black line are the 1 and 2 standard deviation bands around the expected limit.

7.3.1 Impact of the Decay Mode and Isolation on the Expected Limit

In section 4.2.3 the modifications of the identification method for high-p_T taus have been described and an increase in reconstruction efficiency has been reported. In Fig. 7.5 the effect on the expected limit is shown for the medium isolation working point of the discriminator. The old version of the decayModeFinder, which does not include the 2 prong decay modes, is displayed with the dashed line, while the new version is shown with the solid line. One can see that for masses of the W' up to 1 TeV no significant differences can be observed, while for masses larger than 1 TeV the new decayModeFinder yields better cross section limits. The exclusion limit differs by roughly 100 GeV in $M_{W'}$in favor of the new version.

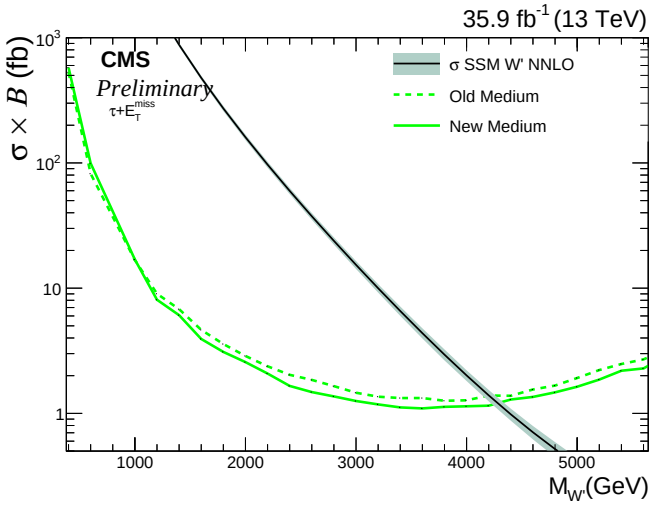

Figure 7.5: The expected exclusion limits of the new and old decayModeFinder based exclusively on a Monte Carlo based description of the background are compared for the medium isolation working point. The new decayModeFinder yields a lower cross section limit for large masses of the W', while for low masses both discriminators perform equally well.

As there are not only two versions of the discriminator, but also different isolation working points, one can test the impact of the isolation on the expected limit. In order to save computing resources, this is done purely on simulation. On left and right of Fig. 7.6, the expected limits for the different isolation working points, ranging from „very loose“ to „very tight“, are displayed for the new and old versions of the decayModeFinder, respectively. Two things can be observed: The behavior of each isolation working point is identical for both versions and the dependency of the isolation working point yielding the best cross section limit on $M_{W'}$. One finds for large values of $M_{W'}$ that the looser the isolation, the better the cross section limit. This can be explained by the fact, that a more loose working point corresponds to a higher signal efficiency. The higher $M_{W'}$ corresponds to more events expected at large values of M_T where there is only little background. In contrast, the tighter the working point the more events from both, signal and background, are rejected. Since the low M_T region is dominated by background, the additional background suppression results in better cross section limits. A direct comparison of all working points of both versions is shown in Fig. 7.7 where the region of $M_{W'}$ between 4 and 4.8 TeV. is shown.

If strictly the exclusion limit on the SSM is supposed to be improved, the very loose working point is recommended to be used. However, if one also is interested in the lower region of W' masses, for example in the context of NUGIM or the impact of the coupling

strength, a working point that works well at all masses should be chosen. This corresponds to the medium working point used throughout this analysis.

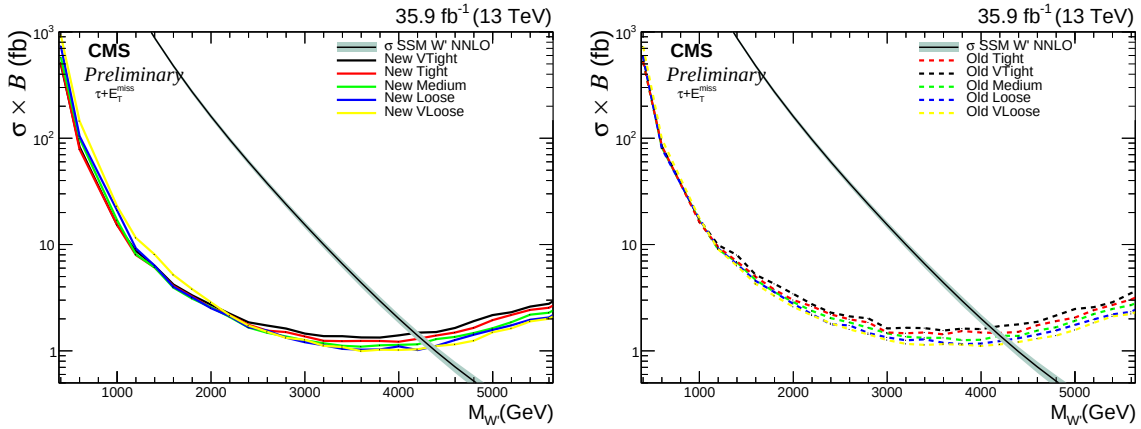

Figure 7.6: The expected exclusion limits of different isolation working points based exclusively on a Monte Carlo based description of the background are compared for the the new and old decayModeFinder on the left and right respectively. Both on the left and right, the looser isolation working point is the better is the exclusion limit at high masses, while for low masses the trend is inverted.

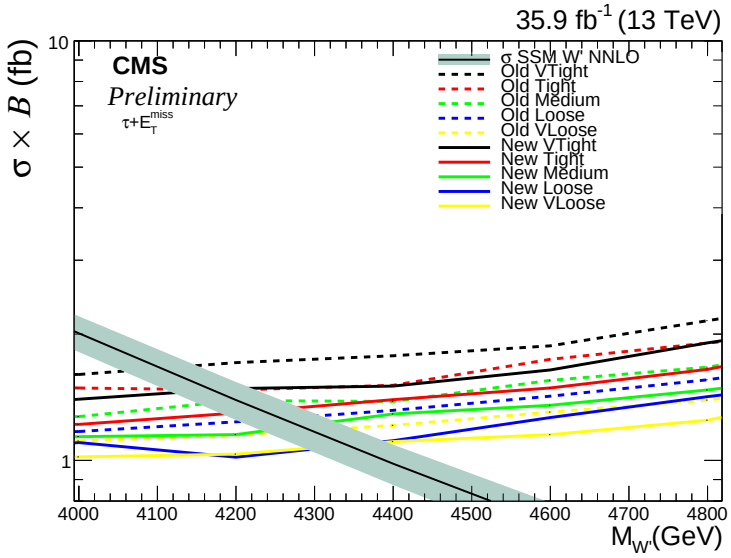

Figure 7.7: A comparison of all expected limits for the isolation working points is shown. For a given isolation working point the new decayModeFinder is performing better than the old decayModeFinder version.

7.3.2 Impact of Multijet Background Estimation

With both a simulation and a data-driven based estimate available, one can compare exclusion limits of both methods and test for an improvement. This is shown in Fig. 7.8. On the left the multijet background is estimated using data and on the right it is estimated using simulation. It can be seen that the observed limits for both approaches are nearly identical.

The small differences are due to statistical fluctuations originating from the numerical determination of the exclusion limits. For the expected exclusion limits there are small differences to be found. The one and two standard deviation bands are slightly bigger and the expected median limit is generally insignificantly lower for the data-driven approach compared to the simulation based approach. As the maximum excluded mass of the W' is virtually the same for both methods and the cross section limits are not significantly improved, one might consider using simulation based multijet description in favor of the data-driven approach in the future.

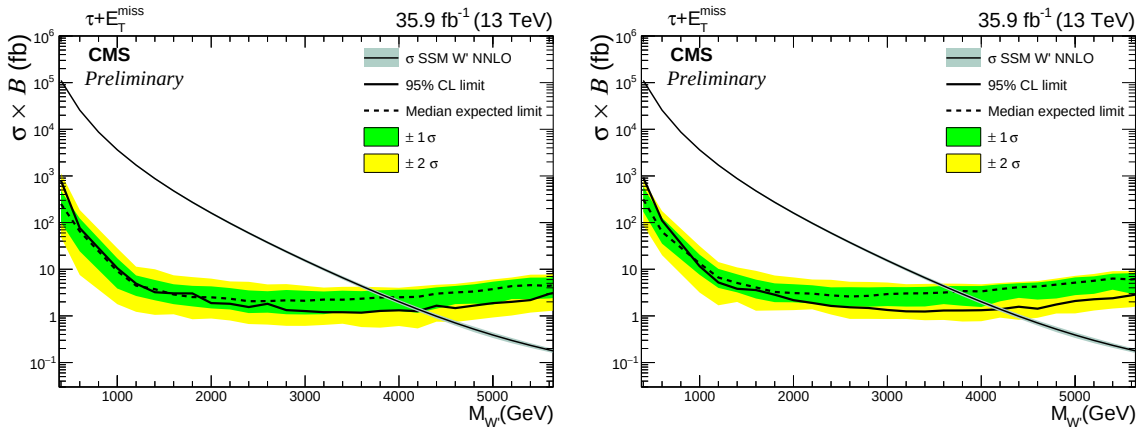

Figure 7.8: On the left and right, the expected and observed exclusion limits for the data-driven and simulation based descriptions of the multijet background are shown. For both the exclusion limit is 4.1 TeV. Only minor differences can be found.

7.3.3 Projection to $300\,\mathrm{fb}^{-1}$

At the end of Run 2, data corresponding to an integrated luminosity of roughly $300\,\mathrm{fb}^{-1}$ are expected to be taken. In order to estimate the increase in sensitivity the hadronic tau channel is used with the SSM as a benchmark model. The background and signal expectations are scaled to the integrated luminosity of $300\,\mathrm{fb}^{-1}$ and the limit setting procedure is repeated. The relative size of the systematic uncertainties is kept the same. As the systematic uncertainties are expected to decrease, the projection serves as a very conservative scenario. The obtained expected exclusion limit is shown in Fig. 7.9 and the sensitivity in $M_{W'}$ is found to increase to 5.2 TeV. The increase of 1 TeV is comparable to the increase of approximately 1.2 TeV from the data taken in 2015 compared to data taken in 2016.

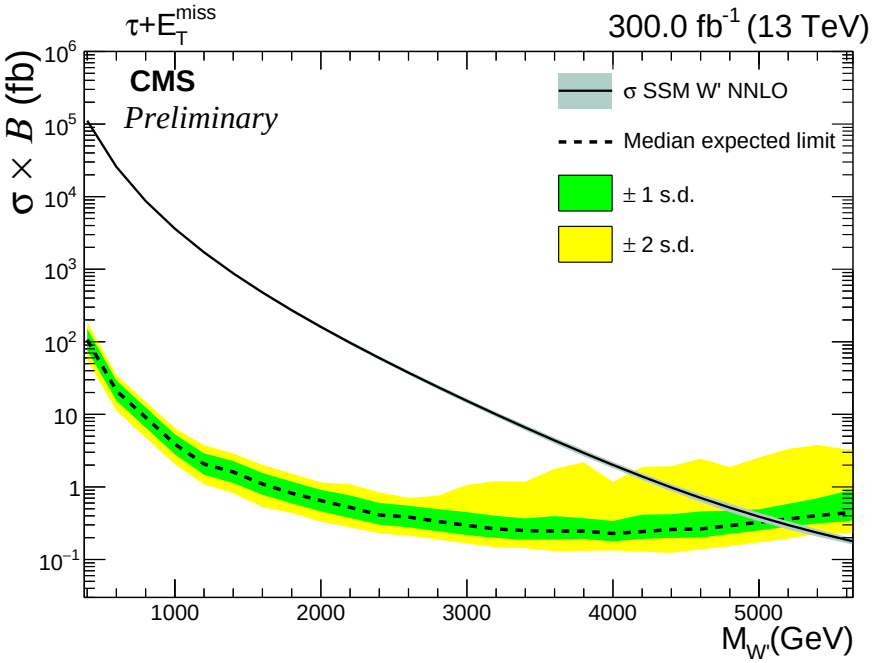

Figure 7.9: The projected exclusion limit on the cross section times branching ratio is shown as a function of the mass of the W' for the hadronic decay channel. The green and yellow areas around the short-dashed black line are the 1 and 2 standard deviation bands around the expected limit.

7.4 Impact of Coupling Strength

As the width of the W' is connected to the coupling strength via

$$\Gamma_{W'} = m_{W'} \frac{g_{W'}}{4 \cdot \pi}$$

the shape of the W' is sensitive to the coupling strength. This can be inferred from Fig. 3.5. This sensitivity is probed by deriving limits on samples obtained by reweighting by CMS officially produced samples with privately produced samples for different widths of the W'. The reweighting is performed by evaluating weights on a bin-by-bin basis in the M_T variable for a given mass point using MADGRAPH 5 version 1.5.11. The weights are defined as the fraction of number of events in a given bin, for two different coupling strengths, where one of those is required to be 1.

The exclusion limits are derived with respect to the ratio of the coupling strengths, in contrast to the $M_{W'}$ dependency in the $g_{W'} = g_W$ case. This limit is calculated for every W' mass. In Fig. 7.10 the limit is shown exemplary for $M_{W'}$=4.2 TeV, the largest excluded mass in the SSM. The observed limit intersects the blue solid line indicating the theoretical cross section for the W' at approximately $\frac{g_{W'}}{g_W}$=0.8. The expected intersection point is at $\frac{g_{W'}}{g_W}$=1. This slight deviation can be explained by deviations in the input distribution.

A second degree polynomial then is used as an interpolation of the expected and observed limits to calculate the intersection points of the theoretical cross section. Once the intersection points for all W' masses are determined, they are connected as seen in Fig. 7.11. The minimal value for the observed exclusion of $\frac{g_{W'}}{g_W}$ ranges from 0.2 at low masses to 1.5 at high masses.

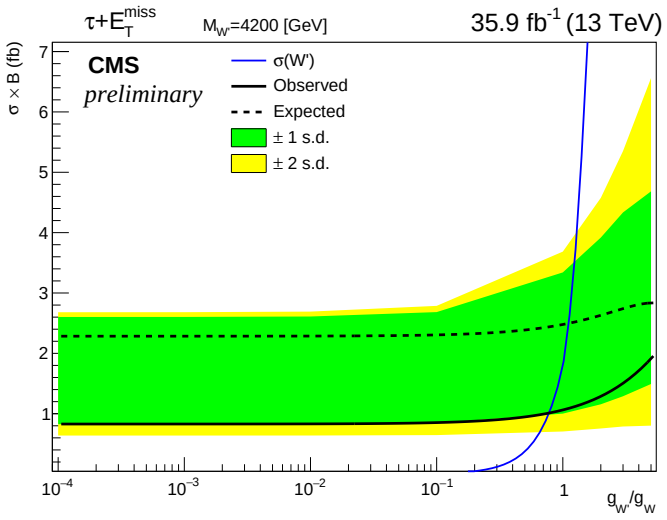

Figure 7.10: The cross section limit is shown as a function of the ratio of coupling strengths of the W' to the SM W boson. The intersection point of the blue theory cross section curve with the observed and expected limit is used as an input for a 2-dimensional plot later.

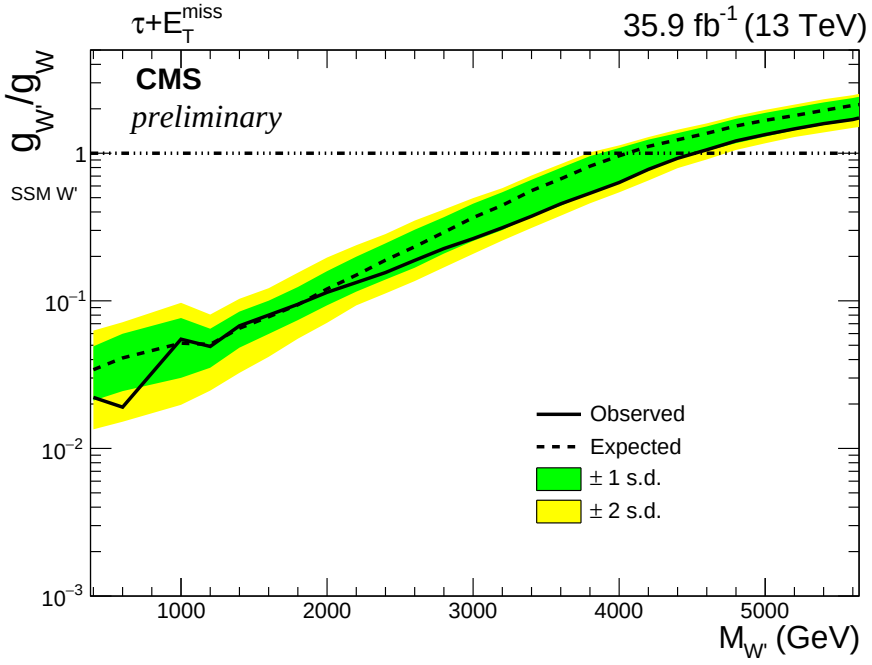

Figure 7.11: The exlusion limit on the ratio of coupling strengths of the W' to the SM W boson is shown as a function of the mass of the W'. Everything to the upper left of the black solid line, indicating the observed limit, can be excluded.

7.5 NUGIM

The parameter defining the NUGIM $\cot\theta_E$ is connected to the fraction of width of a W' with free coupling strength and a SSM W' via

$$\frac{\Gamma_{W'}}{\Gamma_{W'}^{SSM}} = \frac{4 + \frac{1}{4}\cot^2\theta_E + 8\tan^2\theta_E}{12 + \frac{1}{4}}.$$

As the fraction of the width in turn is connected to the fraction of coupling strengths $\frac{g_{W'}}{g_W}$, a limit on $\cot\theta_E$ can be derived by reinterpreting the limit obtained in 7.4. This is done using the formula given above and visualized in Fig. 7.12 on the left. This formula has no natural boundary for the ratio of the mass and the width of the W'. Assuming a particle hypothesis, the relative width $\frac{\Gamma_{W'}}{m_{W'}}$ is required to be larger than 50%. With the calculation used for Fig. 3.6, this requirement restricts $\cot\theta_E$ as a function of the mass of the W'. This dependency is shown in Fig. 7.12 on the right. For $M_{W'}$>3000 GeV the threshold value is constant at $\cot\Theta_E$=6.8. In Fig. 7.13 the limit is shown. The gray area above $\cot\theta_E$ indicates the region in which the W' width is larger than 50% and a particle hypothesis is increasingly unlikely. While the limit can go up to $\cot\theta_E \approx 9$ for low masses, the largest W' mass for which the width is smaller than or equal to 50% of $M_{W'}$ is 2.3 TeV. The limit has improved with respect to the limit of $M_{W'}$=2 TeV obtained with 8 TeV data at lower values of $\cot\theta_E$, shown as the blue dotted line. At the same value for $\cot\theta_E$ the excluded mass is 2.7 TeV an increase of 700 GeV.

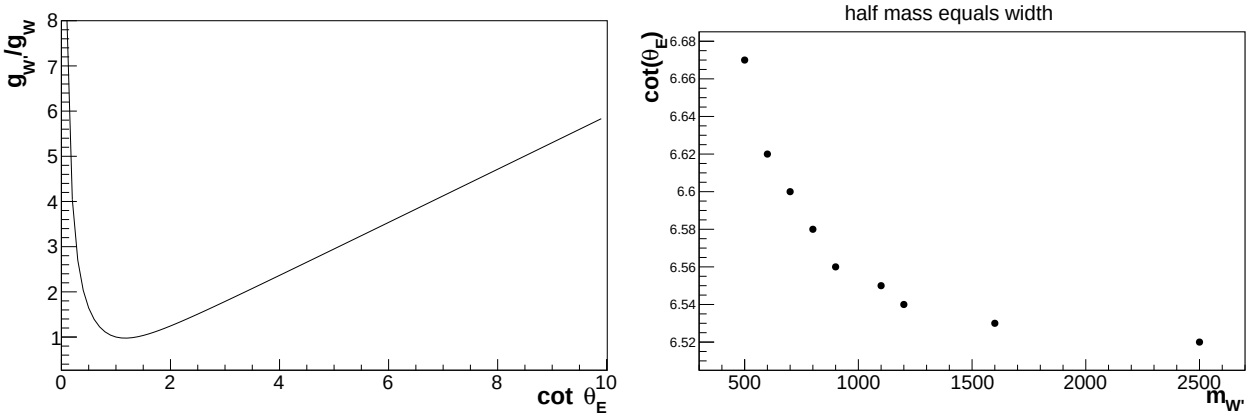

Figure 7.12: On the left the dependence of the fraction of the coupling strengths to the NUGIM parameter $\cot\Theta_E$ is shown, while on the right the dependency of the value of the NUGIM parameter, at which the width equals half of the W' mass, relative to its mass to $M_{W'}$ is shown.

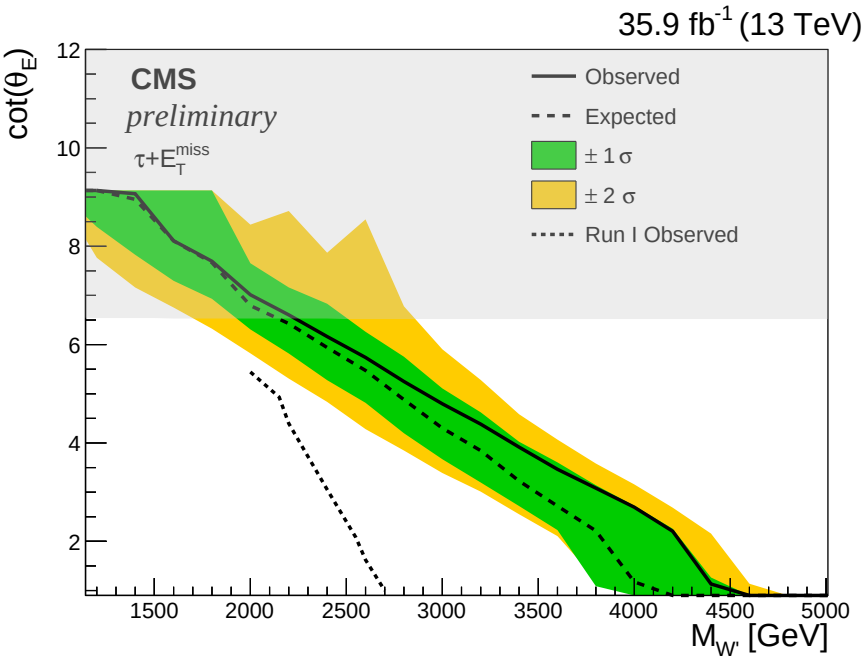

Figure 7.13: The exclusion limit on the NUGIM parameter $\cot\Theta_E$ is shown as a function of the mass of the W'. The gray area indicates the region in which the relative width of the new boson is larger than 50% and a particle hypothesis is unlikely. The black short-dashed line is the exclusion limit observed with Run I data, while the black solid line is the observed limit in Run II. The green and yellow areas around the short-dashed black line are the 1 and 2 σ bands around the expected limit.

7.6 Model Independent Limit

In addition to the model dependent exclusion limit, a model independent limit has been derived. In contrast to the multi-bin approach for the model-dependent search, a single-bin approach is used. A scan over different M_T^{min} thresholds is performed to gauge the change in the excluded cross section. This can be seen in Fig. 7.14. A limit on the cross section times branching ratio ($\sigma \times B$) times acceptance and efficiency ($A \times \epsilon$) can be set. The values for $\sigma \times B \times A \times \epsilon$ range from 174 fb at M_T^{min}=300 GeV to 0.58 fb at M_T^{min}=2000 GeV.

The main advantage of this type of limit is the possibility for theorists to reinterpret this limit easily with a given model. This model has to have similar kinematics in order to be considered. If the kinematics differ strongly, it is strongly suggested to evaluate the exclusion limit for the model. As the reconstruction efficiencies are already included in the exclusion limit, the theorist has to determine the efficiency of the chosen signal above the M_T^{min} threshold: $\epsilon_{\text{signal}} = N_{M_T > M_T^{min}}/N_{\text{total}}$.

Any given, new model then can be excluded if the cross section above the threshold is higher than the excluded cross section given in Tab. 7.1. The condition $\sigma_{\text{newmodel}}(N_{M_T > M_T^{min}}/N_{\text{total}}) = \sigma_{\text{total}} \cdot \epsilon_{\text{signal}} > \sigma_{\text{excluded}}$ thus has to be fulfilled.

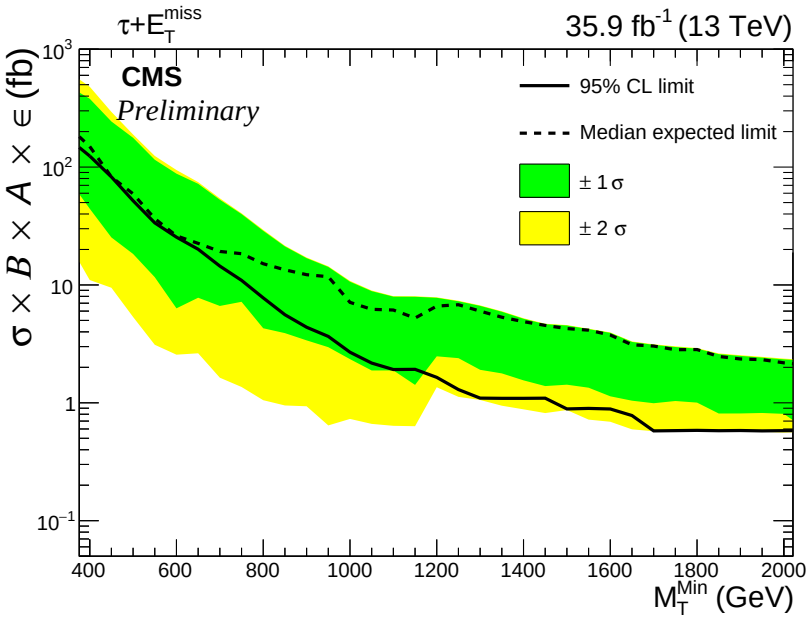

Figure 7.14: The exclusion limit on the cross section times branching ratio times acceptance and efficiency ($\sigma \times \mathcal{B} \times A \times \epsilon$) is shown as a function of the minimal threshold value for the transeverse mass (M_T^{min}). The black solid line is the observed limit in Run II. The green and yellow areas around the short-dashed black line are the 1 and 2 σ bands around the expected limit.

Table 7.1: Values of the observed and expected excluded cross sections for given M_T^{min} values.

M_T^{min} [TeV]	0.3	0.4	0.5	0.6	0.7	0.8
Observed limit [fb]	174.74	180.18	171.69	77.50	32.71	19.90
Expected limit [fb]	209^{+270}_{-124}	130^{+200}_{-90}	50^{+110}_{-40}	31^{+61}_{-22}	23^{+30}_{-16}	20^{+10}_{-15}
M_T^{min} [TeV]	0.9	1.0	1.1	1.2	1.3	1.4
Observed limit [fb]	10.65	5.54	3.63	2.18	1.92	1.27
Expected limit [fb]	12^{+5}_{-10}	$8.7^{+2.0}_{-5.9}$	$7.2^{+0.8}_{-5.3}$	$7.6^{+0.2}_{-5.2}$	$6.44^{+0.17}_{-4.50}$	$5.08^{+0.09}_{-3.48}$
M_T^{min} [TeV]	1.5	1.6	1.7	1.8	1.9	2.0
Observed limit [fb]	1.10	1.09	0.89	0.78	0.58	0.58
Expected limit [fb]	$4.38^{+0.10}_{-2.88}$	$3.82^{+0.08}_{-2.48}$	$3.01^{+0.07}_{-1.97}$	$2.84^{+0.04}_{-1.80}$	$2.46^{+0.04}_{-1.62}$	$2.30^{+0.04}_{-1.48}$

Chapter 8

Summary and Outlook

A search for new physics in the tau+E_T^{miss} channel has been performed and no significant deviations from the SM have been observed. For this thesis the multijet background has been determined with a data-driven approach and the improvement of this approach has been evaluated in the context of the exclusion limits for the SSM for the first time. Furthermore, this analysis has compared different isolation working points and provides limits for the SSM with a coupling constant equal to the one in the SM ($g_{W'} = g_W$). A summary of all exclusion limits from CMS for a W' decaying to a tau lepton in the SSM is shown in Fig. 8.1. With an integrated luminosity of 35.9 fb^{-1} the mass of the W' can be excluded up to 4.1 TeV.

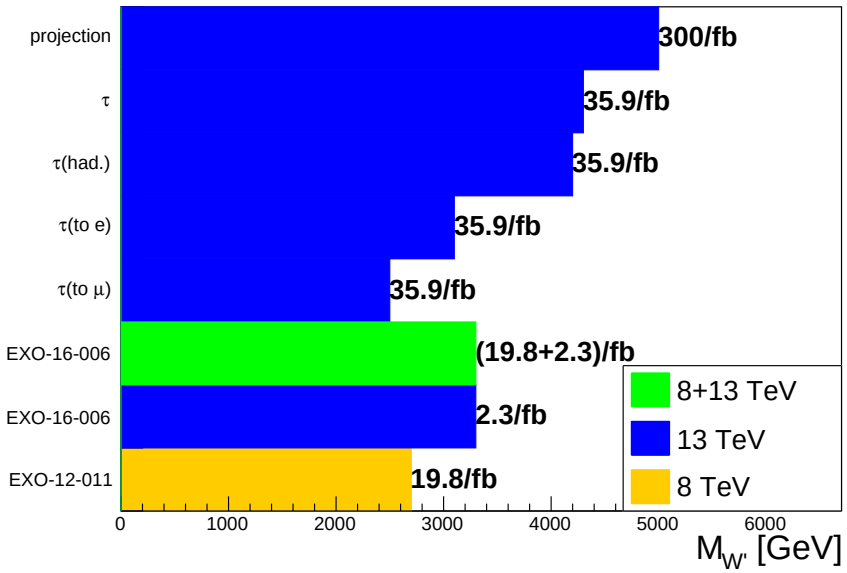

Figure 8.1: A summary of the exclusion limits. The observed limit from Ref. [46] is on the bottom most row, on the second and third rows from the bottom the observed limits from Ref. [20] are given. The observed limits and the projected expected limit determined in this thesis are given starting in the fourth row.

The impact of the coupling constant on the exclusion limit has been studied and the minimal excluded value for the fraction of coupling constants is found to be 0.2 at low masses and increases 1.5 at high masses. This limit subsequently has been reinterpreted in the context of the NUGIM yielding an upper mass limit of 2.3 TeV at $\cot\theta_E$=6.8.

In contrast to the model dependent limits, also a model independent limit has been derived. Effective cross sections ranging from 174 to 0.58 fb can be excluded.

As the projection of the SSM to $\mathcal{L}$=300 fb^{-1} shows, a gain in sensitivity of approximately 1 TeV can be expected for the SSM. If one further wants to increase the sensitivity of this model, new methods have to be introduced to this analysis. One option might be the use of machine learning in the context event classification into signal-like events and background-like events improving the signal to noise ratio and increasing the signal efficiency. This can be done either with a multivariate analysis using boosted decision trees or deep neural networks which, however, are more difficult to develop and understand.

Bibliography

[1] **CMS** Collaboration, "The CMS experiment at the CERN LHC", *JINST* **3** (2008) S08004.

[2] L. Evans and P. Bryant, "LHC Machine", *Journal of Instrumentation* **3** no. 08, (2008) S08001. http://stacks.iop.org/1748-0221/3/i=08/a=S08001.

[3] **ATLAS** Collaboration, "The ATLAS Experiment at the CERN Large Hadron Collider", *JINST* **3** (2008) S08003.

[4] **ALICE** Collaboration, "The ALICE experiment at the CERN LHC", *JINST* **3** (2008) S08002.

[5] **LHCb** Collaboration, "The LHCb Detector at the LHC", *JINST* **3** (2008) S08005.

[6] J. Haffner, "The CERN accelerator complex. Complexe des accélérateurs du CERN",. http://cds.cern.ch/record/1621894. General Photo.

[7] W. Herr and B. Muratori, "Concept of luminosity", *CAS - CERN Accelerator School: Intermediate Course on Accelerator Physics, Zeuthen, Germany, 15 - 26 Sep 2003, pp.361-378 (CERN-2006-002)* (2006) . https://cds.cern.ch/record/941318.

[8] Z. Xie, "CMS Luminosity - Public Results", Feb, 2017. https://twiki.cern.ch/twiki/bin/view/CMSPublic/LumiPublicResults#2016_Proton_Proton_13_TeV_Collis. [Online; accessed 11 March 2017].

[9] **CMS** Collaboration, V. Karimäki, M. Mannelli, P. Siegrist, H. Breuker, A. Caner, R. Castaldi, K. Freudenreich, G. Hall, R. Horisberger, M. Huhtinen, and A. Cattai, *The CMS tracker system project: Technical Design Report*. Technical Design Report CMS. CERN, Geneva, 1997. https://cds.cern.ch/record/368412.

[10] A. Dominguez *et al.*, "CMS Technical Design Report for the Pixel Detector Upgrade", Tech. Rep. CERN-LHCC-2012-016. CMS-TDR-11, Sep, 2012. https://cds.cern.ch/record/1481838. Additional contacts: Jeffrey Spalding, Fermilab, Jeffrey.Spalding@cern.ch Didier Contardo, Universite Claude Bernard-Lyon I, didier.claude.contardo@cern.ch.

[11] **CMS** Collaboration, S. Mersi, "Phase-2 Upgrade of the CMS Tracker", *Nucl. Part. Phys. Proc.* **273-275** (2016) 1034–1041.

[12] **CMS** Collaboration, S. Chatrchyan *et al.*, "Performance of the CMS Level-1 Trigger during Commissioning with Cosmic Ray Muons", *JINST* **5** (2010) T03002, arXiv:0911.5422 [physics.ins-det].

[13] **CMS** Collaboration, *The CMS electromagnetic calorimeter project: Technical Design Report*. Technical Design Report CMS. CERN, Geneva, 1997. https://cds.cern.ch/record/349375.

[14] **CMS** Collaboration, *The CMS hadron calorimeter project: Technical Design Report*. Technical Design Report CMS. CERN, Geneva, 1997. https://cds.cern.ch/record/357153.

[15] **CMS** Collaboration, *The CMS magnet project: Technical Design Report*. Technical Design Report CMS. CERN, Geneva, 1997. https://cds.cern.ch/record/331056.

[16] **CMS** Collaboration, *The CMS muon project: Technical Design Report*. Technical Design Report CMS. CERN, Geneva, 1997. https://cds.cern.ch/record/343814.

[17] **CMS** Collaboration, S. Chatrchyan *et al.*, "The performance of the CMS muon detector in proton-proton collisions at sqrt(s) = 7 TeV at the LHC", *JINST* **8** (2013) P11002, arXiv:1306.6905 [physics.ins-det].

[18] **CMS** Collaboration, G. L. Bayatyan *et al.*, *CMS TriDAS project: Technical Design Report, Volume 1: The Trigger Systems*. Technical Design Report CMS. https://cds.cern.ch/record/706847.

[19] **CMS** Collaboration, S. Cittolin, A. Rácz, P. Sphicas, *et al.*, *CMS The TriDAS Project: Technical Design Report, Volume 2: Data Acquisition and High-Level Trigger. CMS trigger and data-acquisition project*. Technical Design Report CMS. CERN, Geneva, 2002. https://cds.cern.ch/record/578006.

[20] **CMS** Collaboration, "Search for W' decaying to tau lepton and neutrino in proton-proton collisions at sqrt(s) = 13 TeV", CMS Physics Analysis Summary CMS-PAS-EXO-16-006, CERN, Geneva, 2016. http://cds.cern.ch/record/2140976.

[21] D. J. Griffiths, *Introduction to elementary particles; 2nd rev. version*. Physics textbook. Wiley, New York, NY, 2008. ISBN: 9783527406012.

[22] M. Peskin and D. Schroeder, *An Introduction to Quantum Field Theory*. Advanced book classics. Avalon Publishing, 1995. https://books.google.de/books?id=i35LALN0GosC.

[23] F. J. Dyson, "The Radiation Theories of Tomonaga, Schwinger, and Feynman", *Phys. Rev.* **75** (Feb, 1949) 486–502. https://link.aps.org/doi/10.1103/PhysRev.75.486.

[24] F. Englert and R. Brout, "Broken symmetry and the mass of gauge vector mesons", *Phys. Rev. Lett.* **13** (Aug, 1964) 321–323. http://link.aps.org/doi/10.1103/PhysRevLett.13.321.

[25] P. W. Higgs, "Broken symmetries and the masses of gauge bosons", *Phys. Rev. Lett.* **13** (Oct, 1964) 508–509. http://link.aps.org/doi/10.1103/PhysRevLett.13.508.

[26] G. S. Guralnik, C. R. Hagen, and T. W. B. Kibble, "Global conservation laws and massless particles", *Phys. Rev. Lett.* **13** (Nov, 1964) 585–587. http://link.aps.org/doi/10.1103/PhysRevLett.13.585.

[27] **ATLAS, CMS** Collaboration, G. Aad *et al.*, "Measurements of the Higgs boson production and decay rates and constraints on its couplings from a combined ATLAS and CMS analysis of the LHC pp collision data at $\sqrt{s} = 7$ and 8 TeV", *JHEP* **08** (2016) 045, arXiv:1606.02266 [hep-ex].

[28] **CMS** Collaboration, S. Chatrchyan *et al.*, "Observation of a new boson at a mass of 125 GeV with the CMS experiment at the LHC", *Phys. Lett.* **B716** (2012) 30–61, arXiv:1207.7235 [hep-ex].

[29] **ATLAS** Collaboration, G. Aad *et al.*, "Observation of a new particle in the search for the Standard Model Higgs boson with the ATLAS detector at the LHC", *Phys. Lett.* **B716** (2012) 1–29, arXiv:1207.7214 [hep-ex].

[30] Particle Data Group, "Review of Particle Physics", *Chin. Phys.* **C40** no. 10, (2016) 100001.

[31] M. Davier, A. Hocker, and Z. Zhang, "The Physics of hadronic tau decays", *Rev. Mod. Phys.* **78** (2006) 1043–1109, arXiv:hep-ph/0507078 [hep-ph].

[32] *LEP design report.* CERN, Geneva, 1984. https://cds.cern.ch/record/102083. Copies shelved as reports in LEP, PS and SPS libraries.

[33] Y. L. Dokshitzer, "Calculation of the Structure Functions for Deep Inelastic Scattering and e^+ e^- Annihilation by Perturbation Theory in Quantum Chromodynamics.", *Sov. Phys. JETP* **46** (1977) 641–653. [Zh. Eksp. Teor. Fiz.73,1216(1977)].

[34] V. N. Gribov and L. N. Lipatov, "Deep inelastic e p scattering in perturbation theory", *Sov. J. Nucl. Phys.* **15** (1972) 438–450. [Yad. Fiz.15,781(1972)].

[35] G. Altarelli and G. Parisi, "Asymptotic Freedom in Parton Language", *Nucl. Phys.* **B126** (1977) 298–318.

[36] F. D. Aaron *et al.*, "Combined measurement and QCD analysis of the inclusive $e^{\pm}p$ scattering cross sections at HERA", *Journal of High Energy Physics* **2010** no. 1, (Jan, 2010) 109. http://dx.doi.org/10.1007/JHEP01(2010)109.

[37] H. Abramowicz *et al.*, "Combination of measurements of inclusive deep inelastic $e^{\pm}p$ scattering cross sections and qcd analysis of hera data", *The European Physical Journal C* **75** no. 12, (Dec, 2015) 580. http://dx.doi.org/10.1140/epjc/s10052-015-3710-4.

[38] L. A. Harland-Lang, A. D. Martin, P. Motylinski, and R. S. Thorne, "Parton distributions in the LHC era: MMHT 2014 PDFs", *Eur. Phys. J.* **C75** no. 5, (2015) 204, arXiv:1412.3989 [hep-ph].

[39] **WMAP** Collaboration, "Nine-year Wilkinson Microwave Anisotropy Probe (WMAP) Observations: Final Maps and Results", arXiv:1212.5225 [astro-ph].

[40] **Planck** Collaboration, P. A. R. Ade *et al.*, "Planck 2015 results. XIII. Cosmological parameters", *Astron. Astrophys.* **594** (2016) A13, arXiv:1502.01589 [astro-ph.CO].

[41] G. Altarelli, B. Mele, and M. Ruiz-Altaba, "Searching for New Heavy Vector Bosons in $p\bar{p}$ Colliders", *Z. Phys.* **C45** (1989) 109. [Erratum: Z. Phys.C47,676(1990)].

[42] **D0** Collaboration, V. M. Abazov *et al.*, "Search for W' bosons decaying to an electron and a neutrino with the D0 detector", *Phys. Rev. Lett.* **100** (2008) 031804, arXiv:0710.2966 [hep-ex].

[43] **CDF** Collaboration, K. Maeshima, "Search for Z-prime and W-prime at CDF", in *The Albuquerque meeting. Proceedings, 8th Meeting, Division of Particles and Fields of the American Physical Society, Albuquerque, USA, August 2-6, 1994. Vol. 1,2*, pp. 1141–1145. 1994. http://lss.fnal.gov/cgi-bin/find_paper.pl?conf-94-227.

[44] **CMS** Collaboration, V. Khachatryan *et al.*, "Search for physics beyond the standard model in final states with a lepton and missing transverse energy in proton-proton collisions at sqrt(s) = 8 TeV", *Phys. Rev.* **D91** no. 9, (2015) 092005, arXiv:1408.2745 [hep-ex].

[45] **ATLAS** Collaboration, G. Aad *et al.*, "Search for new particles in events with one lepton and missing transverse momentum in pp collisions at $\sqrt{s} = 8$ TeV with the ATLAS detector", *JHEP* **09** (2014) 037, arXiv:1407.7494 [hep-ex].

[46] **CMS** Collaboration, V. Khachatryan *et al.*, "Search for W' decaying to tau lepton and neutrino in proton-proton collisions at $\sqrt{(}s) = 8$ TeV", *Phys. Lett.* **B755** (2016) 196–216, arXiv:1508.04308 [hep-ex].

[47] **ATLAS** Collaboration, M. Aaboud *et al.*, "Search for new resonances in events with one lepton and missing transverse momentum in pp collisions at $\sqrt{s} = 13$ TeV with the ATLAS detector", *Phys. Lett.* **B762** (2016) 334–352, arXiv:1606.03977 [hep-ex].

[48] M. Olschewski, *Search for new physics in proton-proton collision events with a lepton and missing transverse energy*. PhD thesis, RWTH Aachen University, Aachen, 2016. https://publications.rwth-aachen.de/record/572409. Veröffentlicht auf dem Publikationsserver der RWTH Aachen University; Dissertation, RWTH Aachen, 2016.

[49] Z. Sullivan, "Fully differential W' production and decay at next-to-leading order in QCD", *Phys. Rev.* **D66** (2002) 075011, arXiv:hep-ph/0207290 [hep-ph].

[50] E. Accomando, D. Becciolini, S. De Curtis, D. Dominici, L. Fedeli, and C. Shepherd-Themistocleous, "Interference effects in heavy W'-boson searches at the LHC", *Phys. Rev.* **D85** (2012) 115017, arXiv:1110.0713 [hep-ph].

[51] E. Boos, V. Bunichev, L. Dudko, and M. Perfilov, "Interference between W' and W in single-top quark production processes", *Phys. Lett.* **B655** (2007) 245–250, arXiv:hep-ph/0610080 [hep-ph].

[52] K. O. Padeken, *Search for new physics in the tau plus missing energy final states at CMS*. PhD thesis, RWTH Aachen University, Aachen, 2017. http://publications.rwth-aachen.de/record/689036. Veröffentlicht auf dem Publikationsserver der RWTH Aachen University; Dissertation, RWTH Aachen University, 2017.

[53] C.-W. Chiang, N. G. Deshpande, X.-G. He, and J. Jiang, "The Family $SU(2)_l \times SU(2)_h \times U(1)$ Model", *Phys. Rev.* **D81** (2010) 015006, arXiv:0911.1480 [hep-ph].

[54] L. Edelhäuser and A. Knochel, "Observing nonstandard W' and Z' through the third generation and Higgs lens", arXiv:1408.0914 [hep-ph].

[55] **CMS** Collaboration, "CMS Strategies for tau reconstruction and identification using particle-flow techniques", CMS Physics Analysis Summary CMS-PAS-PFT-08-001, CERN, Geneva. https://cds.cern.ch/record/1198228.

[56] **CMS** Collaboration, "Particle-Flow Event Reconstruction in CMS and Performance for Jets, Taus, and MET", CMS Physics Analysis Summary CMS-PAS-PFT-09-001, CERN, 2009. Geneva, Apr, 2009. https://cds.cern.ch/record/1194487.

[57] **CMS** Collaboration, F. Beaudette, "The CMS Particle Flow Algorithm", in *Proceedings, International Conference on Calorimetry for the High Energy Frontier (CHEF 2013): Paris, France, April 22-25, 2013*, pp. 295–304. 2013. arXiv:1401.8155 [hep-ex]. https://inspirehep.net/record/1279774/files/arXiv:1401.8155.pdf.

[58] W. Adam, R. Frühwirth, A. Strandlie, and T. Todor, "Reconstruction of Electrons with the Gaussian-Sum Filter in the CMS Tracker at the LHC", Tech. Rep. CMS-NOTE-2005-001, CERN, Geneva, Jan, 2005. https://cds.cern.ch/record/815410.

[59] **CMS** Collaboration, "Missing transverse energy performance of the CMS detector", *Journal of Instrumentation* **6** (Sept., 2011) 9001, arXiv:1106.5048 [physics.ins-det].

[60] **CMS** Collaboration, "Tau identification in CMS", CMS Physics Analysis Summary CMS-PAS-TAU-11-001, CERN, Geneva, 2011. https://cds.cern.ch/record/1337004.

[61] **CMS** Collaboration, "Performance of reconstruction and identification of tau leptons in their decays to hadrons and tau neutrino in LHC Run-2", CMS Physics Analysis Summary CMS-PAS-TAU-16-002, CERN, Geneva, 2016. https://cds.cern.ch/record/2196972.

[62] **CMS** Collaboration, A. M.Bachtis, S.Dasu, "Prospects for measurement of $\sigma(pp \to Z) \cdot \mathcal{B}(Z \to \tau^+\tau^-)$ with CMS in pp Collisions at $\sqrt{s} = 7$ TeV ", CMS-AN-2010/082, CERN, Geneva, 2010. https://cds.cern.ch/record/1337004.

[63] A. Nehrkorn, "Software guide for tau reconstruction", Mar, 2017. https://twiki.cern.ch/twiki/bin/view/CMSPublic/SWGuidePFTauID. [Online; accessed 23 April 2017].

[64] S. Baffioni, C. Charlot, F. Ferri, D. Futyan, P. Meridiani, I. Puljak, C. Rovelli, R. Salerno, and Y. Sirois, "Electron reconstruction in CMS", Tech. Rep. CMS-NOTE-2006-040, CERN, Geneva, Feb, 2006. http://cds.cern.ch/record/934070.

[65] R. Fruhwirth, "Application of Kalman filtering to track and vertex fitting", *Nucl. Instrum. Meth.* **A262** (1987) 444–450.

[66] **CMS** Collaboration, V. Khachatryan *et al.*, "Performance of Electron Reconstruction and Selection with the CMS Detector in Proton-Proton Collisions at $\sqrt{s} = 8$ TeV", *JINST* **10** no. 06, (2015) P06005, arXiv:1502.02701 [physics.ins-det].

[67] **CMS** Collaboration, "Electron and photon performance in CMS with the full 2016 data sample.",. https://cds.cern.ch/record/2255497.

[68] **CMS** Collaboration, S. Chatrchyan *et al.*, "Performance of CMS muon reconstruction in *pp* collision events at $\sqrt{s} = 7$ TeV", *JINST* **7** (2012) P10002, arXiv:1206.4071 [physics.ins-det].

[69] **CMS** Collaboration, "Muon Identification and Isolation efficiency on full 2016 dataset",. https://cds.cern.ch/record/2257968.

[70] **CMS** Collaboration, "Github repository for cmssw." https://github.com/cms-sw/cmssw. [Online; accessed 18 December 2015].

[71] Aachen 3a CMS working group, "Gitlab repository for tapas", Okt, 2015. https://gitlab.cern.ch/aachen-3a/tapas. [Online; accessed 11 March 2017].

[72] H. P. Bretz *et al.*, "A Development Environment for Visual Physics Analysis", *JINST* **7** (2012) T08005, arXiv:1205.4912 [physics.data-an].

[73] **CMS** Collaboration, "CMS Luminosity Measurements for the 2016 Data Taking Period", CMS Physics Analysis Summary CMS-PAS-LUM-17-001, CERN, Geneva, 2017. https://cds.cern.ch/record/2257069.

[74] **CMS** Collaboration, "Search for Wprime decaying to tau lepton and neutrino in proton-proton collisions at 13 TeV", CMS-AN-2016/356, CERN, Geneva, 2017. CMS internal Analysis Note.

[75] **CMS** Collaboration, "Cross section calculation for leptonicaly decaying W at NNLO QCD and NLO electroweak", Tech. Rep. CMS-AN-2014/263, CERN, Geneva, 2015. CMS internal Analysis Note.

[76] S. Agostinelli *et al.*, "Geant4—a simulation toolkit", *Nuclear Instruments and Methods in Physics Research Section A: Accelerators, Spectrometers, Detectors and Associated Equipment* **506** no. 3, (2003) 250 – 303. http://www.sciencedirect.com/science/article/pii/S0168900203013688.

[77] J. Allison *et al.*, "Geant4 developments and applications", *IEEE Trans. Nucl. Sci.* **53** (2006) 270.

[78] J. Allison *et al.*, "Recent developments in geant4", *Nuclear Instruments and Methods in Physics Research Section A: Accelerators, Spectrometers, Detectors and Associated Equipment* **835** (2016) 186 – 225. http://www.sciencedirect.com/science/article/pii/S0168900216306957.

[79] T. Sjostrand, S. Mrenna, and P. Z. Skands, "A Brief Introduction to PYTHIA 8.1", *Comput. Phys. Commun.* **178** (2008) 852–867, arXiv:0710.3820 [hep-ph].

[80] T. Sjöstrand, S. Ask, J. R. Christiansen, R. Corke, N. Desai, P. Ilten, S. Mrenna, S. Prestel, C. O. Rasmussen, and P. Z. Skands, "An Introduction to PYTHIA 8.2", *Comput. Phys. Commun.* **191** (2015) 159–177, arXiv:1410.3012 [hep-ph].

[81] N. Davidson, G. Nanava, T. Przedzinski, E. Richter-Was, and Z. Was, "Universal Interface of TAUOLA Technical and Physics Documentation", *Comput. Phys. Commun.* **183** (2012) 821–843, arXiv:1002.0543 [hep-ph].

[82] V. Ciulli, "Summary table of samples produced for the 1 Billion campaign, with 25ns bunch-crossing", Apr, 2017. https://twiki.cern.ch/twiki/bin/viewauth/CMS/SummaryTable1G25ns. [Online; accessed 15 August 2017].

[83] J. Alwall, R. Frederix, S. Frixione, V. Hirschi, F. Maltoni, O. Mattelaer, H. S. Shao, T. Stelzer, P. Torrielli, and M. Zaro, "The automated computation of tree-level and next-to-leading order differential cross sections, and their matching to parton shower simulations", *JHEP* **07** (2014) 079, arXiv:1405.0301 [hep-ph].

[84] J. Alwall, M. Herquet, F. Maltoni, O. Mattelaer, and T. Stelzer, "MadGraph 5 : Going Beyond", *JHEP* **06** (2011) 128, arXiv:1106.0522 [hep-ph].

[85] P. Nason, "A New method for combining NLO QCD with shower Monte Carlo algorithms", *JHEP* **11** (2004) 040, arXiv:hep-ph/0409146 [hep-ph].

[86] S. Frixione, P. Nason, and C. Oleari, "Matching NLO QCD computations with Parton Shower simulations: the POWHEG method", *JHEP* **11** (2007) 070, arXiv:0709.2092 [hep-ph].

[87] S. Alioli, P. Nason, C. Oleari, and E. Re, "A general framework for implementing NLO calculations in shower Monte Carlo programs: the POWHEG BOX", *JHEP* **06** (2010) 043, arXiv:1002.2581 [hep-ph].

[88] J. M. Campbell, R. K. Ellis, P. Nason, and E. Re, "Top-Pair Production and Decay at NLO Matched with Parton Showers", *JHEP* **04** (2015) 114, arXiv:1412.1828 [hep-ph].

[89] R. Frederix, E. Re, and P. Torrielli, "Single-top t-channel hadroproduction in the four-flavour scheme with POWHEG and aMC@NLO", *JHEP* **09** (2012) 130, arXiv:1207.5391 [hep-ph].

[90] G. Balossini, G. Montagna, C. M. Carloni Calame, M. Moretti, O. Nicrosini, F. Piccinini, M. Treccani, and A. Vicini, "Combination of electroweak and QCD corrections to single W production at the Fermilab Tevatron and the CERN LHC", *JHEP* **01** (2010) 013, arXiv:0907.0276 [hep-ph].

[91] J. R. Andersen *et al.*, "Les Houches 2013: Physics at TeV Colliders: Standard Model Working Group Report", arXiv:1405.1067 [hep-ph].

[92] R. Gavin, Y. Li, F. Petriello, and S. Quackenbush, "W Physics at the LHC with FEWZ 2.1", *Comput. Phys. Commun.* **184** (2013) 208–214, arXiv:1201.5896 [hep-ph].

[93] S. G. Bondarenko and A. A. Sapronov, "NLO EW and QCD proton-proton cross section calculations with mcsanc-v1.01", *Comput. Phys. Commun.* **184** (2013) 2343–2350, arXiv:1301.3687 [hep-ph].

[94] **CMS** Collaboration, "PDF Uncertainties and K-factor Calculations for the SSM W' at 13 TeV Collisions", Tech. Rep. CMS-AN-2014/240, CERN, Geneva, 2014. CMS internal Analysis Note.

[95] B. Fuks and J. Donini, "Feynrules W' Effective model." https://feynrules.irmp.ucl.ac.be/wiki/Wprime#no1. [Online; accessed 15 August 2017].

[96] **CMS** Collaboration, "Search for charged Higgs bosons with the $H^{\pm} \to \tau^{\pm}\nu_{\tau}$ decay channel in the fully hadronic final state at $\sqrt{s} = 13$ TeV", CMS Physics Analysis Summary CMS-PAS-HIG-16-031, CERN, Geneva, 2016. https://cds.cern.ch/record/2223865.

[97] **CMS** Collaboration, "Search for new physics in the tau + MET final states with the full 2012 dataset at sqrt(s)=8 TeV", CMS-AN-2013/043, CERN, Geneva, 2015. CMS internal Analysis Note.

[98] C. Palmer, "Recommended cross section for pile-up reweigthing." https://hypernews.cern.ch/HyperNews/CMS/get/luminosity/613/2/1/1/1.html. [Online; accessed 15 August 2017].

[99] J. Rojo, "PDF4LHC recommendations for Run II", *PoS* **DIS2016** (2016) 018, arXiv:1606.08243 [hep-ph].

[100] Y. Takahashi, "TauID for 13 TeV run: recommendation from the Tau POG." https://twiki.cern.ch/twiki/bin/viewauth/CMS/TauIDRecommendation13TeV. [Online; accessed 15 August 2017].

[101] A. O. M. Iorio, "Recommended Jet Energy Corrections and Uncertainties For Data and MC." https://twiki.cern.ch/twiki/bin/view/CMS/JECDataMC. [Online; accessed 15 August 2017].

[102] AndreyPopov, "Jet Energy Resolution." https://twiki.cern.ch/twiki/bin/view/CMS/JetResolution. [Online; accessed 15 August 2017].

[103] **CMS** Collaboration, "Search for new physics in l+MET channel with 2016 data", CMS-AN-2016/204, CERN, Geneva, 2017. CMS internal Analysis Note.

[104] **CMS** Collaboration, "Search for high-mass resonances in lepton plus MET final state with 2016 data", CMS Physics Analysis Summary CMS-PAS-2016/033, CERN, Geneva, 2017. in prep.

[105] R. E. Kass and L. Wasserman, "The selection of prior distributions by formal rules", *Journal of the American Statistical Association* **91** no. 435, (1996) 1343–1370. http://www.tandfonline.com/doi/abs/10.1080/01621459.1996.10477003.

[106] **CMS** Collaboration, "Github repository for cms higgs combination toolkit", Aug, 2013. https://github.com/cms-analysis/HiggsAnalysis-CombinedLimit. [Online; accessed 21 May 2017].

[107] **CMS** Collaboration, "Documentation of the roostats-based statistics tools for higgs pag", Nov, 2015. https://twiki.cern.ch/twiki/bin/viewauth/CMS/SWGuideHiggsAnalysisCombinedLimit. [Online; accessed 21 May 2017].

[108] L. Moneta, "Twiki for roostats", Mar, 2015. https://twiki.cern.ch/twiki/bin/view/RooStats/WebHome. [Online; accessed 21 May 2017].

Acknowledgments

I would like to thank everybody, who has helped, supported or contributed to this work:

Firstly, I am grateful to Prof. Dr. Hebbeker for providing the opportunity to write this thesis at the Physics Institute III A and to Dr. Kerstin Hoepfner for again supervising of my thesis in this institute. I am also grateful to PD Dr. Pooth for being the second examiner.

Even though, he did not supervise me directly during my Master's thesis, I would like to thank the mentor of Bachelor's thesis Klaas Padeken for his continuous help during my Bachelor's and Master's theses. Furthermore, I would like to thank Sebastian Wiedenbeck for being a better office college, than I could have hoped for, being a tremendous help with various problems and a readily available partner when discussing various topics.

I would like to thank all current and former members of the W' workgroup, I have had the pleasure of working with. I am thankful for their help, either with technical details or physical understanding. I hope that I was able to return the trust placed in me within the context of the analysis and was able to give back as much as I received from this workgroup. The W' workgroup has not only helped me gather experience but also mature in the scientific community.

While I would like express my appreciation of the harmonic and comfortable working atmosphere within the entire Aachen-3A-CMS group, I would like to highlight the readiness for discussion and help provided by Thomas Esch in the context of this analysis.

I would like to thank everybody who proofread my thesis, especially Dr. Kerstin Hoepfner for her invaluable advice and Sebastian Wiedenbeck for finding all sorts of mistakes. I am also grateful to those keeping me motivated and hope that I am able to return the favor.

Lastly, I would like to thank my parents for giving me to opportunity to study physics and for their continued support.